UNIVERSITY OF CALIFORNIA

Los Angeles

Fundamentals and Applications of the World's Hardest Metals

A dissertation submitted in partial satisfaction of the

requirements for the degree of Doctor of Philosophy

in Chemistry

by

Christopher Turner

2016

ABSTRACT OF THE DISSERTATION

Fundamentals and Applications of the World's Hardest Metals

by

Christopher Turner

Doctor of Philosophy in Chemistry

University of California, Los Angeles, 2016

Professor Richard B. Kaner, Chair

The application of an advanced material, in this case transition metal borides, requires a fundamental understanding of the materials' physical and chemical properties. In this thesis, the bonding environment of boron and various borides are investigated, the solubility limits and physical properties of transition metal substitutes to form solid solutions are explored, and new insights in the causes for "superhard" behavior in the boride families are elucidated. Broadening the understanding of boron's place in borides require a deep look into the environment boron encounters in each structure type. Pure boron exists in various allotropes, predominantly in amorphous (disordered) and crystalline (uniformly ordered), which provide similar x-ray diffraction spectra, but different solid state NMR spectra. The discrepancy arises from the unique bonding environment the boron atoms encounter.

After gaining insight into one of the simplest forms of boron, more complex species with unique structures are analyzed: aluminum diboride (not covered here in detail), rhenium diboride, and tungsten diboride (a hybrid of the two structure types). In the field of solid state NMR, the borides of greatest interest, historically, have been those of common structure type (i.e. AlB_2, alternating layers of planar

boron sheets and metal atoms) and in some cases unique, such as MgB_2 which is superconducting. Other morphologies, like ReB_2, a superhard metal ($H_v \geq 40$ GPa) had until recent been overlooked; containing similar structural motifs to AlB_2, such that they alternate puckered boron sheets and metal atoms, but exhibiting superhard ultra-incompressible characteristics. Traditional characterization of superhard materials involve X-ray diffraction (XRD), neutron diffraction, energy dispersive spectroscopy (EDS), and mechanical hardness testing (Vickers). The x-ray diffraction and neutron diffraction analyses provide structure information—atomic coordinates—within the unit cell. The coordination of the atoms within the structure can be deduced from the data provided by crystallographic (eg. XRD) means; this coordination may then be corroborated with NMR data. First principles calculations are growing in popularity, but simulating the more complex structure types is far from trivial, especially when randomly distributed partial occupancies and partial vacancies exist. Moving towards an application of these novel materials requires fine-tuning of the chemical and physical properties they express. These materials must be hard, tough, readily wettable, and resistant to oxidation. Therefore, the application of these compounds requires the *fundamental* understanding of *how* the properties come to be. Hybrid materials, in the form of solid solutions, allow us to evoke the desired traits. Solid solutions are materials containing a partial substitution of a parent element by another element within the structure; molybdenum partially substituted for tungsten in the tungsten tetraboride structure (WB_4) would become $W_{1-x}Mo_xB_4$ where x is the percent substituted. Adding molybdenum (or any transition metal) has its limits, but as seen in a subsequent chapters, the change in hardness and oxidation resistance is in some cases significant. The emphasis on producing next generation materials for any application lies within knowing the capabilities and limitations of the material.

The dissertation of Christopher Turner is approved.

Sarah Tolbert

Jenn-Ming Yang

Richard B. Kaner, Committee Chair

University of California, Los Angeles

2016

DEDICATION

To the pursuit of knowledge,
entertaining curiosity,
answering the question 'why?',
and to Thunder

TABLE OF CONTENTS

List of Tables

List of Figures

ACKNOWLEDGEMENTS

The particular sequence of occurrences leading to the writing of this very thesis have been nothing less than serendipitous. I feel it would be difficult to clearly any given moment to produce the trajectory I have followed thus far; to pick a point on the Fibonacci spiral and say “this is where it turns” is meaningless, because from a broader perspective, the spiral is infinitely the same. Some sort of chain reaction of pursuits—both physical and mental, intellectual growth, building friendships, and realizing the vastness of that which remain unknown have culminated to this point, not as an end, but as a momentary pause in time, “now”. A starting point for my future in science may have been in my childhood, when I learned the power of the question “*why?*”. As it would be impossible to truly thank everyone involved *thus* far in my academic and industrial “career”, the immediate scope will be relevant to the last few years. Perhaps a chronological order would better suite our needs. This may be an unapologetically, exhaustive section so skip ahead for the SCIENCE.

I feel my interest in chemistry, in particular, was established in high school; Mr. Carl Vandercook was one of the first exposures to chemistry, and therefore, chemists. Chemists or those directly related to the field seem to have a kindred, analytical perception of “things” (that is some subdivision of the cosmos). At some point, I was his teaching assistant; it was a great pride to prepare the reagents necessary, but little did I know this was only the beginning. High school was also a time for friendships, a few friends in particular—Mr. Justin Day and Mr. Nick Kariger, I am grateful, as we had countless discussions on nearly everything. I didn’t have a particular college in mind, and in fact I missed the application deadlines for freshman enrollment due to both oversight, and the desire to work (probably too many hours). Community college was more or less a continuation of high school, but with the caveat of *choosing* the classes of interest. My community college professors at Antelope Valley College, Dr. Jessica Harper and Dr. David Newman, were by far the strongest gravitational forces to keeping the spiral

towards chemistry; additionally, I'd like to thank Mr. Scott Covell for the (dis)courses on English and a necessary appreciation for Pink Floyd.

While moonlighting as an aspiring academic, I worked when I should have, and was not, studying. My initial interest in chemistry was for a future in pharmaceuticals, inspired by Dr. Richard Wood, a pharmacist and former employer. Subsequent employment by Mr. Harley Frank, I am grateful for the opportunity and employment, and machine shop supervision by Mr. Jim Niggles who allowed me to enough become an aspiring machinist. The interest in machining would prove fortuitous on multiple occasions. First, I met Mr. Charlie Johnson, a master machinist, and his family—from the simple and complex parts we have machined, to the small "business" ventures, and to the homegrown fruits and vegetables, I am eternally thankful. The growing fascination with machining was paralleled with a developing interest in most things mechanical—namely cars. To Mr. Josh Boam, many thanks to you for the deep conversations, and late-night wrenching.

While in community college, the goal was to transfer to a "four-year"; while working the goal was to learn anything and everything hands-on. It was precisely at about this time, with a developing interest in cars, machining, and science that led me to befriend Mr. David Brickner, his (now) fiancé Ms. Tyana Hawker, and Mr. Brian Smith; I am extraordinarily grateful for the continued friendship, "reality-checks", and adventures. Incredible friends (all mentioned above and below) are necessary to ride the highs and lows of things beyond academics or work, that is to say, life. I worked full time, schooled full time, and playing my cards right, without intention, I transferred to one of the most respected universities in the world.

At the time of transferring, I felt I had lost direction in my future in chemistry, torn between the various divisions within. The concept of the pharmaceutical industry became rather disenchanting, but Inorganic chemistry, taught by my future mentor—Dr. Ric Kaner, brought me to a field of chemistry I hadn't yet discovered. For posterity: I was a student in his Solid-State Chemistry class, and given my

history of machining/metalworking, asked if he happened to know anything of tungsten carbide. Tungsten carbide is more or less the (currently) leading hard material used in industry (as noted in chapters within this thesis). It turns out, unbeknownst to me, that he was a leading expert on hard materials—namely borides. He asked why I was curious in particular, or if I had read any papers (journal articles) he had published. I mentioned a background in machining, and knew of tungsten carbide, but was curious as to the existence of others. Apparently, undergraduate research positions are both competitive and highly sought after; instead of asking for a research position, he offered one! He (and my future colleagues) were working on the worlds hardest metals. I found my way into a lab, his lab, and made many friends/colleagues.

In no particular order, Drs. Veronica Strong, Yue (Jessica) Wang, Lisa Wang, Kan Wang, Sergey Dubin, Maher El'Kady, John Wassei, Danny King, Wanmei Sun, Miao Xie, Brian McVerry, and Jaime Torres made lab an intellectually stimulating place and provided great discussion. Drs. Julio D'Arcy and Tom Farrell assisted me in the understanding of lab culture and all that would become grad school. Dr. Michael Yeung and Mr. Georgiy Akopov proved invaluable for their discussions on borides and most any topic. Mr. Matt Kowal has been an integral part of sanity maintenance, that is, to go outside and do things, from wrenching to climbing, always a fresh idea. Ms. Samantha Clarke, as an undergrad classmate, friend, and grad student peer—many great times were had. Ms. Avalon Dismukes, my first undergrad researcher, I owe many thanks; countless hours spent preparing, polishing, and analyzing samples as well as discussions on direction and theory for the applications of hard materials. Friends and colleagues are hand in hand, in grad school, and as such Mr. Kris Marsh, Dr. John Cook, and Boris Volosskiy have been there nearly every step of the way. I feel eternally grateful to Dr. Reza Mohammadi, one of the kindest humans I have ever met: inspiration, motivation, consolation, and friendship. Dr. Andrew Lech—my (undergrad) mentor and friend—an enigma and wealth of knowledge, many thanks are in order for the guidance and insightful conversations. I have also had the great pleasure of collaborating with Dr. Robert Taylor and Dr. Dimitrios

Koumoulis on the solid state NMR work. I feel very fortunate to have been able to work with Dr. Taylor, an expert in the field; I sincerely thank you. Between him and Dimitrios, we have corroborated atomic behavior to structural positions for a variety of borides, previously unexplored.

I have been very fortunate to establish collaborations with researchers at the Jet Propulsion Lab, under the supervision of Dr. Jean Pierre Fleurial, through the JPL Visiting Scholar Research Program. Dr. Sabah Bux has been a phenomenal mentor and collaborator, thank you for entertaining my wild ideas and for the intellectual and sometimes abstract conversations. Dr. James Ma, for the crash course in spark plasma sintering and investigative methodology, and of course, ideas. Mr. Dean Cheikh, for the countless topics covered, the carpooling, and keeping WSW alive. The rest of the 277 crew, including but not limited to: Mr. Billy Li, Dr. Kathy Lee, Dr. Fivos Drymiotis, and all others in bldg. eleven.

More recently, with the search for direct applications, I am grateful to Mr. Hans Schieder, Mr. Nick Higdon and Mr. Leo Porter-Zasada for the endless milling, analysis and polishing—I wish you both the best in your future academic careers. To Ms. Lisa Pangilinan, may the borides treat you well; there remains many compositional variations unexplored. Ms. Lindsay Chaney has been an incredible help in the day-to-day grind towards producing viable samples, and therefore, metrics. Dr. Keshavan and Dr. Kavanaugh for the insightful discussions regarding the potential futures of the world's hardest metal.

Dr. Sarah Tolbert and Dr. Xianfeng Duan were instrumental as advisors and mentors, for the helpful discussions and keeping my path moving forward. An additional thank you to Dr. Jenn-Ming Yang for serving (Profs. Duan and Tolbert) on my committee, and for use of the nano-indentation equipment.

Prof. Ric Kaner has been everything a graduate student/employee could ask for in a mentor/boss. Through the invitation to his join lab from *that* serendipitous conversation about hard materials, and the pursuit of funding through the commercialization grants and the encouragement to *do* what was necessary to make functional composites of the world's hardest metal. Although acceptance and approval of this dissertation will mean I am no longer in lab, I believe you will always be an exceptional mentor.

Family, blood and otherwise, are an integral part towards achieving higher goals. To my mother Terri, I am endearingly grateful for the support you have provided me. To my father Robert and step-mother Ann, thank you for the encouragement, motivation, and assistance with any obstacles I have encountered. To my brothers, Brian, Scott, and Kevin, and step-brothers, Brent and Eric, I am indebted to you all for everything, said and experienced. Grandparents, Don and Pearl, and Joann and Richard, thank you for the words of wisdom and encouragement in my endeavors, both academic and otherwise. To aunts, uncles, cousins and extended family, thank you for everything. To the Harris family, thank you for sharing the varieties of life. Denise and Alex Harris I am grateful for their motivation and fruitful discussions, on the path to complete such a daunting task. I feel particularly indebted to Dave Harris, who taught me innumerable things, especially “getting things done, right the first time”; I feel everything he taught me, is relevant to, and will last, a lifetime—I think he would be proud. Taylor Harris, my dearest and beloved, thank you for everything, every step of the way, all the time—without you, *this* journey would have seemed evermore insurmountable.

I am grateful to have had the necessary funding to carry out my research, both fundamental and applied. I would like to thank the National Science Foundation, Department of Materials Research, for the funding our lab has utilized to produce exceptional results on fundamental studies on borides. I would also like to thank the UCLA Dean of Sciences Commercialization grant funders and the University of California Proof of Concept program for pushing forward the applied materials program as well as additional support provided in collaboration with SuperMetalix, Inc.

Chapters 2 and 3 are largely adapted from the work: Turner, C. L., Taylor, R.E., & Kaner, R.B. "10B and 11B NMR Study of Elemental Boron." *The Journal of Physical Chemistry C* (2015), and Koumoulis, D., Turner, C.L., Taylor, R.E. &Kaner, R.B. “11B NMR spectral and Nuclear Spin-Lattice Relaxation Analyses of ReB2.” *The Journal of Physical Chemistry C*. (2016).

Chapter 4 is an adaptation of a paper *submitted for publication*, Turner, C.L., Zukovic, Z., Koumoulis, D., Taylor, R.E., Kaner, R.B. 11B NMR Study of WB2. (2016).

Chapter 5 is an adaptation of the work found in Lech, A. T.*, Turner, C. L.*, Lei, J., Mohammadi, R., Tolbert, S. H., & Kaner, R. B. Superhard Rhenium/Tungsten Diboride Solid Solutions. *Journal of the American Chemical Society* (2016).

Chapters 6, 7, and 8 cover the essentials of the resolution of the WB_4 structure and compositional/structural differences in its solid solutions; historically, our lab has focused on the synthesis, characterization, and further understanding of this complex boride. It has been an ongoing project for me for the past six years, in addition to other boride species and their subsequent applications, and our lab's involvement with borides extends back even further. The following, respectively, are the works on such: Lech, A.T., Turner, C. L., Mohammadi, R., Tolbert, S. H. & Kaner, R. B. "The Structure of Super-hard Tungsten Tetraboride: A 'Missing Link' between MB_2 and MB_{12} – type Higher Borides." *Proc. of the Nat. Aca. of Sciences 112 (11) (2015),* 3223-3228, Mohammadi, R., Turner, C.L., Xie M., Yeung, M.T., Lech, A.T., Tolbert, S.H. & Kaner, R.B. "Enhancing the Hardness of Superhard Transition Metal Borides: Molybdenum-Doped Tungsten Tetraboride." *Chemistry of Materials 28*(2) (2015), 632-637, and Akopov, G., Yeung, M.T., Turner, C.L., Mohammadi, R. and Kaner, R.B., "Extrinsic Hardening of Superhard Tungsten Tetraboride Alloys with Group 4 Transition Metals." *Journal of the American Chemical Society 138*(17) (2016): 5714-5721.

VITA

Education

B.S. Chemistry	The University of California, Los Angeles 2012
M.S. Chemistry	The University of California, Los Angeles 2013
Ph. D Candidate	The University of California, Los Angeles 2014 –

Research

Post-Baccalaureate

Research Fellow, UCLA, Kaner Group

Focus 1: Investigation of metal-matrix composites—Synthesis and Application
Focus 2: Solid state chemistry research investigating Superhard, Refractory Transition-Metal Borides
Focus 3: Solid State NMR on Borides

Undergraduate Research

Summer 2010 - Summer 2012

University of California, Los Angeles, Student Research Program (SRP)—Initial investigations in ceramic-metallic composites and solid solution

Technical Skills

- High temp. / High pressure synthesis
- Metathesis Reactions
- Powder Metallurgy
- Scanning Electron Microscopy (SEM)
- Energy-dispersive spectrometry (EDS)
- X-Ray powder diffraction (XRD)
- 3D Modelling / Drafting / Design
- Finite Element Analysis (FEA)
- Micro- and Nano-Indentation
- Solid-State Nuclear Magnetic Resonance (NMR)
- Static/Dynamic Light Scattering (SLS / DLS)
- Optical Microscopy
- Atomic Force Microscopy (AFM)
- Thermogravimetric Analysis (TGA)
- Inert Atmosphere Materials handling
- Grant / Funding / Patent Application authoring
- Design and fabrication of high vacuum systems and laboratory equipment

Awards

Fall 2011	Glenn T. Seaborg Symposium Poster Session, 1st Place Undergraduate Div.
Fall 2012	Dean of Sciences Commercialization Grant
Spring 2013	University of California Proof of Concept Startup Grant

Publications and Presentations

Turner, C.L., Zukovic, Z., Koumoulis, D., Taylor, R.E., Kaner, R.B. 11B NMR Study of WB2. *Submitted*

Lech, A. T.*, Turner, C. L.*, Lei, J., Mohammadi, R., Tolbert, S. H., & Kaner, R. B. Superhard Rhenium/Tungsten Diboride Solid Solutions. *Journal of the American Chemical Society* (2016).

Akopov, G., Yeung, M. T., Sobell, Z. C., Turner, C. L., Lin, C. W., & Kaner, R. B. Superhard Mixed Transition Metal Dodecaborides. *Chemistry of Materials*, *28*(18) (2016), 6605-6612.

Yeung, M.T., Lei, J., Mohammadi, R., Turner, C.L., Wang, Y., Tolbert, S.H. and Kaner, R.B. "Superhard Monoborides: Hardness Enhancement through Alloying in $W_{1-x}Ta_xB$." *Advanced Materials* (2016).

Akopov, G., Yeung, M. T., Turner, C. L., Li, R. L., & Kaner, R. B. (2016). "Stabilization of HfB12 in Y1–x Hf x B12 under Ambient Pressure." *Inorganic chemistry*, *55*(10) (2016), 5051-5055.

Akopov, G., Yeung, M.T., Turner, C.L., Mohammadi, R. and Kaner, R.B., "Extrinsic Hardening of Superhard Tungsten Tetraboride Alloys with Group 4 Transition Metals." *Journal of the American Chemical Society 138*(17) (2016): 5714-5721.

Koumoulis, D., Turner, C.L., Taylor, R.E. &Kaner, R.B. "11B NMR spectral and Nuclear Spin-Lattice Relaxation Analyses of ReB2." *The Journal of Physical Chemistry C*. (2016) 10.1021/acs.jpcc.5b10410

Detsi, E., Cook, J.B., Lesel, B.K., Turner, C.L., Liang, Y.L., Robbennolt, S. & Tolbert, S.H. "Mesoporous Ni 60 Fe 30 Mn 10-alloy based metal/metal oxide composite thick films as highly active and robust oxygen evolution catalysts." *Energy & Environ. Sci*. (2015), 10.1039/C5EE02509E

Mohammadi, R., Turner, C.L., Xie M., Yeung, M.T., Lech, A.T., Tolbert, S.H. & Kaner, R.B. "Enhancing the Hardness of Superhard Transition Metal Borides: Molybdenum-Doped Tungsten Tetraboride." *Chemistry of Materials 28*(2) (2015), 632-637

Xie, M., Mohammadi, R., Turner, C. L., Kaner, R. B., Kavner, A., & Tolbert, S. H. "Exploring hardness enhancement in superhard tungsten tetraboride-based solid solutions using radial X-ray diffraction." *Appl. Phy. Letters*,*107*(4) (2015), 041903.

Turner, C. L., Taylor, R.E., & Kaner, R.B. "10B and 11B NMR Study of Elemental Boron." *The Journal of Physical Chemistry C* (2015).

Lech, A.T., Turner, C. L., Mohammadi, R., Tolbert, S. H. & Kaner, R. B. "The Structure of Super-hard Tungsten Tetraboride: A 'Missing Link' between MB_2 and MB_{12} – type Higher Borides." *Proc. of the Nat. Aca. of Sciences 112 (11) (2015),* 3223-3228

D'Arcy, Julio M., et al. "Vapor-Phase Polymerization of Nanofibrillar Poly (3, 4-ethylenedioxythiophene) for Supercapacitors." *ACS nano* 8.2 (2014): 1500-1510.

Xie, M., Mohammadi, R., Turner, C. L., Kaner, R. B., Kavner, A., & Tolbert, S. H. "Lattice stress states of superhard tungsten tetraboride from radial x-ray diffraction under nonhydrostatic compression." *Physical Review B*90.10 (2014): 104104.

R. Mohammadi, M. Xie, A. T. Lech, C. L. Turner, A. Kavner, S. H. Tolbert & R. B. Kaner, "Toward Inexpensive Superhard Materials: Tungsten Tetraboride-Based Solid Solutions", Journal of the American Chemical Society (JACS), 134 (2012) 20660-20668.

Conference Papers and Abstracts

R.B. Kaner*, R. Mohammadi, A. T. Lech, M. Xie, C. L. Turner and S. H. Tolbert, "Synthesis and Characterization of Low-Cost Superhard Transition Metal Borides", invited talk at APS-SCCM & AIRAPT-24 Joint Conference, Seattle, WA, USA, July 7-12, 2013.

C.L. Turner*, A. T. Lech, R. Mohammadi, M. Xie, S. H. Tolbert, R.B. Kaner. "Superhard Metallic Borides", invited talk at Gordon Research Conference on Solid State Chemistry, New London, NH, USA, July 22-27, 2012.

C. L. Turner*, R. Mohammadi, A. T. Lech, M. Xie, S. H. Tolbert and R. B. Kaner, "Superhard Solid Solutions Based on Tungsten Tetraboride", poster presentation at the American Chemical Society (ACS) Spring Meeting, San Diego, CA, USA, March 25-29, 2012.

Chapter 1

Introduction

The interest in borides, namely transition metal borides, has been nearly as multi-faceted as the crystal structures they assume. Borides have risen in popularity in recent years for their interesting properties: high melting point (refractory), oxidation resistance, hardness, toughness, and even superconductivity.[1-4] These properties follow compositional trends—the transition metal dictating crystal structure and therefore the exhibited behavior. The rudimentary characterization of most borides was first conducted in the U.S.S.R. and Europe in the 1950's via the "brute-force" method.[5] A plethora of variations in metal to boron concentration were documented through X-ray diffraction (XRD) and added to the list of known phases. On occasion, these phases were further analyzed: oxidation temperature, hardness, or melting point – were worth noting. Ultimately, these materials were being groomed for potential applications—refractory coatings[6], metalworking tools[7], or bearing materials[8]. As an example, lanthanum hexaboride had been found to have a low work function making it ideal for use as an electron beam source in scanning electron microscopes.[9]

The initial and underlying goal was to find an application for a hard material, and produce a superhard transition metal boride capable of competing with the most advanced industry standards. The purpose of this thesis is not to educate one on the history of metal tools or their applications, but to inform on the state-of-the-art materials that may replace the existing standards. Our search for materials that have potential for the next generation of cutting tools or abrasives have led us to a new class of superhard metals, the transition metal borides. Since metals may be

readily cut into shapes using electric discharge machining (EDM),[10] a technique available to all modern machine shops, metals have great potential as superhard materials if they can be synthesized in a cost effective manner. Unfortunately, our early superhard refractory borides contained platinum group transition metals (Os, Ru, and Re) making them exorbitantly expensive. Ruthenium diboride (RuB_2), osmium diboride (OsB_2) and rhenium diboride (ReB_2) formed the first generation of borides to be considered for machining purposes.[11-13] For example, ReB_2 has a Vickers hardness above 40 GPa, can scratch diamond, can be synthesized at ambient pressure, is electrically conductive, and has excellent elastic properties. Hence, these superhard materials are promising in all aspects except one – cost. Thus, the superhard borides would be prohibitively expensive for wide-scale use; however, the solution was clear: replace the expensive platinum group metals with an alternative, readily available transition metals, while increasing the boron concentration to create more hard covalent bonds.

This exploration resulted in tungsten tetraboride (WB_4) and its alloys. This relatively inexpensive, superhard boride exhibits a hardness of up to ~57 GPa with a facile synthesis using arc melting under ambient pressure.[14] Solid solutions of WB_4 under investigation in our laboratory have further increased hardness, toughness, oxidation resistance, etc.[15-16] Tungsten tetraboride could well become the material for the next generation of cutting tools. My objective in this thesis is to investigate the feasibility of incorporating WB_4 as an inexpensive superhard material into industrial applications through systematic synthesis and fabrication techniques. The initial goal of the project was to produce a cutting tool insert prototype using WB_4, as seen in Figure 1.1. Creating a prototype WB_4 tool insert required incorporation of the processes found in WC tool production. These methods are well established and many methods are shared between the syntheses of WC and WB_4. Currently, WB_4 ingots are synthesized in a resistive-arc melting furnace in an argon

atmosphere under ambient pressure. The samples may then be crushed through ball milling and mechanical grinding to an appropriate particle size; the composition, purity, particle size and particle shape of each powder batch is critical.

Similar to tungsten carbide, WB_4 without a binder is too brittle to be used directly as a cutting tool; thus, we have explored the use of transition metals (and combinations thereof) as binders to introduce enhanced fracture toughness in the final product. Sintering processes such as high-temperature furnace sintering, hot pressing (HP), hot isostatic pressing (HIP), or spark plasma sintering (SPS), have been successfully used to produce composites. The addition of binders to a finely divided hard material is commonly used to increase wear resistance, thus further increasing the life of the implement. The sacrifice of *some* hardness for fracture toughness is necessary, but the total loss in hardness is negligible, since the initial hardness of WB_4 far surpasses WC and approaches that of c-BN. Production of industry targeted composites and abrasives through rigorous vetting processes is an unsung success of this project. Thorough understanding of an *applied* material is necessary to effectively *use* said material.

Subsequently, in addition to the potential applications, I simultaneously engaged in the applied and more academic study of borides with colleagues in the Kaner lab, in collaboration with the Tolbert and Kavner labs, at UCLA. This work primarily focused on the tungsten boride family and third row transition metal borides. The boride research was predominantly fundamental in nature, exploratory for the definitive crystal structure, bonding behavior, or even solubility of another transition metal substituted for the parent metal (ternary "solutions"). Collaboration with Drs. Mohammadi, Lech, Xie, and Yeung, and Mr. Akopov, has resulted in many of compositions having produced phenomenal properties, some of which form the basis for chapters herein.[15-18]

The immediate behavior of boron in different crystal structures, and therefore bonding environments, became a collaborative interest with Dr. Bob Taylor, also seen in subsequent chapters.[19-20]

Initially, the behavior of boron in solid-state nuclear magnetic resonance (SSNMR) in the tungsten tetraboride structure was what sparked the collaboration. Incidentally the boron signal was highly convoluted as the structure poses *at least* four unique boron types (unique due to their bonding environment). Realizing the potential bonding complexity for the metal-boride structures, an initial study on the differences found between amorphous and crystalline boron was conducted. The primary synthesis method used by our lab is electric arc melting, which requires a slight excess in boron composition due to the volatility of boron at ~3000°C. Some samples requiring the slight excess may in turn contain crystalline boron that precipitates at the grain boundaries. This secondary crystalline boron phase would then produce a unique signal of its own. Proper identification would ease deconvolution of the signal when more complex structures were analyzed.

Historically, there has been a limited interest in the field of SSNMR on boron (and borides), but perhaps this will change. The information available relates mostly to magnesium diboride (MgB_2)[21], a known superconducting diboride. Two other crystal structures of particular interest for SSNMR are: AlB_2, and ReB_2.[22] Aluminum diboride alternates between flat sheets and metal atoms; however, rhenium diboride has alternating layers of puckered sheets and metal atoms. Figure 1.2 demonstrates the differences between the structure types. Understanding boron and the two aforementioned structures led to WB_2, which has a hybrid structure between AlB_2 and ReB_2, also shown in Figure 1.2.

The pursuit of application-viable composites and abrasives is never ending; however, the materials quickly approach an industry-ready state. Academically, borides are gaining international attention as their unique chemical and physical properties, as well as potential for industrial applications, become recognized.

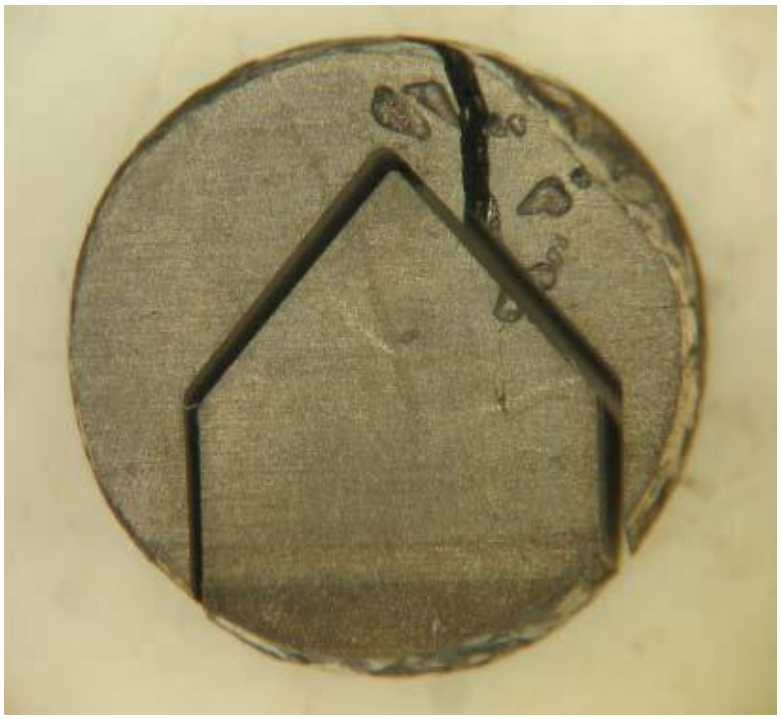

Figure 1.1. A proof of concept insert; tungsten tetraboride cut into a suitable lathe insert shape via wire-EDM.

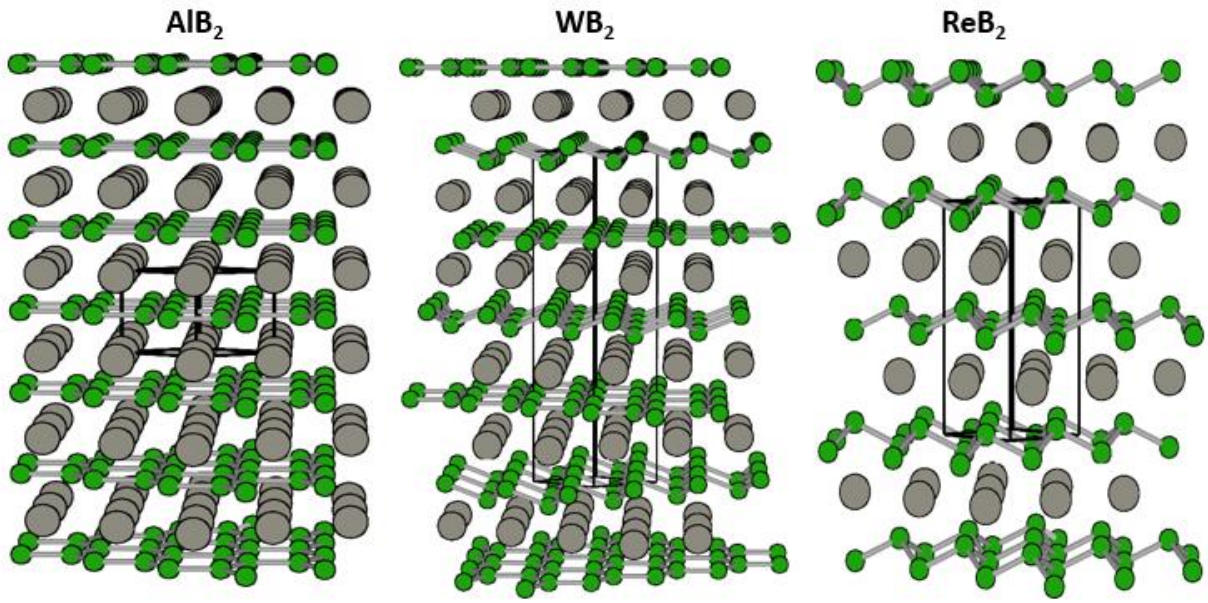

Figure 1.2. Metal Diboride structures: aluminum diboride (most common), tungsten diboride, and rhenium diboride, respectively.

References

(1) Lundström, T. Borides: Solid-State Chemistry. *Encyclopedia of Inorganic Chemistry* **2006**, 481−494.

(2) Levine, J. B.; Nguyen, S. L.; Rasool, H. I.; Wright, J. A.; Brown, S. E.; Kaner, R. B. Preparation and Properties of Metallic, Superhard Rhenium Diboride Crystals. *J. Am. Chem. Soc.* **2008**, 130 (50), 16953− 16958

(3) Akopov, G.; Yeung, M.T.; Sobell, Z.C.; Turner, C.L.; Kaner, R.B.; Lin, C.-W. Superhard Mixed Metal Dodecaborides. *Chem. Mater.* **2016**, 28, 6605−6612.

(4) Matthias, A. B. T.; Geballe, T. H.; Andres, K.; Corenzwit, E.; Hull, G. W.; Maita, J. P. Superconductivity and Antiferromagnetism in Boron-Rich Lattices. *Science* **1968**, *159*, 530.

(5) Samsonov, G. V.; Markovskii, L. Y.; Zhigach, A. F.; Valyashko, M. G. Boron, Its Compounds and Alloys [in Russian]; House of the Academy of the Sciences Ukrainian SSR: Kiev, **1960**.

(6) Chandran, K. R.; Sanders, A. P.; Du, J.; Walker, L. S.. Rapid Synthesis of Nanostructured Titanium Boride (TiB) by Electric Field Activated Reaction Sintering. *Processing, Properties, and Design of Advanced Ceramics and Composites: Ceramic Transactions* **2016**, *259*, 187.

(7) Woods H.P.; Wawner F.E.; Fox B.G. Tungsten diboride: preparation and structure. *Science* **1966**, *151*(3706):75.

(8) Mayer, W. J.; Lange, W. H.; & Turner, J. T. **1965** *U.S. Patent No. 3,212,834*. Washington, DC: U.S. Patent and Trademark Office.

(9) Timofeeva, I. I.; Timofeeva, E. N. Physicochemical Properties of Lanthanide Hexaborides. *Inorg. Mater.* **1968**, *4*, 1559−1561.

(10) Ho, K.H.; Newman, S.T.; Rahimifard, S.; Allen, R.D. State of the Art in Wire Electrical Discharge Machining (WEDM), *Int. J. Mach. Tool Manu.***2004,** *44*, 1247 (2004).

(11) Cumberland, R. W.; Weinberger, M. B.; Gilman, J. J.; Clark, S. M.; Tolbert, S. H.; Kaner, R. B. Osmium diboride, an ultra-incompressible, hard material. *J. Am. Chem. Soc.* **2005**, *127*(20), 7264-7265.

(12) Weinberger, M.B.; Levine, J.B.; Chung, H.Y.; Cumberland, R.W.; Rasool, H.I.; Yang, J.M.; Kaner, R.B.; Tolbert, S.H. Incompressibility and Hardness of Solid Solution

Transition Metal Diborides: Os1− x Ru x B2. *Chemistry of Materials* **2009**, *21*, 9: 1915-1921.

(13) Chung, H.-Y.; Weinberger, M.B.; Levine, J.B.; Cumberland, R.W.; Kavner, A.; Yang, J.-M.; Tolbert, S.H.; Kaner, R.B. Synthesis of ultra-incompressible superhard rhenium diboride at ambient pressure, *Science* **2007,** *316*, 436.

(14) Mohammadi, R.; Lech, A. T.; Xie, M.; Weaver, B. E.; Yeung, M. T.; Tolbert, S. H.; Kaner, R. B. Tungsten Tetraboride, an Inexpensive Superhard Material. *P. Natl. Acad. Sci.* **2011**, *108*, 10958-10962.

(15) Mohammadi, R.; Xie, M.; Lech, A. T.; Turner, C. L.; Kavner, A.; Tolbert, S. H.; Kaner, R. B. Toward Inexpensive Superhard Materials: Tungsten Tetraboride-Based Solid Solutions. *J. Am. Chem. Soc.* **2012**, *134* (51), 20660−20668.

(16) Akopov, G.; Yeung, M. T.; Turner, C. L.; Mohammadi, R.; Kaner, R. B. Extrinsic Hardening of Superhard Tungsten Tetraboride Alloys with Group 4 Transition Metals. *J. Am. Chem. Soc.* **2016**, *138* (17), 5714−5721.

(17) Yeung, M. T.; Lei, J.; Mohammadi, R.; Turner, C. L.; Wang, Y.; Tolbert, S. H.; Kaner, R. B. Superhard Monoborides: Hardness Enhancement through Alloying in W1−xTaxB. Adv. Mater. **2016**, *28*, 6993−6998.

(18) Lech, A.T., Turner, C.L., Lei, J., Mohammadi, R., Tolbert, S.H. and Kaner, R.B. Superhard Rhenium/Tungsten Diboride Solid Solutions. *J. Am. Chem. Soc.* **2016**, *138*(43),14398-14408.

(19) Turner, C. L., Taylor, R.E., & Kaner, R.B. 10B and 11B NMR Study of Elemental Boron. *The J. of Phys. Chem. C* **2015**, *19*(24), 13807-13813.

(20) Koumoulis, D., Turner, C.L., Taylor, R.E. &Kaner, R.B. "11B NMR spectral and Nuclear Spin-Lattice Relaxation Analyses of ReB2." *The J. of Phys. Chem. C* **2016** *120*(5), 2901-2907.

(21) J. Nagamatsu, J.; Nakagawa, N.; Muranaka, T.; Zenitani, Y.; Akimitsu, J. Superconductivity at 39 K in magnesium diboride, *Nature* **2001**, *410* (6824), 63-64.

(22) Silver, A. H.; Kushida, T. Nuclear Magnetic Resonance in Transition-Metal Diborides, *J. Chem. Phys.* **1963**, *38*, 865 -872.

Chapter 2

Introduction

Transition metal borides exhibit an interesting range of physical properties, including being superhard materials[1]. These superhard materials are characterized by high valence-electron density and bond covalency and may exist as insulators or semiconductors. In the synthesis of boron-based superhard materials, such as WB_4 [2], elemental boron is, in some instances, a side product that is difficult to separate from the desired superhard material. For characterization of such boron-based superhard materials by nuclear magnetic resonance (NMR) spectroscopy, it is desirable to have a good characterization of elemental boron in order to investigate the NMR responses arising from the transition metal borides. Discerning the spectroscopic behavior of boron alone will aid in the thorough comprehension of its behavior within the metal-boride structure.

The interaction between boron and metal atoms within the structure contains multitudes of bonding environments. Elucidation of the boron-metal interaction will further allow the "prediction" of plausible metal-boride structures. Historically, the borides have been characterized through X-ray diffraction (XRD), energy dispersive X-ray spectroscopy (EDS), and a host of physical measurements such as micro- and nano-indentation and thermo-gravimetric analysis. Clearly defining boron's interactions allows corroboration with previously used techniques to further realize metal-boride structures. Comprehensive recognition of boron's bonding characteristics allows more precise tailoring of metal-boride structures. Bulk crystallographic properties are both theoretically predicted and experimentally determined, but boron's bonding environments currently leave room for further understanding.

Elemental boron also displays interesting properties of its own. In thermodynamically stable β-rhombohedral boron, the intrinsic defects arising from numerous partially occupied sites give rise to both semiconductive behavior[3] and "frustration" arising from antiferromagnetic correlations[4,5].

In the present study, both metallic and amorphous boron are characterized by ^{10}B and ^{11}B nuclear magnetic resonance (NMR) spectroscopy as a prelude to the study of boron-based superhard materials. Both resonant lineshape and spin-lattice relaxation data are presented and are compared and contrasted with previous literature results.

Materials and Methods

Samples prepared for NMR spectroscopy were used as received -- amorphous boron (99+%, Strem Chemicals) and crystalline boron (99%, Materion). Both samples contain the naturally occurring abundance ratio of ^{10}B to ^{11}B. Using a 325 mesh (44 μm) screen (Humboldt Mfg.), the boron powders were independently screened to ensure a uniform, maximum particle size for the NMR experiments. For characterization by X-ray, the samples were deposited onto silicon (511) "zero-background" plates, with excess material removed by razor blade to guarantee flatness. Diffraction patterns were collected from 10° to 76° 2$\boldsymbol{\theta}$ using an X'Pert Pro Bragg-Bentano geometry laboratory X-ray diffractometer (PANalytical) with nickel-filtered $Cu_{K\alpha}$ radiation (($\lambda_{K\alpha1}$ = 1.540593 Å, $\lambda_{K\alpha2}$ = 1.5444274 Å), flat sample state, 0.04 Soller slits, and X'Celerator position sensitive detector.

The NMR data were acquired with a Bruker DSX-300 spectrometer operating at frequencies of 96.29 MHz for ^{11}B and 32.24 MHz for ^{10}B. The NMR properties of the two boron isotopes are given in Table 2.1.

Magic-angle spinning (MAS) spectra were acquired with a standard Bruker MAS probe using a 4-mm outside diameter zirconia rotor with a sample spinning rate of 12 kHz. The ^{11}B $\pi/2$ pulse widths for the MAS experiments were 3 μs as measured on an aqueous solution of boric acid. The ^{11}B background from the boron nitride stator in the MAS probe was minimized by the use of the *E*limination of *A*rtifacts in NMR *S*pectroscop*Y* (*EASY*) pulse sequence[6].

Static polycrystalline samples of either metallic or amorphous boron were placed in a standard Bruker X-nucleus wideline probe with a 5-mm solenoid coil. The ^{11}B background from sodium borosilcate glass was avoided by the use of a polyimide coil support and a quartz sample tube. As a result, the ^{11}B spectral data could be directly acquired without the use of background suppression techniques such as *EASY*. Each sample was ground to 325 mesh to avoid radiofrequency (RF) skin-depth effects at this NMR frequency. Samples were confined to the length of the RF coil. The ^{11}B $\pi/2$ pulse width was 5 μs as measured with an aqueous boric acid standard. However, the "solid-state" ninety degree pulse width was reduced by a factor of $(I + ½)$, where I is the nuclear spin, in comparison with the ninety-degree pulse width for the same nucleus measured in solution[7,8].

Data for determining the spin-lattice relaxation times (T_1) were acquired with both saturation-recovery and inversion-recovery techniques[9].

The ^{11}B and ^{10}B chemical shift scales were calibrated using the unified Ξ scale[10], relating the nuclear shift to the ^{1}H resonance of dilute tetramethylsilane in $CDCl_3$ at a frequency of 300.13 MHz. The reference compound for defining zero ppm on each chemical shift scale is BF_3 etherate[10]. The chemical shift referencing was experimentally verified with the ^{11}B and ^{10}B resonances of an aqueous solution of boric acid[11] at pH = 4.4.

Spectral simulations were performed with the solids simulation package (‘‘solaguide’’) in the TopSpin (Version 3.1) NMR software program from Bruker BioSpin. The electron paramagnetic resonance (EPR) spectrum was acquired with a Bruker EMX spectrometer operating at 9.77 GHz.

Results and Discussion

The idealized crystal structure of β-rhombohedral elemental boron, $((B_{12})_4(B_{28})_2B$ or $B_{84}(B_{10})_2B$, is based on icosahedral subunits[4,5,12-14]. The x-ray diffraction spectra collected (independently) validated the elemental purity of each boron sample (Fig. 2.1). The crystalline boron spectrum contains the sharp, distinct peaks expected for a crystalline compound. The broader, less defined peaks obtained from the amorphous boron illustrate the less ordered structure expected for the amorphous material. The consistencies between peak locations, as shown in Fig. 2.1, provide agreement on the elemental purity (and identity) of each sample analyzed. There were no detectable impurities present in either sample.

The ^{11}B spectrum of a static sample of 325-mesh metallic β-rhombohedral elemental boron is shown in Fig. 2.2B. This spectrum is quite similar to those of previous NMR studies[12,15,16]. Different explanations of the spectral feature of “two split lines”[15] observed with natural abundance ^{11}B in the static sample have been offered in the literature. First is the suggestion that this feature arises from the “second order quadrupole effect”[15]. The parameters extracted from simulations of the second-order quadrupolar interaction for the central transitions of both the MAS and static-sample spectra are given in Table 2.2. Two issues are immediately apparent. The extracted parameters, *i.e.*, the shifts and quadruopolar coupling constants, from the simulations of a single second-order quadrupolar interaction in the two spectra of the same compound are not in

reasonable agreement. Also, while the simulation does describe the general features of the static lineshape, the simulation is not a particularly good fit. These issues suggest that the observed lineshape does not arise from the second-order quadrupolar interaction.

An alternative suggestion raises the possibility of "two distinct boron sites"[16]. The MAS spectrum, showing a single resonance in Fig. 2.2A, suggests that this two-site hypothesis is not correct. However, Lee and co-workers[16] did note that these two apparent peaks shifted as a function of particle size. In Fig. 6 of Reference 6.16, the two resonances observed for the "coarse….boron powder" appear at 114.4 and -150.2 ppm while they appear at 66.8 and -109.3 ppm for the "fine…boron powder". With the 325-mesh sample used for this study, the resonances appeared at 45.5 and -56.9 ppm. It is worth noting that the spectra acquired by Lee and co-workers[16] and the spectra reported here were obtained using the same magnetic field strength of 7.05 T.

The dependence of the "two peaks" upon particle size (and presumably shape) suggests that bulk magnetic susceptibility[17] contributes to the observed lineshape. Spectral broadening from isotropic bulk magnetic susceptibility will not be observed in the MAS experiment[18] (although anisotropic bulk susceptibility may still contribute to the broadening). The removal of spectral broadening from bulk magnetic susceptibility of the static sample under MAS (with averaging of the second-order quadrupolar interaction) explains the observation of a single peak in the MAS spectrum.

The intrinsic defects in β-rhombohedral boron arise from partial occupancy of unit cell sites[3-5]. The resulting paramagnetic centers are observed in the EPR spectrum shown in Fig. 2.3. Effects upon the NMR spectral features arising from paramagnetic centers are to be expected. The

spectral features of the ^{11}B spectrum of a static sample shown in Fig. 2.2B result from the combination bulk magnetic susceptibility with the lineshapes arising from the second-order quadrupolar interactions of varying magnitude. The evidence of varying quadrupolar coupling constants arises from the skewed resonance shown in the multiple quantum MAS (MQMAS)[19,20] spectrum in Fig. 2.4.

The ^{10}B spectrum of a static sample of 325-mesh metallic β-rhombohedral elemental boron is shown in Fig. 2.5. The major features observed in the spectrum can be achieved with a simple model. A simulation of first-order quadrupolar interactions from only three major sites, all with a chemical shift of -26 ppm but with differing quadrupolar coupling constants, reproduces the major spectral features. While using an asymmetry parameter, η, of zero for all three sites, the quadrupolar coupling constants, ν_Q, used in the simulation are zero Hz, 750 kHz, and 1,450 kHz.

The earlier single crystal and powder NMR study[12] of β-rhombohedral elemental boron reported evidence for sites with ν_Q of zero, 130 ± 30 kHz, and 680 ± 70 kHz. The ^{11}B MQMAS and ^{10}B NMR spectra are consistent with quadrupolar coupling constants over these ranges. However, the ^{10}B NMR spectrum indicates that there is an even larger quadrupolar coupling constant with a range centered around 1,450 kKz. All of these quadrupolar coupling constants are still smaller than those obtained from the single second-order quadrupolar simulations of the ^{11}B spectra and given in Table 2.2. This provides further evidence that the spectrum of the static sample does not arise solely from the second order quadrupolar interaction.

NMR relaxation studies provide information regarding both the structure and dynamics of chemical compounds. Usually the spin-lattice relaxation time constant is measured as the function

of some parameter, *e.g.*, temperature, pressure, or magnetic field strength. For this study of elemental boron, ^{11}B spin-lattice relaxation rates have been acquired as a function of temperature.

The results of a ^{11}B saturation-recovery experiment with a static sample of polycrystalline metallic boron at 296 K are shown in Figure 2.6. The plot shows the integrated area of the resonance of the central transition as a function of the time after application of a single ninety-degree saturation pulse.

The spin-lattice relaxation of a half-integer quadrupolar nucleus in a non-cubic singe crystal is typically characterized by a multi-exponential function regardless of whether the relaxation mechanism is quadrupolar or magnetic in origin[21]. Of course this assumes that the crystal is oriented in the static magnetic field such that there are no accidental degeneracies of the satellite energy levels with that of the central transition. The multi-exponential recovery results as the quadrupolar interaction creates unequal energy spacings in the Zeeman interaction. However, for spin-lattice relaxation of the same half-integer quadrupolar nucleus in polycrystalline samples, an exponential recovery is typically observed[22]. The suggestion[23] has been made that the mathematical process of orientational averaging[24] of quadrupolar relaxation gives rise to a spin-lattice relaxation well characterized by a single exponential function.

On the other hand, there are other mechanisms which produce non-exponential spin-lattice relaxation for these half-integer quadrupolar nuclei in solids, such as relaxation through spin diffusion from dilute paramagnetic centers[25]. The EPR spectrum in Fig. 2.3 suggests that the paramagnetic centers may play a role in the spin-lattice relaxation. The ^{11}B saturation-recovery data from a static sample of polycrystalline metallic boron at 296 K shown in Fig. 2.6, which is non-exponential, has been fit with three single-exponential functions. The time constants

extracted from fitting three single-exponential functions to the ^{11}B saturation-recovery data obtained as a function of temperature is shown in Fig. 2.7. The shortest time constants, T_1, are on the order of microseconds. There is scatter in these extracted time constants, but no discernable trend with temperature was noticed. However, the mid-range and longest time constants remain relatively constant at 248 K and below. Relaxation independent of temperature is a hallmark of relaxation by paramagnetic centers[26] for a sample in the rigid-lattice limit. Above 248 K, both the mid-range and longest time constants indicate a thermally activated relaxation mechanism. For numerical comparison with the shortest time constant noted above, the mid-range T_1 is 97 ms and the longest is 526 ms, both at 296 K. As analyses of both the mid-range and longest time constants yield the same activation energy of 15.8 kJ/mol (0.16 eV), there is a single relaxation mechanism responsible. This activation energy is in reasonable agreement with the 0.19 eV determined by photoconductivity measurements[3] for "localized states" in the band gap attributed to boron vacancies (*e.g.*, see Fig. 12 in Ref. 3). In short, the relaxation mechanism above 248 K is dominated by interaction with the conduction charge carriers originating from the boron vacancies.

The earlier single crystal and powder NMR study[12] of β-rhombohedral elemental boron reported a single spin-lattice relaxation measurement at ambient temperature and suggested that the relaxation mechanism was quadrupolar in origin. A "back of the envelope" calculation was used to rule out spin diffusion as a relaxation mechanism at ambient temperature. However, the variable temperature spin-lattice relaxation results reported here clearly show that the relaxation below 248 K is dominated by spin-diffusion from paramagnetic centers (as indicated by the independence of the spin-lattice relaxation rate with temperature) while relaxation above 248 is

dominated by a thermally-activated interaction with the conduction charge carriers. The shortest T_1 arises from boron nuclei in the immediate vicinity of the paramagnetic centers.

There is also interest in the properties of amorphous elemental boron[27-29] and comparison of its properties to those of metallic elemental boron. The ^{11}B spectrum of a static sample of 325-mesh amorphous elemental boron is virtually identical to that of the metallic β-rhombohedral elemental boron shown in Fig. 2.2B. However, the ^{11}B spin-lattice relaxation is slightly different. There are three time constants quite similar to the three found for the metallic β-rhombohedral elemental boron, but there is an additional component with a very long time constant of 44 s at ambient temperature. This very long time constant suggests the presence of isolated domains without boron vacancies, *i.e.*, an insulating material.

Conclusions

Both amorphous and β-rhombohedral elemental boron were investigated with ^{10}B and ^{11}B NMR. The ^{11}B spectrum of a static sample reflects both bulk magnetic susceptibility and second-order quadrupolar lineshapes of quadrupolar coupling constants ranging from zero to 1.45 MHz. In contrast to the previous literature, the variable temperature spin-lattice relaxation data indicate the ^{11}B relaxation at 248 K and below is dominated by spin-diffusion from paramagnetic centers. Above 240 K, relaxation is dominated by a thermally-activated interaction with the conduction charge carriers originating from the boron vacancies. Relaxation in amorphous elemental boron shows an additional insulating component with a comparatively long time constant of 44s.

Table 2.1. NMR Properties of Boron Nuclei[a]

Isotope	Spin	Natural Abundance (%)	Magnetogyric Ratio (10^7 rad s^{-1} T^{-1})	Quadrupolar Moment (fm^2)
^{11}B	3/2	80.1	8.5847044	4.059
^{10}B	3	19.9	2.8746786	8.459

[a]From Ref. 2.10

Table 2.2. ^{11}B NMR Parameters from Spectral Simulations of metallic Boron[a]

Compound	δ_{iso}[b] (ppm)	C_Q[c] (MHz)	υ_Q[d] (MHz)	η[e] (ppm)	Linebroadening (Hz)
Metallic Boron (static)	33.4	3.864	1.932	0	8100
Metallic Boron (MAS)	14.2	2.339	1.170	0	2498

[a]Spectral parameters obtained from simulations in Figure 2.2.

[b]Chemical shifts referenced to the unified Ξ scale .

[c]Quadrupolar coupling constant { $e^2qQ/\hbar$}.

[d]Quadrupolar frequency $\{(3e^2qQ)/[2I(2I-1)\hbar]\}$.

[e]η = asymmetry $\{\{0 \leq \eta \leq 1\}$

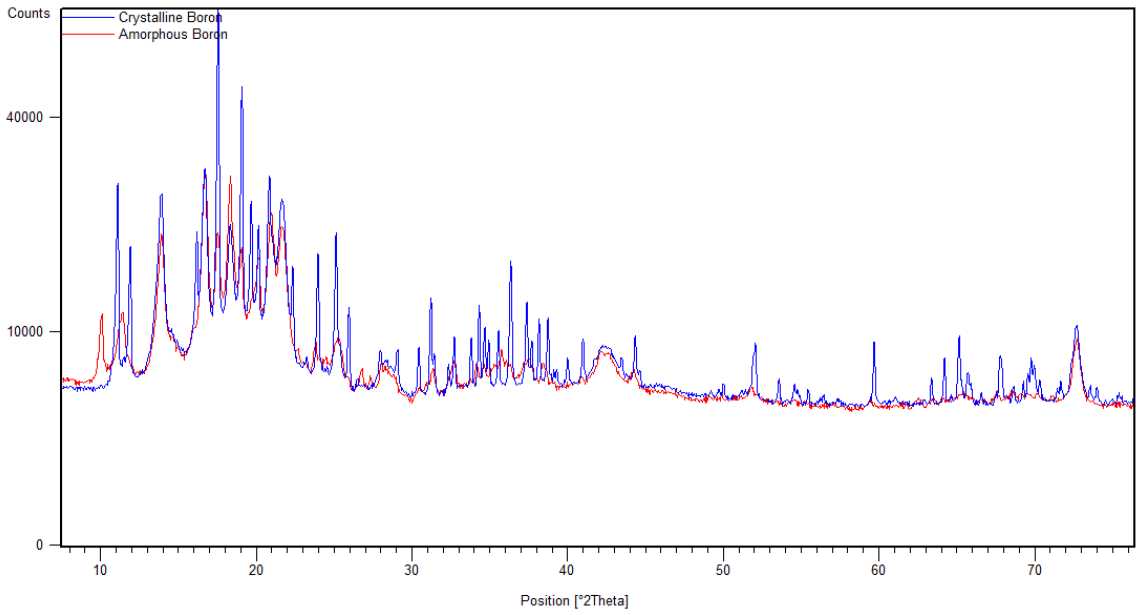

Figure 2.1: X-ray diffraction spectra of crystalline (blue) and amorphous (red) boron. The presence of fine peaks (blue line) indicates high crystallinity and structure. Conversely, the amorphous boron (red line) shows less apparent ordering (color online).

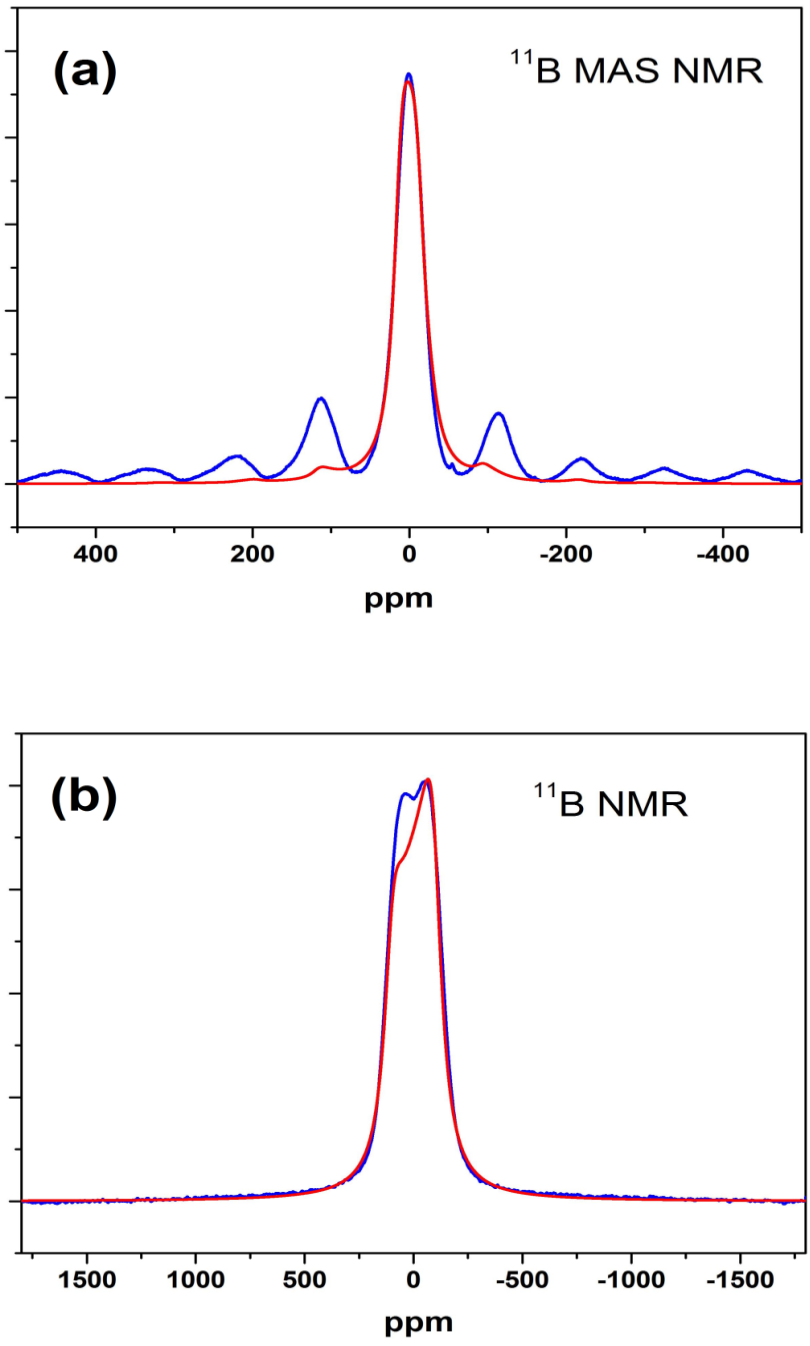

Figure 2.2: ^{11}B MAS spectrum (top) of polycrystalline metallic boron at 296 K with the ^{11}B wideline spectrum (bottom) of static polycrystalline metallic boron at 296 K. The simulated lineshapes are the smooth lines in red (color online). The difference in axes should be noted. Parameters extracted from the simulations are given in Table II.

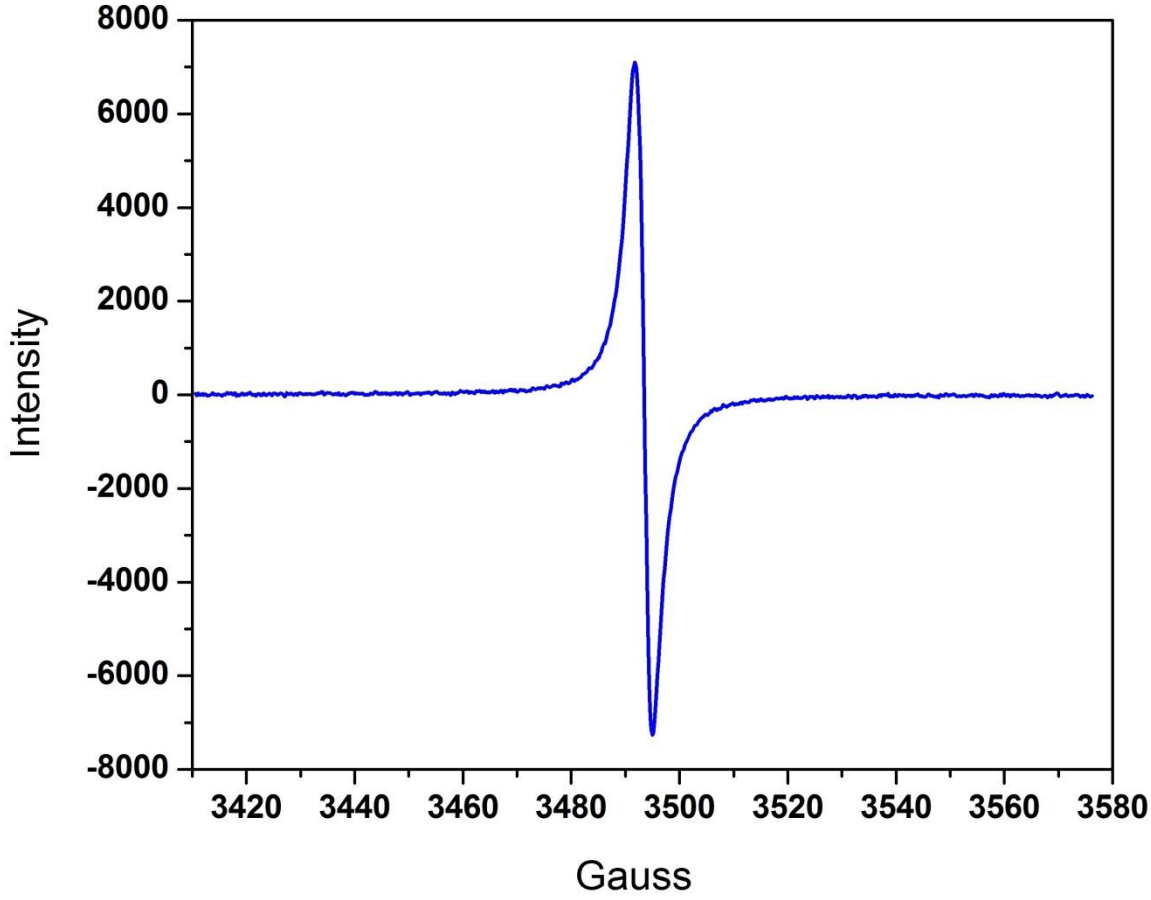

Figure 2.3: EPR spectrum of polycrystalline metallic boron at 296 K.

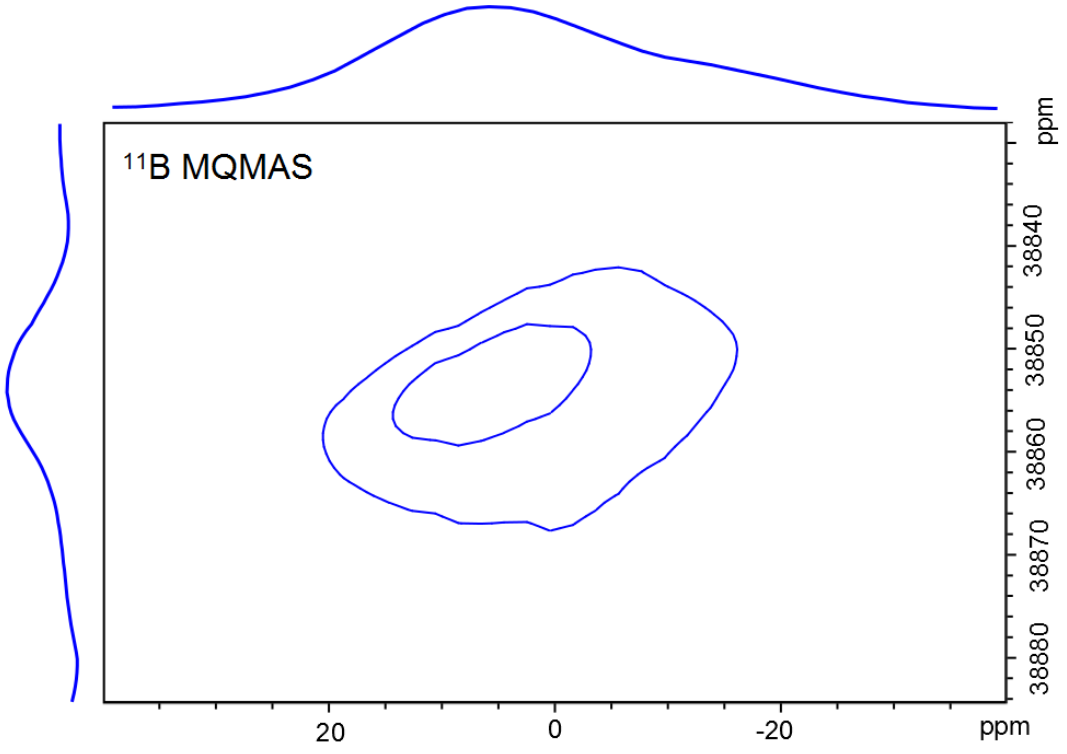

Figure 2.4: ^{11}B MQMAS spectrum of polycrystalline metallic boron at 296 K.

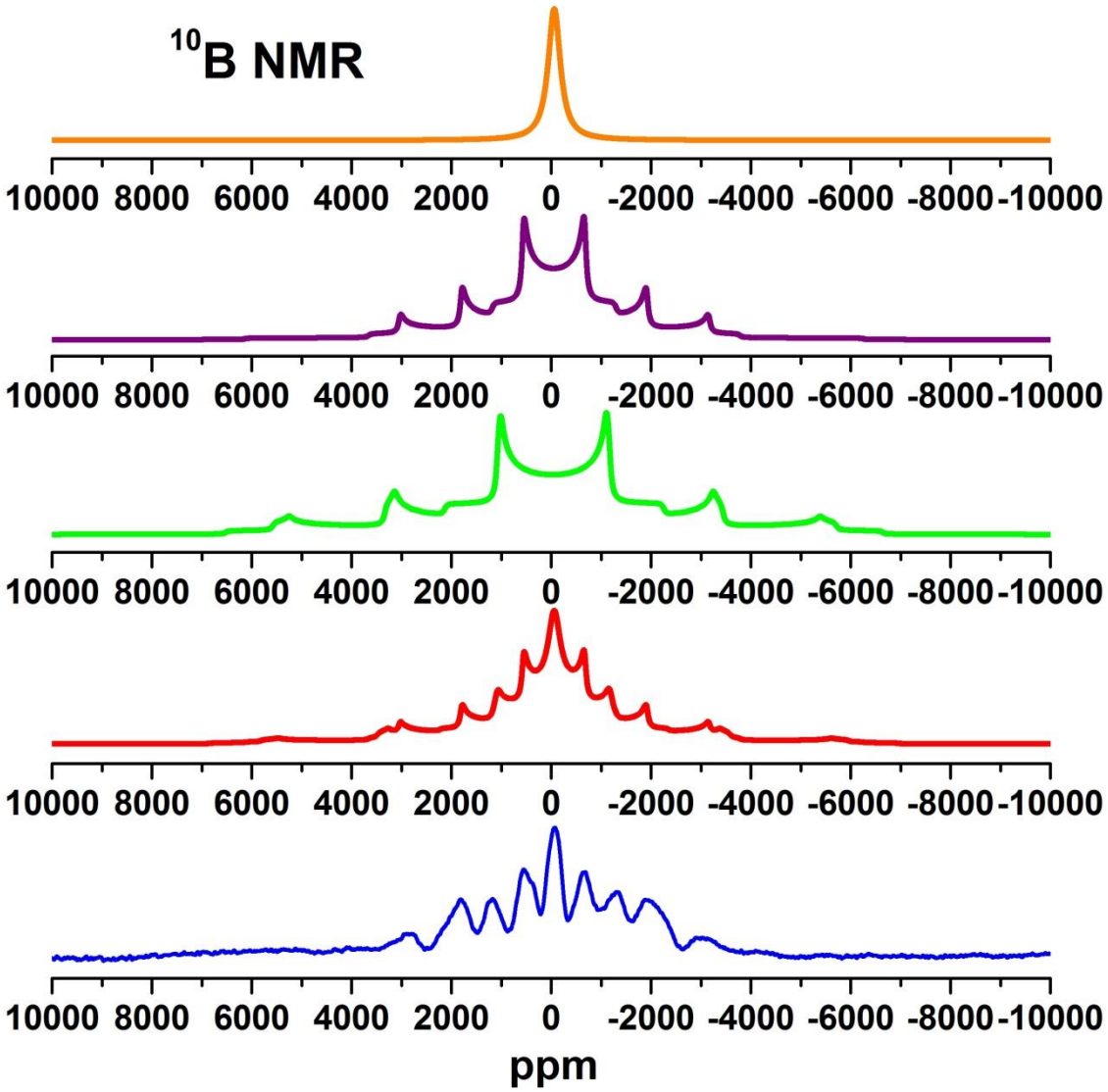

Figure 2.5: ^{10}B wideline spectrum (in blue) of static polycrystalline metallic boron at 296 K. The simulated spectrum (in red) is the summation of the simulations of three sites, presented above and described in the text.

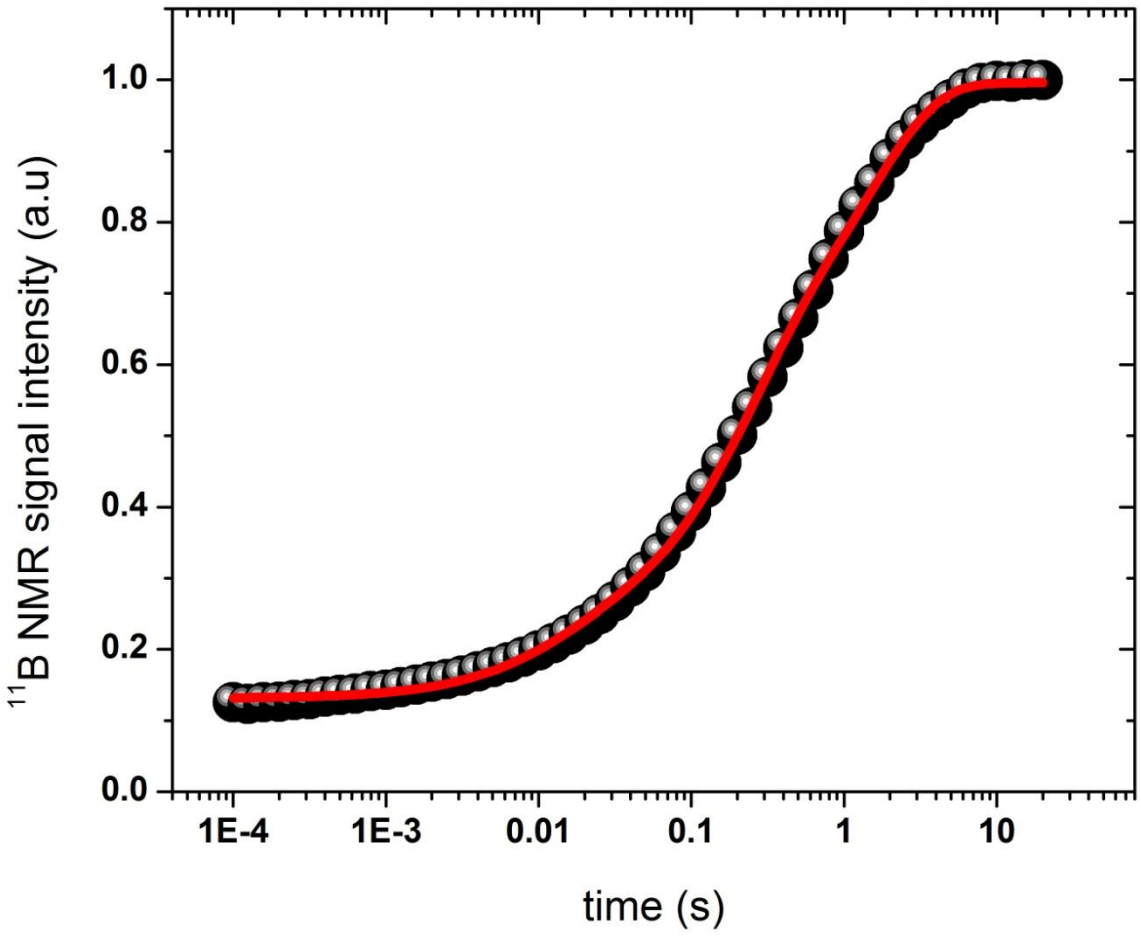

Figure 2.6: ^{11}B NMR saturation-recovery data for static polycrystalline metallic boron at 296 K with the variable time delay on a logarithmic scale so that the data points are evenly spaced. The smooth line (in red online) is the fit of three exponential functions to the data.

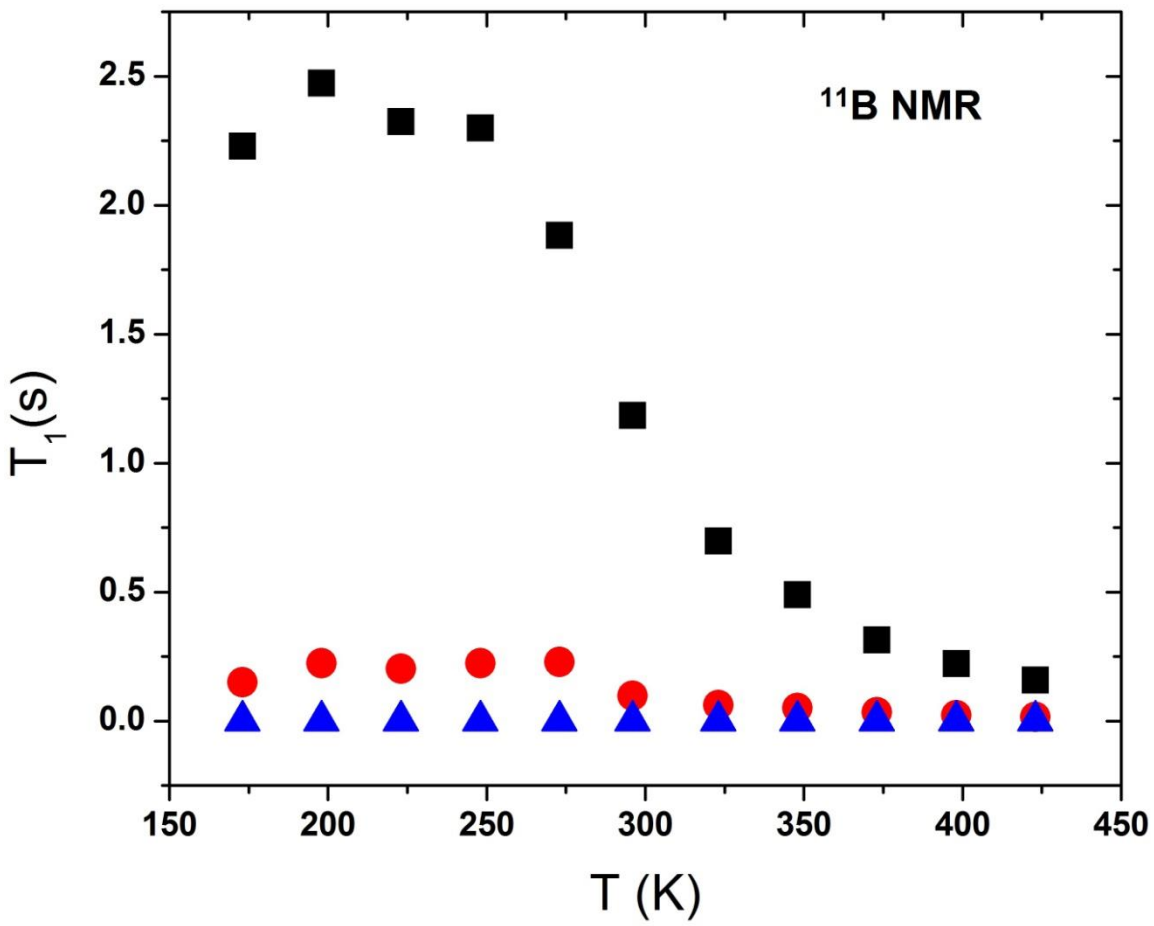

Figure 2.7: ^{11}B NMR saturation-recovery time constants T_1 for static polycrystalline metallic boron as a function of temperature from 173 K to 423 K.

References

(1) Chung, H-Y.; Weinberger, M. B.; Levine, J. B.; Cumberland, R. W.; Kavner, A.; Yang, J-M.; Tolbert, S. H.; Kaner, R. B. Synthesis of Ultra-Incompressible Superhard Rhenium Diboride at Ambient Pressure. *Science* **2007**, *316*, 436-439.

(2) Mohammadi, R.; Lech, A. T.; Xie, M.; Weaver, B. E.; Yeung, M. T.; Tolbert, S. H.; Kaner, R. B. Tungsten tetraboride, an inexpensive superhard material. *Proc. Nat. Aca. Sci.* **2011**, *108*, 10958-10962.

(3) Werheit, H.; Wehmöller, B. New peculiarities of the conductivity and photoconductivity mechanisms in β-rhombohedral boron. *J. Solid State Chem*. **2004**, *177*, 556-565.

(4) Ogitsu, T.; Gygi, F.; Reed, J.; Motome, Y.; Schwegler, E.; Galli, G. Imperfect Crystal and Unusual Semiconductor: Boron, a Frustrated Element. *J. Am. Chem. Soc*. **2009**, *131*, 1903-1909.

(5) Ogitsu, T.; Gygi, F.; Reed, J.; Udagawa, M.; Motome, Y.; Schwegler, E.; Galli, G. Geometrical frustration in an elemental solid: An Ising mode to explain the defect structure of β-rhomohedral boron. *Phys. Rev. B* **2010**, *81*, 020102.

(6) Jaeger, C.; Hemmann, F. EASY: A simple tool for simultaneously removing background, deatime and acoustic ringing in quantitative NMR spectroscopy—Part I: Basic Principle and applications. *Solid State NMR* **2014**, *57-58*, 22-28.

(7) Fenzke, D.; Freude, D.; Frohlich, T.; Haase, J. NMR intensity measurements of half-integer quadrupole nuclei. *Chem. Phys. Lett*. **1984**, *111*, 171-175.

(8) Mann, P.; Klinowski, J.; Trokiner, A.; Zanni, H.; Papon, P. Selective and Non-selective NMR Excitation of Quadrupolar Nuclei in the Solid State. *Chem. Phys. Lett*. **1988**, *151*, 143-160.

(9) Farrar, T. C.; Becker, E. D. *Pulse and Fourier Transform NMR, Introduction to Theory and Methods*; Academic Press: New York, 1971.

(10) Harris, R. K.; Becker, E. D.; De Menezes, S. M. C.; Goodfellow, R.; Granger, P. NMR NOMENCLATURE. NUCLEAR SPIN PROPERTIES AND CONVENTIONS FOR CHEMICAL SHIFTS (IUPAC Recommendations 2001). *Pure Appl. Chem*. **2001**, *73*, 1795-1818.

(11) Bishop, M.; Shahid, N.; Yang, J.; Barron, A. R. Determination of the mode and efficacy of the cross-linking of guar by borate using MAS ^{11}B NMR of borate cross-linked guar in combination with solution ^{11}B NMR of model systems. *Dalton Trans*. **2004**, *17*, 2621-2624.

(12) Hynes, T. V.; Alexander, M. N. Nuclear Magnetic Resonance Study of β-Rhombohedral Boron and Boron Carbide. *J. Chem. Phys*. **1971**, *54*, 5296-5310.

(13) Werheit, H.; A. Moldenhauer, H. On the diffusion of free carriers in β-rhombohedral boron. *J. Solid State Chem*. **2006**, 179, 2775-2778.

(14) Delaplane, R. G.; Dahlborg, U.; Granéli, B.; Fischer, P.; Lundström, T. A Neutron Diffraction Study of Amorphous Boron. *J. Non-Crystall. Solids* **1988**, ***104***, 249-252.

(15) Tsiskarishvili, G. P.; Lunström, T.; Tegenfelt, J.; Dolidze, T. V.; Tsagareishvili, G. V. Isotope Effect in β-Rhombohedral Boron. *AIP Conference Proceedings* **1991**, *231*, 280.

(16) Lee, D.; Bray, P. J.; Aselage, T. L. The NQR and NMR studies of icosahedral borides. *J. Phys.: Condens. Matter* **1999**, *11*, 4435-4450.

(17) Kubler, L.; Gewinner, G.; Koulmann, J. J.; Jaéglé, A. Magnetic Susceptibility of Pure Boron. *Phys. Stat. Sol. (B)* **1973**, *60*, 117-124.

(18) VanderHart, D. L.; Earl, W.; Garroway, A. N. Resolution in ^{13}C NMR of Organic Solids Using High-Power Proton Decoupling and Magic-Angle Sample Spinning. *J. Magn. Reson*. **1981**, *44*, 361-401.

(19) Frydman, L.; Harwood, J. S. Isotropic Spectra of Half-Integer Quadrupolar Spins from Bidimensional Magic-Angle Spinning NMR. *J. Am. Chem. Soc*. **1995**, *117*, 5367-5368.

(20) Medik, A.; Harwood, J. S.; Frydman, L. Multiple-Quantum Magic-Angle Spinning NMR: A New Method for the Study of Quadrupolar Nuclei in Solids. *J. Am. Chem. Soc*. **1995**, *117*, 12779-12787.

(21) Andrew, E. R.; Tunstall, D. P. Spin-Lattice Relaxation in Imperfect Cubic Crystals and in Non-cubic Crystals. *Proc. Phys. Soc*. 1961, **78**, 1-11.

(22) Rigamonti, A. NMR-NQR Studies of Structural Phase Transitions. *Adv. Phys*. **1984**, *33*, 115-191.

(23) Jung, J. K.; Han, O. H.; Choh, S. H. Temperature dependence of ^{23}Na NMR quadrupole parameters and spin-lattice relaxation rate in $NaNO_2$ powder. *Sol. State Comm*. **1999**, *110*, 547-552. .

(24) Okubo, N.; Igarashi, M.; Yoshizaki, R. Relaxation of ^{27}Al NMR in Aluminum Tribromide due to Raman Process. *Z. Naturforsch*. **1996**, *51a*, 277-282.

(25) Simmons, W. W.; O'Sullivan, W. J.; Robinson, W. A. Nuclear Spin-Lattice Relaxation in Dilute Paramagnetic Sapphire. *Phys. Rev*. **1962**, *127*, 1168-1178.

(26) Nisson, D. M.; Dioguardi, A. P.; Klavins, P.; Lin, C. H.; Shirer, K.; Shockley, A. C.; Crocker, J.; Curro, N. J. Nuclear magnetic resonance as a probe of electronic states of Bi_2Se_3. *Phys. Rev. B* **2013**, *87*, 195202.

(27) Tutton, A. E. The Properties of Amorphous Boron. *Nature* **1892**, *45*, 522-523.

(28) Kuhlmann, U.; Werheit, H.; Lundström, T.; Robers, W. Optical Properties of Amorphous Boron. *J. Phys. Chem. Solids* **1994**, *55*, 579-587.

(29) Berezin, A. A.; Golikova, O. A.; Kazanin, M. M.; Khomidov, T.; Mirlin, D. N.; Petrov, A. V.; Umarov, A. S.; Zaitsev, V. K. Electrical and Optical Properties of Amorphous Bonron and Amorphous Concept for β-Rhombohedral Boron. *J. Non-Crystal. Solids* **1974**, *16*, 237-246.

Chapter 3

Introduction

Metal diborides are of scientific interest due to a range of physical properties[1], including superhardness[2] and superconductivity[3]. Characteristic examples are the high hardness of ≥40 GPa displayed by rhenium diboride[2] (ReB_2) and the high temperature superconductivity at 39 K discovered in magnesium diboride[3] (MgB_2). These properties are thought to arise from or at least be influenced by the boron bonding environments[4,5] found in these materials. As a result, numerous nuclear magnetic resonance (NMR) studies have been reported[1,5-16].

One of the common structural motifs for metal diborides is that of the AlB_2 type[17], which is found for MgB_2 mentioned above. In this structure, there are planes of boron atoms forming six-membered rings similar to that of graphite. The metal atoms form planes between the boron layers and are located in the middle of the hexagonal boron rings. This configuration allows the metal to interact with twelve boron atoms, six in the plane above and six in the plane below the metal atom. The AlB_2-type structure differs from that of the ReB_2 type[15,17]. In the ReB_2-type structure, the "plane" of boron atoms is puckered, forming six-membered rings in a chair-like formation. The plane of metal atoms is arranged such that the metal is directly under a boron atom in the plane above, and above the boron in the plane below. In this arrangement the metal atom interacts with eight boron atoms, four in the plane above and four in the plane below. The different topology of the boron atoms in these two crystal structures strongly affects the conformation of the charge density of the metal atoms around the boron atom and results in interesting modifications of their band structures and Fermi surface characteristics[18].

This investigation focuses on ReB_2. While both ^{11}B spectral and spin-lattice relaxation results have been previously reported for polycrystalline ReB_2 [14], issue[15] has already been taken with one of the results. Specifically, the ReB_2 study[14] mentioned that "no visible satellite lines in a wide frequency range" were observed. This was attributed to the quadrupolar asymmetry parameter, η_q, being very large. This result in particular was surprising as the trigonal symmetry of the boron site should require the quadrupolar asymmetry parameter to be zero[7]. Indeed, this axial symmetry required by the site symmetry was later experimentally verified by a single crystal X-ray and ^{11}B NMR study[15]. In addition, the initial study[14] reported the "^{11}B NMR resonance [to be] dipolar broadened" with the ^{11}B isotropic Knight shift given with respect to an aqueous $NaBH_4$ solution reference. The current study considers an additional interaction, the shielding anisotropy, to explain the width of the central transition of the ^{11}B resonance and, following the recommendation of Nowak[19] for reporting Knight shifts[20], gives the shift according to IUPAC recommendations[21]. This report also discusses experimental considerations for how the spin-lattice relaxation measurements should be acquired and mathematically how the results should be analyzed. NMR spectroscopy, through both the shift and relaxation measurements, provides valuable information related to the crystal structure and the Fermi surface properties. Thus, the present study revisits the spectral and the nuclear relaxation parameters in order to provide a clearer picture of the electronic characteristics and the chemical bonding properties of boron atoms in ReB_2.

Materials and Methods

Rhenium diboride, ReB_2, samples were synthesized from the elements using an electric arc furnace. The samples were prepared from amorphous boron (99+%, Strem Chemicals, U.S.A) and rhenium (99.99%, CERAC Inc., U.S.A) powders, which were mixed thoroughly in an agate mortar and pestle, without any grinding. The stoichiometrically mixed powders were then cold pressed into "green pellets" in a 12mm die, at ~750mg each, by hydraulic pressing (Model #3851, Carver, USA). The pressed pellets were then loaded into an electric arc furnace, and the atmosphere was purged with ultra-high purity argon; subsequently, the samples were melted, flipped upon cooling, and re-melted to ensure thorough mixing and homogeneity. After arcing, the ingots were then crushed into fine powders using a Plattner-style tool steel mortar and pestle set (H-17270, Humboldt Mfg. Co., USA). The fine powders were sorted through a -325 Mesh sieve to remove larger particles. The samples were washed a minimum of two times with dilute HCL (0.5M) to remove any trace contaminates introduced during the grinding process. Lastly, the samples were dried to remove any residual moisture, in a vacuum furnace (70°C, a minimum of 1 hour, at ~150 torr).

The finely ground ReB_2 powders underwent X-ray diffraction (XRD) to ensure that both purity and crystal structure were synthesized and maintained. The XRD was performed on a flat stage sample holder, using an X'Pert Pro Bragg-Bentano geometry powder diffraction system (PANalytical, Netherlands). The Rhenium Diboride samples produced provided consistently clean spectra, see Figure 3.1, with a near perfect match to the ReB_2 reference (JCPDS: 00-011-0581), and verified for use in NMR experiments.

The ^{11}B NMR data were acquired with a Bruker DSX-300 spectrometer operating at a frequency of 96.29 MHz using both magic-angle spinning (MAS) and wideline techniques. The NMR samples were ground to 325 mesh to avoid radiofrequency (RF) skin-depth effects. Due to the conductivity[22] of the samples, each sample was also mixed with an equal volume of NaCl to reduce particle-to-particle contact. The mixing with NaCl provided significant improvements in both tuning of the NMR probes and in achieving higher MAS sample spinning rates.

MAS spectra of the rhenium diboride powder mixed with NaCl were acquired with a standard Bruker MAS probe using a 4-mm outside diameter zirconia rotor with a sample spinning rate of 14 kHz. The ^{11}B $\pi/2$ pulse widths for the MAS experiments were 5 μs as measured on an aqueous solution of boric acid.

A static sample of the rhenium diboride powder mixed with NaCl was placed in a standard Bruker X-nucleus wideline probe with a 5-mm solenoid coil with the sample confined to the length of the RF coil. The ^{11}B background from sodium borosilicate glass was avoided by the use of a polyimide coil support and a quartz sample tube. The ^{11}B $\pi/2$ pulse width was 5 μs as measured with an aqueous boric acid standard. For both the MAS and wideline probes, the "solid-state" ninety degree pulse width was reduced by a factor of $(I + ½)$, where I is the nuclear spin, in comparison with the ninety-degree pulse width for the same nucleus measured in solution[23,24].

The ^{11}B NMR spectra were acquired with a delay of greater than five times the spin-lattice relaxation time (T_1) as determined by a saturation-recovery technique[25]. The ^{11}B chemical shift scale was calibrated using the unified Ξ scale[21], relating the nuclear shift to the ^{1}H resonance of dilute tetramethylsilane in $CDCl_3$ at a frequency of 300.13 MHz. The reference compound for defining zero ppm is BF_3 etherate[21]. The chemical shift referencing was experimentally verified

with the ^{11}B resonance of an aqueous solution of boric acid[26] at pH = 4.4. Spectral simulations were performed with the solids simulation package (‘‘solaguide’’) in the TopSpin (Version 3.1) NMR software program from Bruker BioSpin.

Results and Discussion

The ^{11}B wideline NMR spectrum for a static sample of polycrystalline ReB_2 at ambient temperature is shown in Figure 3.2. The spectrum displays a typical quadrupolar powder pattern consisting of the central line transition and the satellite transitions as expected for a ^{11}B ($I = 3/2$) NMR spectrum. The observation of the satellite peaks provides valuable information related to the quadrupolar parameters that reflect the local charge density and symmetry at the boron site. The parameters related to the quadrupolar interaction extracted from simulation of the experimental spectrum are presented in Table 3.1. However, analysis of the one-dimensional ^{11}B spectrum provides further information.

In contrast to the earlier polycrystalline powder study of ReB_2 [14], the satellite transitions are clearly evident in Figure 3.2 with the extracted parameters characterizing the ^{11}B quadrupolar interaction in agreement with those reported in the single crystal study[15]. Specifically, the quadrupolar asymmetry parameter, η_q, is zero. This result is expected from the trigonal symmetry of the boron site[7].

The experimental data show a reduced spectral intensity for the satellite transitions in comparison with the intensities given in the spectral simulation. Such a result might be attributed to the roll off of the radiofrequency (RF) excitation pulse, *i.e.*, the RF pulse is unable to uniformly excite the entire spectral resonance. However, this same reduction of spectral intensity for the satellite transitions is also observed in the *v*ariable *o*ffset *c*umulative *s*pectra (VOCS)[27]. This

indicates that the reduced intensity does not appear to be due to the bandwidth limitation of the RF pulse. However, Abragam[28] has noted that a reduced spectral intensity may arise from the average magnitude of the quadrupolar couplings due to imperfections and dislocations within the crystallites. Indeed the authors of the single crystal study[15] of ReB_2 also noted that the relative intensities of the central and satellite line did not correspond to the expected values and attributed this discrepancy to "defects and imperfections" rather than to RF limitations.

The central transition of the ^{11}B wideline NMR spectrum shown in Figure 3.2 is asymmetric with a full width at half maximum of 20.2 kHz. This linewidth was earlier ascribed[14] to dipolar broadening. However, this observed linewidth is significantly larger than that expected from the various dipolar couplings. The dipolar couplings can be calculated[29] from the internuclear distances given in Ref. 15. With an internuclear distance of 181.5 pm for boron, the ^{11}B homonuclear dipolar coupling is 2.06 kHz while the heteronuclear coupling to ^{10}B is 0.69 kHz. With a Re-B internuclear distance of 225.8 pm, the ^{187}Re-^{11}B dipolar coupling is 0.77 kHz with the ^{11}B coupling to ^{185}Re being 0.76 kHz. This suggests that an additional nuclear interaction is responsible for the observed linewidth.

The asymmetry of the central transition along with the trigonal symmetry of the boron site suggests an axially symmetric shielding interaction similar to that observed for ^{11}B in $Al_{0.9}B_2$ [5]. For $Al_{0.9}B_2$, the ^{11}B shielding anisotropy was given as approximately 130 ppm with the authors[5] "assum[ming] coincidence of the principal axis system for the Knight shift with [the] quadrupolar interaction". Weiss and Bryce[30] have combined both ^{11}B MAS and static experiments in various magnetic fields in order to extract the parameters characterizing both the electric field gradient and the chemical shift tensor along with the relative orientations of the principal axis systems for these interactions in boronic acids and boronic esters. While available instrumentation limits the current

study to a single magnetic field strength (7 T), the approach of Weiss and Bryce[30] can be used here for ReB_2. In the case of ReB_2, the parameters of the quadrupolar interaction have been previously determined in a single crystal study[15]. ^{11}B MAS can be used to determine the isotropic shift, as shown in Figure 3.3. The same trigonal symmetry argument[7] that requires the quadrupolar asymmetry parameter to be zero (and verified in the single crystal study[15]) can also be made to require the shielding asymmetry parameter, η_s, to be zero. Although limited to a single magnetic field strength, the number of unknown spectral parameters for the quadrupolar and shielding interactions is limited to the shielding anisotropy and the Euler angles[30] relating the principal axis systems of the two interactions.

The extracted parameters of the two interactions are given in Table 3.1. The shielding anisotropy for ^{11}B in ReB_2 at 100 ppm is smaller than that observed for ^{11}B in $Al_{0.9}B_2$. For the case of the differing ReB_2 structure (relative to the AlB_2 structure), it is clear that the two principal axis systems are not coincident for ReB_2, in contrast to that assumed[5] for ^{11}B in $Al_{0.9}B_2$. The spectral simulations of the quadrupolar and shielding interactions were insensitive to the α and γ angles. The spectral simulations were quite sensitive to β, which yielded a value of 65°.

The orientation of the electric field gradient at the boron site in ReB_2 relative to the molecular framework was determined in the single crystal study[15]. With V_{zz} being the Z component of the electric field gradient tensor in its principal axis system, the Z axis is found to coincide with the c axis in the crystallographic frame, as shown in Figure 2 of Ref. 15. The crystallographic c axis is perpendicular to the planes of boron and rhenium atoms. Thus, the orientation of the shielding tensor relative to the molecular framework is known.

The observation of the satellite transitions shown in Figure 3.2 plays a significant role in determining both how a spin-lattice relaxation experiment is set up experimentally and what mathematical description is used to fit the recovery data in order to extract a spin-lattice relaxation time constant.

Theoretical descriptions of spin-lattice relaxation of half-integer quadrupolar nuclei as measured with NMR experiments have been given across the decades since NMR was first demonstrated[31-44]. There are two general mechanisms for relaxation of these quadrupolar nulcei. Quadrupolar relaxation arises from fluctuations of the electric field gradient at the nucleus, typically due to phonons[32] or molecular motion[45]. The other relaxation mechanism is magnetic, most often due to interactions with conduction charge carriers or paramagnetic centers and impurities[35,36] (with such paramagnetic centers and impurities occasionally referred to as "localized" moments[46]).

For a half-integer quadrupolar nucleus in a non-cubic single crystal, the spin-lattice relaxation recovery is typically described by a multi-exponential function[31-44]. Assuming that the crystal is oriented in the static magnetic field such that there are no accidental degeneracies of the satellite energy levels with that of the central transition, this multi-exponential recovery results as the quadrupolar interaction creates unequal energy spacings in the Zeeman interaction. Due to the unequal spacings of the energy levels, there is no common spin temperature.

For $I = 3/2$ ^{11}B, the result from Andrew and Tunstall[35] describing spin-lattice relaxation through a magnetic interaction has been applied to the measurements of numerous metal diborides[1,10,14]. However, the mathematical formulation for the spin-lattice relaxation recovery by Andrew and Tunstall[35] was derived based on the assumption of "saturation of the central line of

the resonance spectrum". The selection of radiofrequency power levels that also excite the satellite transitions, *e.g.*, spectra shown in Figure 4 of Ref. 1, suggests that the Andrew and Tunstall[35] description may not be appropriate to the chosen experimental conditions. Indeed, the error in applying such spin-lattice relaxation recovery equations to actual experimental data arising from an incorrect assumption of the initial conditions of the magnetization has been discussed[47]. Yesinowski[48] has shown for the *I = 3/2* case where all transitions, both satellite and central, have been saturated, the analysis of the relaxation behavior predicts a single-exponential recovery. With the choice of experimental parameters that observes both the central and satellite transitions as shown in Figure 3.2, the spin-lattice relaxation behavior of ReB_2 was re-examined in the present study.

Note also that the derivation of Andrew and Tunstall[35] was for a single crystal oriented in a magnetic field such that there were no degeneracies among the energy levels. However, many of the ^{11}B spin-lattice relaxation studies use polycrystalline samples for the experimentally practical reason of avoiding issues with the RF skin depth effects. Phenomenologically the spin-lattice relaxation recoveries of these half-integer quadrupolar nuclei in polycrystalline samples are frequently observed to be a single exponential[49,50]. In polycrystalline materials, Slichter and coworkers[51] have pointed out that the apparent relaxation time from the entire sample is simply "an effective average over the assembly of crystallites".

The use of MAS offers potential advantages in NMR studies of polycrystalline materials by improving sensitivity due to the narrowing of resonances and allowing the observation of resonances arising from atomic sites with differing shifts. Unfortunately, MAS is known to significantly shorten the spin-lattice relaxation recovery times for half-integer quadrupolar nuclei in solids[52-54]. This is qualitatively explained by MAS causing the satellite and central transition

frequencies to overlap during sample rotation due to the orientational dependence of the quadrupolar interaction. Nevertheless, Yesinowski[48] has recently shown that accurate spin-lattice relaxation measurements for half-integer quadrupolar nuclei can still be made under MAS conditions in order to take advantage of the MAS spectrum by applying a train of saturation pulses asynchronous to the MAS in order to use the overlapping of the satellite and central transition during the sample rotation so that both central and satellite transitions are saturated. However, the sample temperature of conductive samples[55] under MAS has been shown to be significantly higher than that expected from the frictional heating of MAS[56,57] alone. For that reason, the saturation recovery spin-lattice relaxation results reported here were acquired with static samples.

The ambient temperature relaxation data are shown in Figure 3.4. The spin-lattice relaxation time constant, T_1, was extracted via the fit of a single exponential to the experimental data as per the previous paragraphs and yielded a value of 4.2s. It should be noted that single exponential behavior of the relaxation recovery data is in agreement with that predicted by Yesinowski[48], when both the satellite and central transitions are saturated. The T_1 of 4.2 s also indicates the high purity of the sample. In the synthesis of transition metal diborides such as ReB_2, elemental boron is sometimes a side product that is difficult to separate. However, elemental boron[58] has shown a multi-exponential ^{11}B spin-lattice saturation recovery with observed time constants on the order of microseconds, 100 ms, and 500 ms. Even though the observed ^{11}B shifts for ReB_2 and elemental boron are quite similar, the absence of such short times constants in the recovery data as observed for elemental boron indicates the absence of elemental boron at levels detectable by NMR in the ReB_2 sample.

The spin-lattice relaxation rate, $1/T_1$, is a well-established microscopic probe of the density of states at the Fermi level as well as of the Fermi surface characteristics[1,10]. The analysis of the

T_1 data as a function of temperature is shown in Figure 3.5. The NMR results, in agreement with the transport data[22] and with the resistivity data[22], indicate a Korringa[59] mechanism that shows the metallic character of the rhenium diboride. Such a result indicates that the magnetic interaction dominates the quadrupolar relaxation mechanism over this temperature range[48].

As might be expected, given the interesting physical properties of ReB_2, numerous calculation studies have been reported[15,60-64]. These studies show that the density of states at the Fermi level is dominated by the Re-*5d* and B-*2p* orbitals. There is little or no contribution from the *s*-orbital of the boron. As a result, the Fermi contact interaction is small[14]. The Knight shift[20] is thus also expected to be small, in agreement with the measured shift of 5 ppm (Table I) that is almost in the middle of the range of boron chemical shifts. The boron spin-lattice relaxation is expected to be dominated by other orbital and dipolar mechanisms arising from the *p* states[14]. The interest in repeating the ^{11}B spin-lattice relaxation measurements for ReB_2 arose due to absence of experimental information regarding the RF excitation and the observation of satellite transitions while applying the Andrew-Tunstall model, appropriate for selective excitation of the central transition given in previous studies[1,14]. For the present study, using the relaxation rate values shown in Figure 3.5 yields a Korringa product (T_1T) equal to 1154 sK. This is significantly larger than the value of 280 sK previously reported[14]. Using the same assumptions as given in Ref. 14 to calculate the contribution to the density of states from the *p* orbitals yields a smaller value of 0.18 states/eV than the 0.24 given in Table 3.1 of Ref. 14. Interestingly, the Korringa product reported here is about two times higher than in the cases of OsB_2[11] (600 sK) and RuB_2[11] (680 sK). This domination of the relaxation by the *p* orbitals is also shown in the Korringa ratio[11], $R=\frac{K^2T_1T}{S}$, where $S \equiv \left(\frac{\gamma e}{\gamma n}\right)\left(\frac{h}{8\pi 2kb}\right)$ where γ_e and γ_n are the gyromagnetic ratios for the electron and nucleus,

respectively. For ReB_2, the Korringa ratio of $R = 0.01$ is calculated from $S = 2.57\times10^{-6}$ sK for the case of the boron nucleus and the $K_{iso} = 5$ ppm (see Table 3.1). A value of $R = 0.01$ indicates that the character of the electronic wavefunctions around the Fermi level is mainly a non-*s* type, driven by the 2*p* boron states in agreement with recent first-principle calculations on ReB_2[52].

While the previous relaxation study[14] reported relaxation measurements only at ambient temperature and below, the current study extended measurements to higher temperatures. In this high temperature regime, a departure from Korringa behavior was observed above 360 K. A first-principle study[52] on ReB_2 predicts the opening of a pseudo-gap at the Fermi level. However, this feature has never yet been detected experimentally. The reduction of the Korringa product above 360 K could be a signature of the opening of a gap in the density of states at the high temperature regime. This unexpected observation remains unclear and further experiments are in progress in order to uncover this unknown relaxation behavior in ReB_2.

Conclusions

A complete analysis of the ^{11}B NMR parameters from one-dimensional spectra from static and MAS experiments demonstrates that the two principal axis systems of the electric field gradient and the shielding tensor are not coincident for ReB_2. This result differs from that assumed for $Al_{0.9}B_2$. Appropriate selection of radiofrequency and acquisition parameters allows the observation of both central and satellite transitions in a polycrystalline sample. As a result, the initial conditions for a saturation recovery spin-lattice relaxation experiment now allow an accurate extraction of the spin-lattice relaxation time constant of ReB_2. Contrary to a previous NMR study[14], the satellite transition lines are visible and the boron site has an axial symmetry. Accurate measurements of the relaxation rates as a function of temperature allow the character of the

electronic wavefunctions around the Fermi surface of the ReB_2 to be characterized. In addition, the spin-lattice relaxation measurements were extended to temperatures above ambient. An upturn of the $1/T_1$ above 360 K could be assigned to a theoretically predicted pseudo-gap in the density of states of ReB_2. Further work remains to be done in order to shed light on this observation.

Table 3.1. ^{11}B NMR Quadrupolar and Shielding Parameters of ReB_2[a]

	δ_{iso}[b] (ppm)	C_Q[c] (MHz)	υ_Q[d] (MHz)	η_q[e]	δ_{11}[b] (ppm)	δ_{22}[b] (ppm)	δ_{33}[b] (ppm)	δ_{iso}[a] (ppm)	ζ_{csa}[f] (ppm)	η_s[g]	Ω[h] (ppm)	κ[i]	α (^{0})	β (^{0})	γ (^{0})
ReB_2 Static	5	0.550	0.275	0	105	-45	-45	5	100	0	150	-1	0	65	0
ReB_2 MAS	7.6			0						0					

[a]Spectral parameters obtained from simulations in Figure 3.3.

[b]Chemical shifts referenced to the unified Ξ scale [9].

[c]Quadrupolar coupling constant { $e^2qQ/\hbar$}.

[d]Quadrupolar frequency $\{(3e^2qQ)/[2I(2I-1)\hbar]\}$.

[e]η = asymmetry $\{\{0 \leq \eta \leq 1\}$.

[f] $\zeta_{csa} = \delta_{33} - \delta_{iso}$.

[g] $\eta = (\delta_{22} - \delta_{11})/\zeta_{csa}$.

[h] $\Omega = |\delta_{33} - \delta_{11}|$.

[i] $\kappa = 3(\delta_{22} - \delta_{iso})/\Omega$.

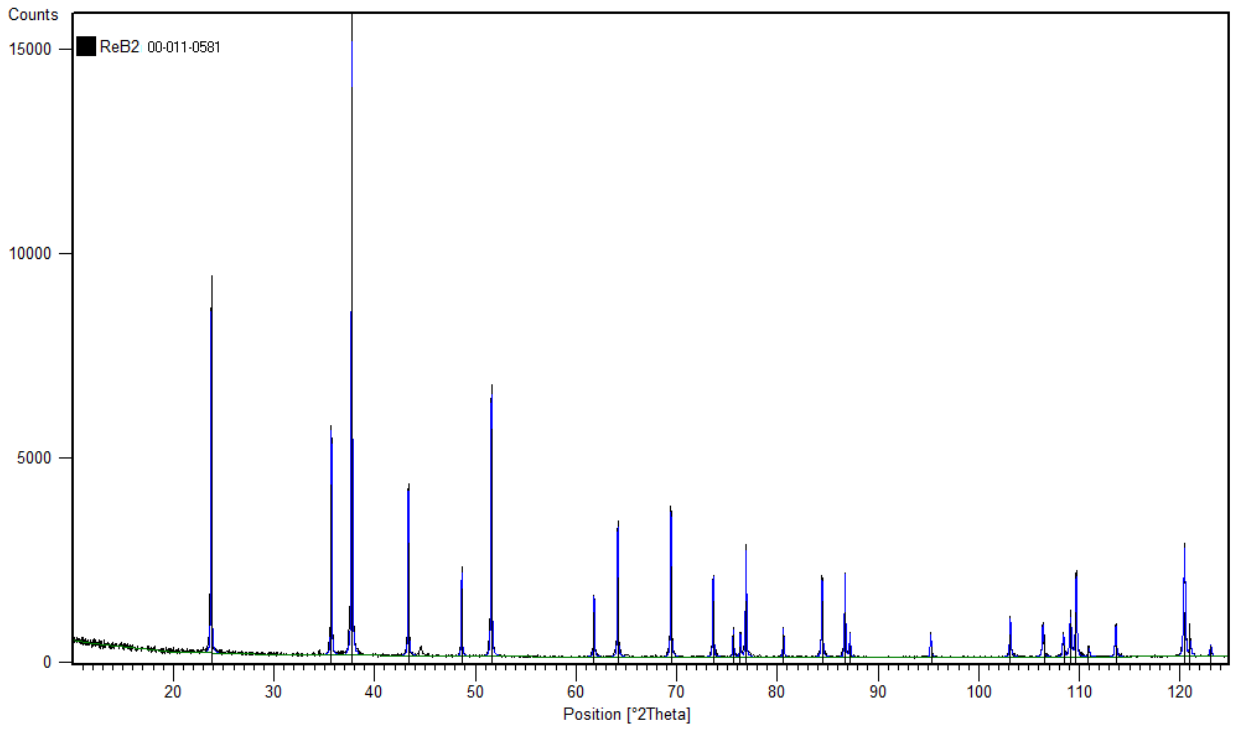

Figure 3.1: ReB_2 XRD Spectra for the powders produced for the NMR experiments. The match between experimental data and the reference are near perfect. Experimentally collected data are seen as the blue line, with the JCPDS reference displayed as the black "stick" lines.

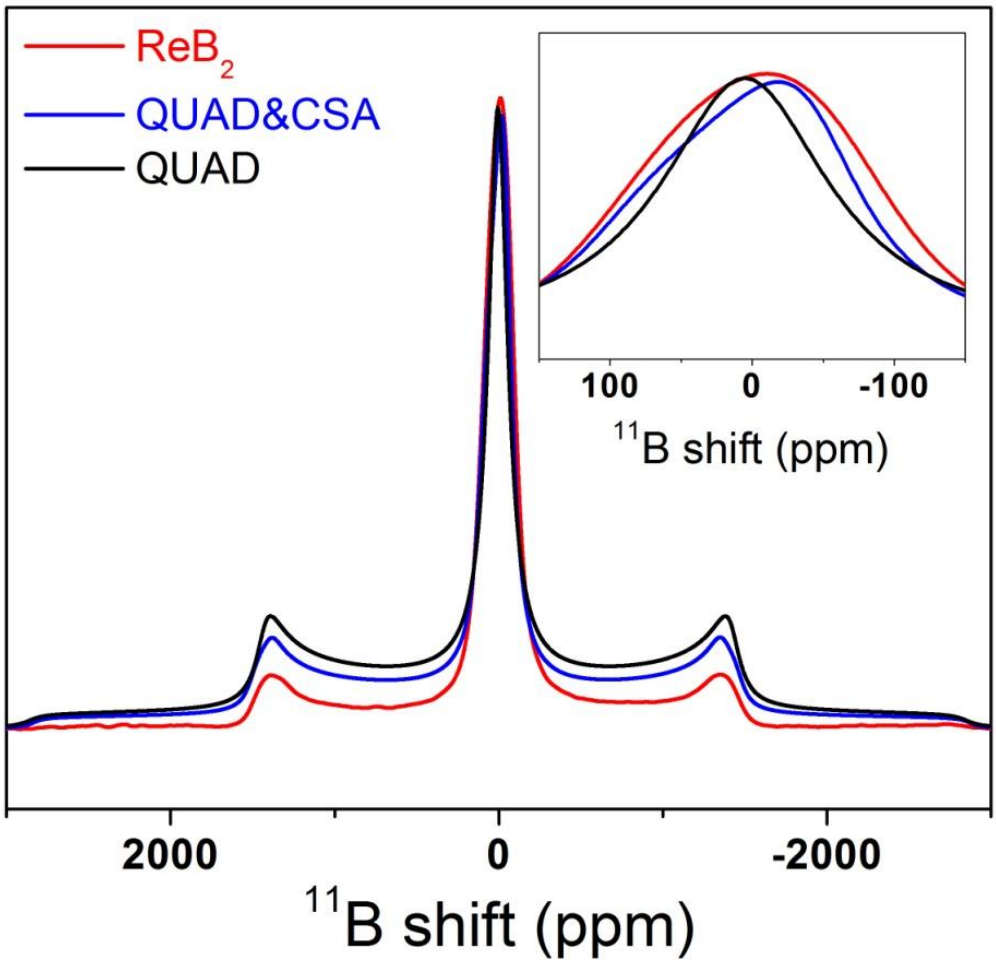

Figure 3.2: ^{11}B NMR spectrum of a static polycrystalline sample of ReB_2 at ambient temperature (red line). The spectrum displays the central line and the satellite transitions expected for the *I* = 3/2 ^{11}B nucleus (black line). The optimal simulation of the spectrum is achieved after the introduction of the shielding anisotropy (CSA) contribution in addition to the quadrupolar term (QUAD) as shown in the inset (blue line).

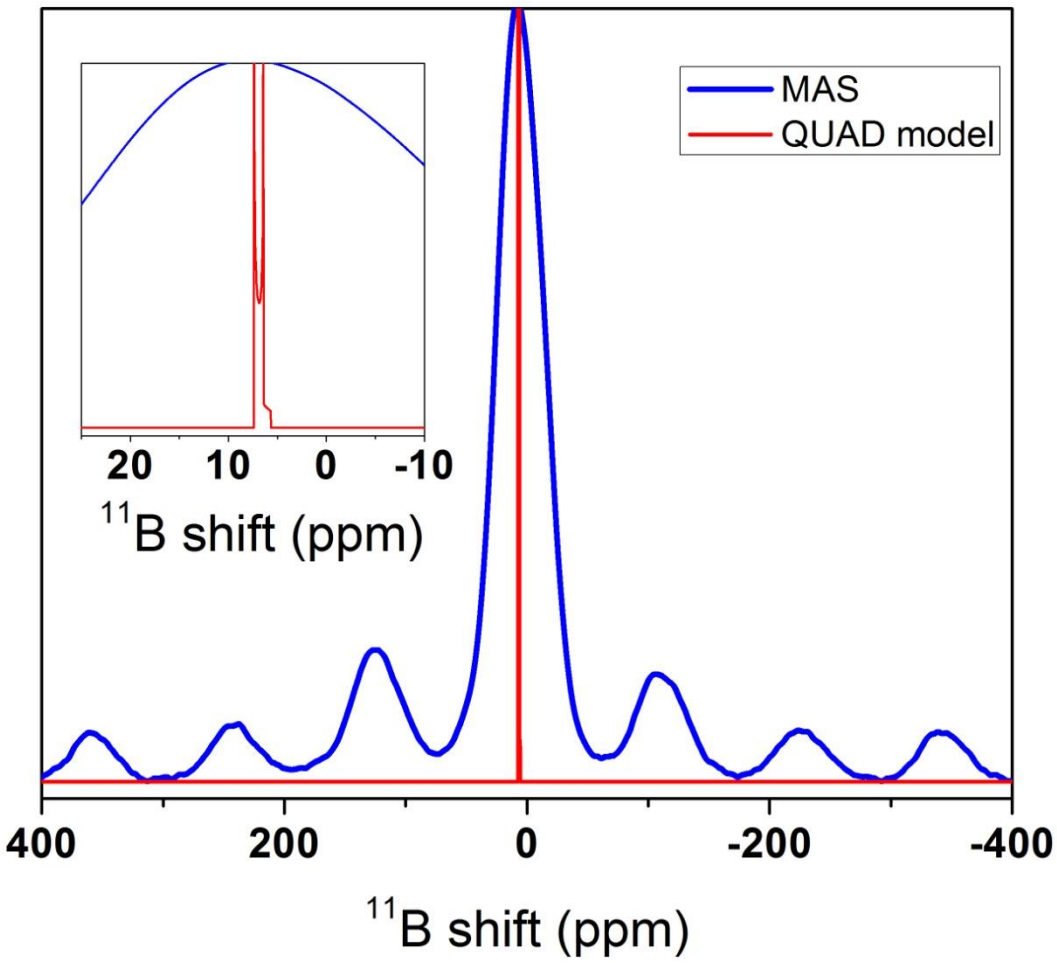

Figure 3.3: ^{11}B MAS NMR spectrum of ReB_2 at ambient temperature (blue line). The second order quadrupolar interaction is insufficient alone to describe the remaining observed linewidth under MAS.

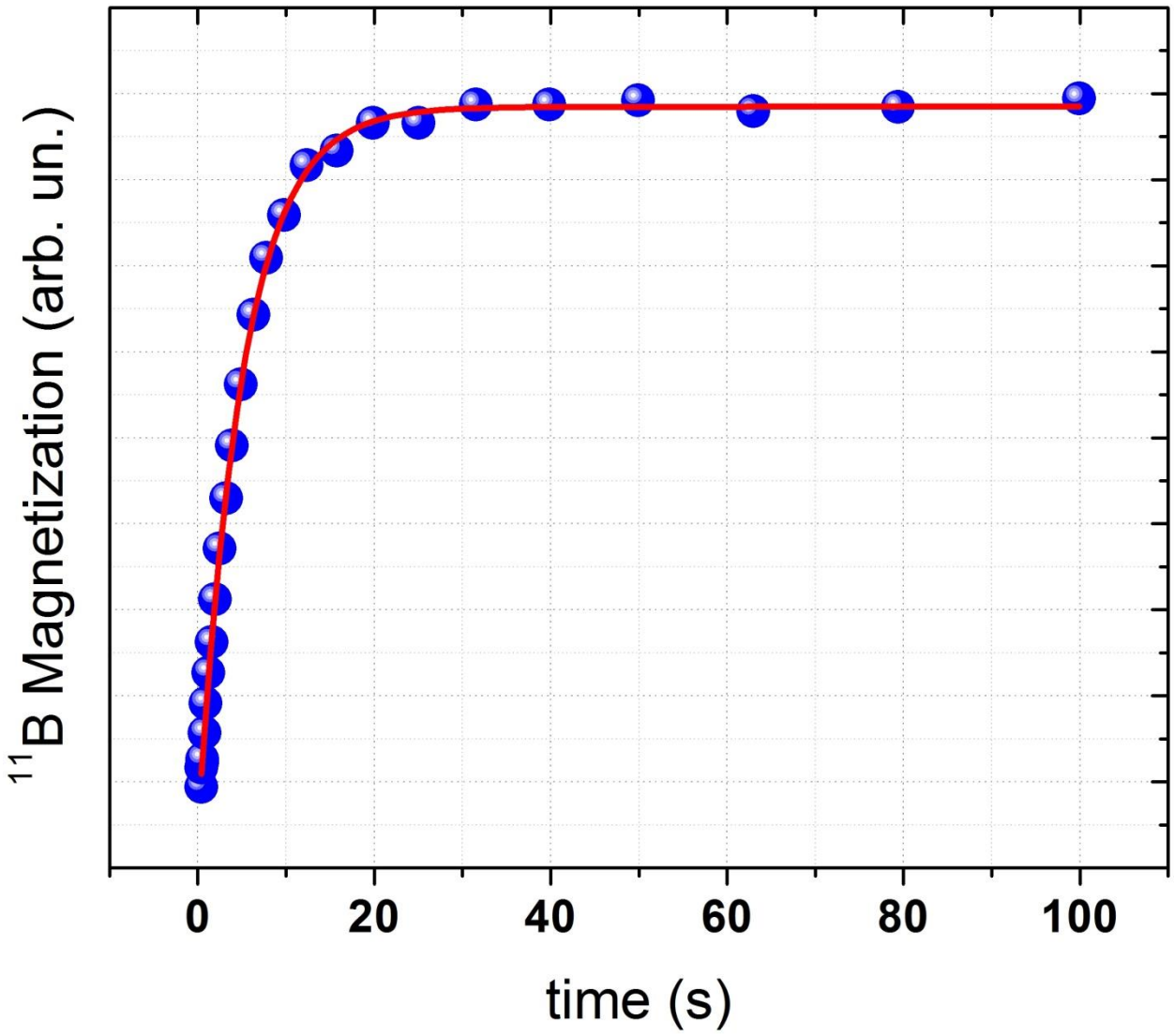

Figure 3.4: ^{11}B saturation recovery data at 295 K. The smooth line in red shows the fit of a single exponential to the data.

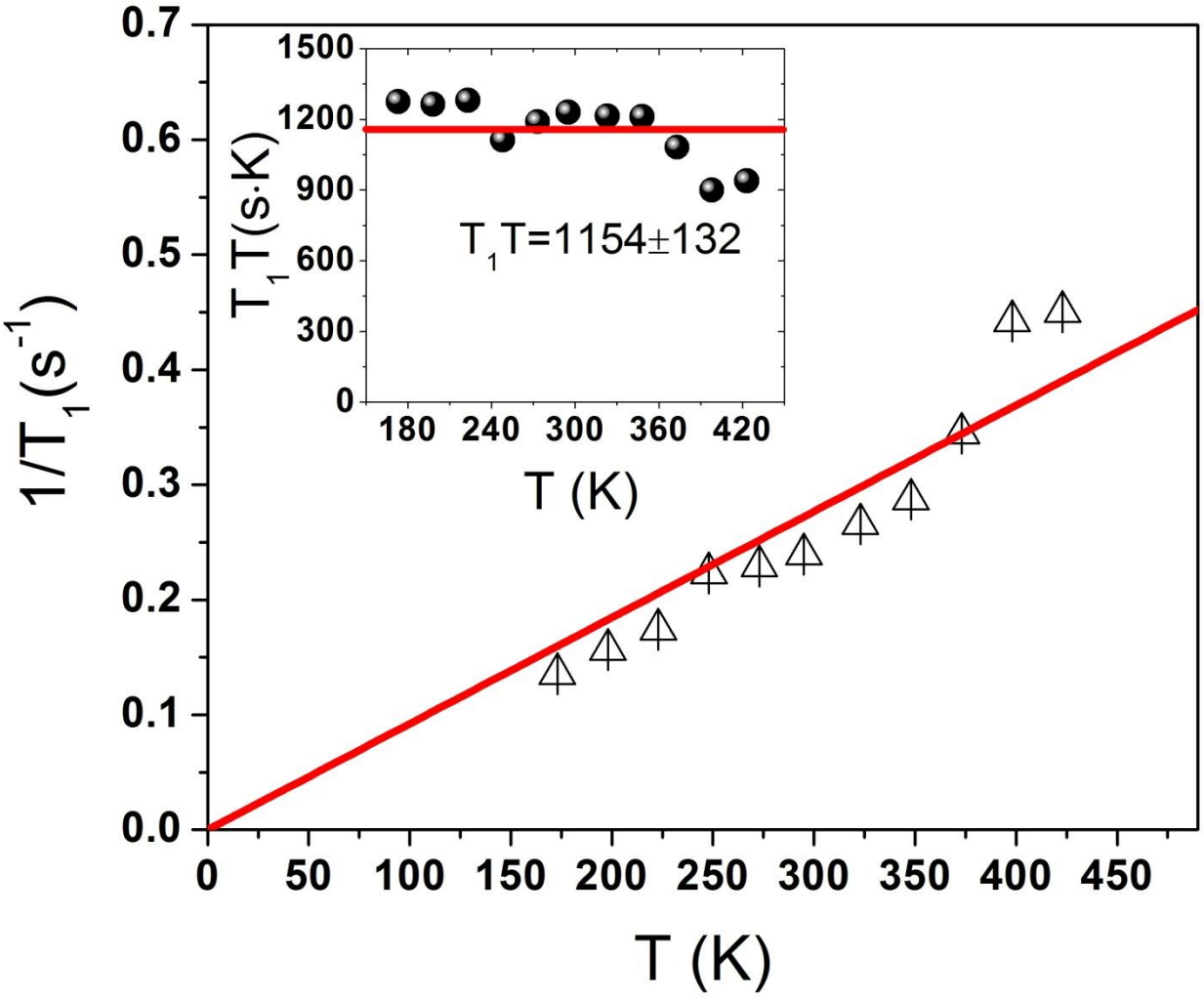

Figure 3.5: Temperature dependence of the ^{11}B nuclear spin-lattice relaxation rate in ReB_2. The dashed red line shows the Korringa behavior with the product T_1T = 1154 sK across the entire temperature range.

References

(1) Lue, C. S; Lai, W. J. NMR Study of B-*2p* Fermi-level Density of States in the Transition Metal Diborides. *Phys. Stat. Sol. (B)* **2005**, *242*, 1108-1112.

(2) Chung, H-Y.; Weinberger, M. B.; Levine, J. B.; Cumberland, R. W.; Kavner, A.; Yang, J-M.; Tolbert, S. H.; Kaner, R. B. Synthesis of Ultra-Incompressible Superhard Rhenium Diboride at Ambient Pressure. *Science* **2007**, *316*, 436-439.

(3) J. Nagamatsu, J.; Nakagawa, N.; Muranaka, T.; Zenitani, Y.; Akimitsu, J. Superconductivity at 39 K in magnesium diboride, *Nature* **2001** (Mar 1), *410* (6824), 63-64.

(4) Kawano, A.; Mizuta, Y.; Takagiwa, H.; Maranaka, T.; Akimitsu, J. The Superconducitivity in Re-B System, *J. Phys. Soc. Japan* **2003**, *72*, 1724 -1728.

(5) Bukhardt, U.; Gurin, V.; Haarmann, F.; Borrmann, H.; Schnelle, W.; Yaresko, A.; Grin, Y. On the electronic and structural properties of aluminum diboride $Al_{0.9}B_2$, *J. Solid State Chem.* **2004**, *117*, 389 -394.

(6) Silver, A. H.; Bray, P. J. NMR Study of Bonding in Some Solid Boron Compounds, *J. Chem. Phys.* **1960**, *32*, 288 -292.

(7) Silver, A. H.; Kushida, T. Nuclear Magnetic Resonance in Transition-Metal Diborides, *J. Chem. Phys.* **1963**, *38*, 865 -872.

(8) Barnes, R. G.; Creel, R. B. Chromium-like Antiferromagnetic Behavior of CrB_2, *Phys. Lett*. **1969**, *29A*, 203 -204.

(9) Carter, G. C.; Swartz, J. C. Nuclear Magnetic Resonance Knight Shifts and Quadrupole Effects in Transition Metal Diborides, *J. Phys. Chem. Solids* **1971**, *32*, 2415 – 2421.

(10) Baek, S. H.; Suh, B. J.; Pavarini, E.; Borsa, F.; Barnes, R. G.; Bud'ko, S. L.; Canfield, P. C. NMR spectroscopy of the normal and superconducting states of MgB_2 and comparison to AlB_2, *Phys. Rev. B* **2002**, *66*, 104510.

(11) Suh, B. J.; Zong, X.; Singh, Y.; Niazi, A.; Johnston, D. C. ^{11}B NMR in the layered diborides OsB_2 and RuB_2, *Phys. Rev. B* **2007**, *76*, 144511.

(12) Michioka, C.; Itoh, Y.; Yoshimura, K.; Watabe, Y.; Kousaka, Y.; Ichikawa, H.; Akimitsu, J. NMR studies of single crystal chromium diboride, *J. Magnetism and Magnetic Materials* **2007**, *310*, e620 –e622.

(13) Su. T. H.; Lue, C. S.; Kuo, Y. K. NMR and Seebeck coefficient studies of the electronic band structure in $NB_{1-x}B_2$, *J. Appl. Phys*. **2008**, *104*, 093705.

(14) Lue, C. S.; Tao, Y. F.; Su, T. H. Comparative NMR investigation of the Re-based borides, *Phys. Rev. B* **2008**, *78*, 033107.

(15) Żogał, O. J.; Fojud, Z.; Herzig, P.; Pietraszko, A.; Lyashchenko, A. B.; Jurga, S.; Paderno, V. N. Crystal structure, electric field gradient, and electronic charge densities in ReB_2: A single crystal x-ray, ^{11}B nuclear magnetic resonance, and first-principles study, *J. Appl. Phys*. **2009**, *106*, 033514.

(16) Beckett, P.; Denning, M. S.; Heinmaa, I.; Dimri, M. C.; Young, E. A.; Stern, R.; Carravetta, M. High resolution ^{11}B NMR of magnesium diboride using cryogenic magic angle spinning, *J. Chem. Phys*. **2012**, *137*, 114201.

(17) Burdett, J. K.; Canadell, E.; Miller, G. J. Electronic Structure of Transition-Metal Borides with the AlB_2 Structure, *J. Am. Chem. Soc*. **1986**, *108*, 6561 – 6568.

(18) Aydin, S.; Simsek, M. First-principles calculations of MnB_2, TcB_2, and ReB_2 within the ReB_2-type structure, *Phys. Rev. B,* **2009**, *80*, 134107.

(19) Nowak, B. Comment of the reference compound for chemical shift and Knight shift determination of ^{209}Bi nuclei, *Solid State NMR* **2015**, *65-67*, 49 -50.

(20) W. D. Knight, W. D. Nuclear magnetic resonance shift in metals, *Phys. Rev*. **1949**, *76*, 1259 - 1260.

(21) Harris, R. K.; Becker, E. D.; De Menezes, S. M. C.; Goodfellow, R.; Granger, P. NMR NOMENCLATURE. NUCLEAR SPIN PROPERTIES AND CONVENTIONS FOR CHEMICAL SHIFTS (IUPAC Recommendations 2001), *Pure Appl. Chem*. **2001**, *73*, 1795 - 1818.

(22) Levine, J. B.; Nguyen, S. L.; Rasool, H. I.; Wright, J. A.; Brown, S. E.; Kaner, R. B. Preparation and properties of Metallic, Superhard Rhenium Diboride Crystals, *J. Am Chem. Soc*. **2008**, *130*, 16953 – 16958.

(23) Fenzke, D.; Freude, D.; Frohlich, T.; Haase, J. NMR Intensity Measurements of Half-integer Quadrupole Nuclei. *Chem. Phys. Lett*. **1984**, *111*, 171-175.

(24) Mann, P.; Klinowski, J.; Trokiner, A.; Zanni, H.; Papon, P. Selective and Non-selective NMR Excitation of Quadrupolar Nuclei in the Solid State. *Chem. Phys. Lett*. **1988**, *151*, 143-160.

(25) Farrar, T. C.; Becker, E. D. *Pulse and Fourier Transform NMR, Introduction to Theory and Methods*; Academic Press: New York, 1971.

(26) Bishop, M.; Shahid, N.; Yang, J.; Barron, A. R. Determination of the Mode and Efficacy of the Cross-linking of Guar by Borate using MAS ^{11}B NMR of Borate Cross-linked Guar in Combination with Solution ^{11}B NMR of Model Systems. *Dalton Trans*. **2004**, *17*, 2621-2624.

(27) Massiot, D.; Farnan, I.; Gautier, N.; Trumeau, D.; Trokiner, A.; Coutures, J.P. ^{71}Ga and ^{69}Ga nuclear magnetic resonance study of β-Ga_2O_3: resolution of four- and six-fold coordinated Ga sites in static conditions, *Solid State NMR* **1995,** *4*, 241–248.

(28) Abragam, A. *Principles of Nuclear Magnetism*, Oxford University Press, Oxford **1961**.

(29) Levitt, M. H. *Spin Dynamics Basics of Nuclear Magnetic Resonance*, John Wiley and Sons, Chichester **2001**.

(30) Weiss, J. W. E.; Bryce, D. L. A Solid-State ^{11}B NMR and Computational Study of Boron Electric Field Gradient and Chemical Shift Tensors in Boronic Acids and Boronic Esters, *J. Phys. Chem. A* **2010**, *114*, 5119 – 5131.

(31) R. V. Pound, R. V. Nuclear Electric Quadrupole Interactions in Crystals, *Phys. Rev*. **1950**, *79*, 685 - 702.

(32) J. Van Kranendonk, J. Theory of Quadrupolear Nucelar Spin-Lattice Relaxation, *Physica* **1954**, 20, 781 - 800.

(33) Mieher, R. L, Nuclear Relaxation via Quadrupole Coupling, *Phys. Rev. Lett*. **1960**, *4*, 57 - 59.

(34) Wikner,E. G, Blumberg, W. E.; Hahn,E. L. Nucelar Quadrupole Spin-Lattice Relaxation in Alkali Halides, *Phys. Rev*. **1960**, *118*, 631 – 639.

(35) Andrew, E. R.; Tunstall, D. P. Spin-Lattice Relaxation in Imperfect Cubic Crystals and in Non-cubic Crystals, *Proc. Phys. Soc*. **1961** *78*, 1 - 11.

(36) W. W. Simmons, W. W; O'Sullivan, W. J.; Robinson, W. A. Nuclear Spin-Lattice Relaxation in Dilute Paramagnetic Sapphire, *Phys. Rev*. **1962**, *127*, 1168 - 1178.

(37) D. G. Hughes, D. G. Nuclear quadrupole spin-lattice relaxation in single crystals for I = 3/2, *Proc. Phys. Soc*. **1966**, *87*, 953 - 965.

(38) Narath, A. Nuclear Spin-Lattice Relaxation in Hexagonal Transition Metals: Titanium, *Phys. Rev*. **1967**, *162*, 320332.

(39) Narath, A.; Weaver, H. T. Effects of Electron-Electron Interactions on Nuclear Spin-Lattice Relaxation Rates and Knight Shifts in Alkali and Noble Metals, *Phys. Rev*. **1968**, *175*, 373 - 382.

(40) Stepišnik, J. Magnetic-Resonance Relaxation and Saturation of Quadrupole-Interacting Spin System, *Phys. Rev. B* **1973**, *7*, 3250 - 3255.

(41) M. I. Gordon, M. I.; Hoch, J. J. R., Quadrupolar spin-lattice relaxation in solids, *J. Phys. C: Solid State Phys*. **1978**, *11*, 783 - 795.

(42) Rega, T. Separation of magnetic and quadrupolar relaxation rates from spin-latice recovery laws at short times with illustration in a high-Tc superconductor, *J. Phys.: Condens. Matter* **1991**, *3*, 1871 - 1876.

(43) Suter,A.; Mali, M.; Roos, J.; Brinkmann, D. Mixed magnetic and quadrupolar relaxation in the presence of a dominant static Zeeman Hamiltonian, *J. Phys.: Condens. Matter* **1998**, *10*, 5977 - 5994.

(44) Yesinowksi, J. P. Magnetization-recovery experiments for static and MAS-NMR of I=3/2 nuclei, *J. Magn. Reson*. **2006**, *180*, 147 - 161.

(45) Sharma, R.; Taylor, R. E.; Bouchard, L-S. Intramolecular Ligand Dynamics in d15-(PPh3)-Capped Gold Nanoparticles Investigated by ^{2}H NMR, *J. Phys. Chem. C* **2011**, *115*, 3297 - 3303.

(46) Nisson, D. M.; Dioguardi, A. P.; Klavins, P.; Lin, C. H.; Shirer, K.; Shockley, A. C.; Crocker, J.; N. J. Curro, N. J. Nuclear magnetic resonance as a probe of electronic states of Bi_2Se_3, *Phys. Rev. B* **2013**, *87* , 195202.

(47) McDowell, A. F. Magnetization-Recovery Curves for Quadrupolar Spins, *J. Magn. Reson., Series A* **1995**, *113*, 242 - 246.

(48) Yesinowski, J. P. Finding the true spin-lattice relaxation time for half-integral nuclei with non-zero quadrupole couplings, *J. Magn. Reson*. **2015**, *252*, 135 – 144.

(49) Rigamonti, A. NMR-NQR Studies of Structural Phase Transitions, *Adv. Phys*. **1984**, *33*, 115 - 191.

(50) Fanciulli, M.; Corti, M. ^{11}B NMR and relaxation study of boron nitride, *Phys. Rev. B* **1995**, *52*, 11872 - 11878.

(51) Sakaie, K. E.; Slichter, C. P.; Lin, P.; Jaime, M.; Salamon, M. B. ^{139}La spectrum and spin-lattice relaxation measurements of $La_{2/3}Ca_{1/3}MnO_3$ in the paramagnetic state, *Phys. Rev. B* **1999**, 59, 9382 - 9391.

(52) Woessner, D. E.; Timken, H. K. C. The Influence of MAS on Spin-Lattice Relaxation Curves and Nuclear Spin Excitation of Half-Integer Spin Quadrupolar Nuclei in Solids, J. *Magn. Reson*. **1990**, *90*, 411 - 419.

(53) Kwak, H-T.; Srinivasan, P.; Quine, J.; Massiot, D.; Gan, Z. Satellite transition rotational resonance of homonuclear quadrupolar spins: magic-angle effect on spin-echo decay and inversion recovery, *Chem. Phys. Lett*. **2003**, *376*, 75 - 82.

(54) Thurber, K. R.; Tycko, R. Measurement of sample temperatures under magic-angle spinning from the chemical shift and spin-lattice relaxation rate of ^{79}Br in KBr powder, *J. Magn. Reson*. **2009**, *196*, 84 - 87.

(55) Yesinowski, J. P.; Ladouceur, H. D.; Purdy, A. P.; Miller, J. B. Electrical and Ionic Conductivity Effects on Magic-Angle Spinning Nuclear Magnetic Resonance Parameters of CuI, *J. Chem. Phys*. **2010**, *133*, 234509.

(56) Bielecki, A.; Burum, D. P. Temperature Dependence of ^{207}Pb MAS Spectra of Solid Lead Nitrate. An Accurate, Sensitive Thermometer for Variable-Temperature MAS. *J. Magn. Reson. A* **1995**, *116*, 215 − 220.

(57) Neue, G.; Dybowski, C. Determining Temperature in a Magic angle Spinning Probe using the Temperature Dependence of the Isotropic Chemical Shift of Lead Nitrate. *Solid State NMR* **1997**, *7*, 333 − 336.

(58) Turner, C. L; R. E. Taylor, R. E.; Kaner, R. B. ^{10}B and ^{11}B NMR Study of Elemental Boron, *J. Phys. Chem. C* **2015**, *119*, 13807 - 13813.

(59) Korringa, J. NUCLEAR MAGNETIC RELAXATION AND RESONNANCE LINE SHIFT IN METALS, *Physica* **1950**, *XVI*, 601 - 610.

(60) Hao, X.; Xu, Y.; Wu, JZ.;Zhou, D.; Liu, X.; Cao, X.; Meng, J. Low-compressibility and hard materials ReB_2 and WB_2: Prediction from first-principles studies, *Phys. Rev. B* **2006**, *74*, 224112.

(61) Zhou, W.; Wu, H.; Yildirim, T. Electronic, dynamical, and thermal properties of ultra-incompressible superhard rhenium dirboride: A combined first-principles and neutron scattering study, *Phys. Rev. B* **2007**, *76*, 184113.

(62) Long Run; Dai Ying; Jin Hao; and Huang Baibiao. Structural, Elastic, and Electronic Properties of ReB_2: A First-Principles Calculation, *Research Letters in Physics* **2008**, 293517.

(63) Li, Y-L.; Zhou, G-H.; Zeng, Z. All-electron study of ultra-incompressible superhard material ReB_2: structural and electronic properties, *Chinese Phys. B* **2009**, *18*, 4437 - 4442.

(64) Pan, Y.; Zheng, W. T.; Guan, W. M.; Zhang, K. H.; Yu, S. S.; Hu, X. Y. Effect of boron vacancies on mechanical properties of ReB_2 from first-principles calculation, *Comp. Mater. Sci.* **2014**, 82, 12 – 16.

Chapter 4

Introduction

As a class of materials, transition metal diborides exhibit an interesting range of physical properties, including "high melting point, high hardness, high thermal conductivity, high chemical stability, low electrical resistivity, and low mass density"**Error! Bookmark not defined.**, with ^{11}B nuclear magnetic resonance (NMR) studies of these materials going back decades[2,3]. Numerous transition metal diborides are considered "superhard" materials[4], which are characterized by high valence-electron density and bond covalency and are also typically metallic.

Many metal diborides adopt an AlB_2-type structure[5]. In such a structure, the boron atoms form layers of connected planar hexagonal rings. The metal is typically found in a layer of its own above and under the center of the boron rings and is 12-coordinate with the rings above and below the metal. The other common structure is the ReB_2-type[5]. In this type of structure, the six-membered boron rings are puckered, *i.e.*, have a chair configuration. The metal is typically directly above and below one boron atom and is additionally bonded with the three nearest-neighbor boron atoms in that layer. The metal is 8-cordinate with the rings above and below the metal. However, transition metal diborides exhibit a variety of structures. For example, at least five different binary compounds formed between tungsten and boron have been reported: W_2B, WB (two crystal structures), WB_2, W_2B_4 (formerly described as W_2B_5) and WB_4 [6-9]. For the transition metal diboride phase of interest in the present study, WB_2, assumes a structure in which the boron layers alternate between AlB_2-type and ReB_2-type arrangements[8], as shown in Figure 4.1.

Transition metal borides can display many different bonding environments as the interactions between boron and metal atoms vary within the different structures. Numerous ^{11}B NMR studies of various metal diborides with both the AlB_2-type[10-17] and ReB_2-type[18-20] structures have been reported in the literature. However, the present ^{11}B NMR study is the first to investigate boron sites arising from the differing structural motif of WB_2. Both boron shifts and quadrupolar frequencies of the sites are characterized. The mechanism for the ^{11}B spin-lattice relaxation is also determined.

Materials and Methods

Tungsten diboride, WB_2, was first synthesized from the elements, amorphous boron (Strem, USA) and tungsten powder (Strem, USA), using an electric arc furnace in a manner similar to that previously described for ReB_2 [20]. The structure was confirmed by powder X-ray diffraction.

The ^{11}B NMR data were acquired with a Bruker DSX-300 spectrometer using both magic-angle spinning (MAS) and wideline techniques at a frequency of 96.29 MHz. Additional ^{11}B MAS data were acquired with a Bruker AV-500 spectrometer at 160.48 MHz to investigate the magnetic field dependence of the observed spectra. The NMR samples were ground to -325 mesh (<44 μm) to minimize radiofrequency (RF) skin-depth effects. In addition, each sample was also mixed with an equal volume of NaCl to reduce particle-to-particle contact. The mixing with NaCl provided significant improvements in both tuning of the NMR probes and in achieving higher MAS sample spinning rates.

MAS spectra of the tungsten diboride powder mixed with NaCl were acquired with a standard Bruker MAS probe using a 4-mm outside diameter zirconia rotor with a sample spinning rate of either 5 or 14 kHz. The ^{11}B $\pi/2$ pulse width for the MAS experiments was 5 μs as measured

on an aqueous solution of boric acid. The ^{11}B background from the boron nitride stator in the MAS probe was minimized by the use of the *E*limination of *A*rtifacts in NMR *S*pectroscop*Y* (EASY) pulse sequence[21].

A static sample of the tungsten diboride powder mixed with NaCl was placed in a standard Bruker X-nucleus wideline probe with a 5-mm solenoid coil with the sample confined to the length of the RF coil. The use of a polyimide coil support and a quartz sample tube removed any ^{11}B background that might arise from the presence of sodium borosilicate glass. The ^{11}B $\pi/2$ pulse width was 5 μs as measured with an aqueous boric acid standard. For both the MAS and wideline probes, the "solid-state" ninety degree pulse width was reduced by a factor of $(I + ½)$, where I is the nuclear spin, in comparison with the ninety-degree pulse width for the same nucleus measured in solution[22,23].

All ^{11}B NMR spectra were acquired with a delay of five times the spin-lattice relaxation time (T_1) as determined by a saturation-recovery technique[24]. In the various ^{11}B saturation-recovery experiments, three different saturation methods were used. For static samples, these included either single-pulse saturation or a saturation pulse sequence of ($p3_x$ – 210 μs - $p3_y$ – 350 μs - $p3_{-x}$ – 283 μs - $p3_{-y}$ – 111 μs-). The RF pulse p3 was 4.25 μs, a value experimentally determined by minimizing the remaining signal 100 μs after the saturation pulse sequence. The intervening times between the p3 pulses in the saturation sequence are chosen to be longer than the time for the NMR signal to dephase into the noise of the baseline after a single pulse. For the ^{11}B saturation-recovery experiment with MAS at a rate of 5 kHz, the method of pulsing asynchronously to the sample spinning given by Yesinowski[25] was used.

The ^{11}B chemical shift scale was calibrated using the unified Ξ scale[26], relating the nuclear shift to the ^{1}H resonance of dilute tetramethylsilane in $CDCl_3$ at a frequency of 300.13 MHz. The reference compound for defining zero ppm is BF_3 etherate[26]. The chemical shift referencing was experimentally verified with the ^{11}B resonance of an aqueous solution of boric acid[27] at pH = 4.4. Spectral simulations were performed with the solids simulation package (''solaguide'') in the TopSpin (Version 3.1) NMR software program from Bruker BioSpin.

Results and Discussion

As mentioned in the Introduction, tungsten diboride, WB_2, has a structure in which the boron layers alternate between AlB_2-type and ReB_2-type arrangements. The structures for both the AlB_2-type and ReB_2-type arrangements along with that for WB_2 are shown in Fig. 4.1.

Figure 4.2 shows the ^{11}B NMR spectrum of a static polycrystalline sample of WB_2 at 296 K. The full width at half-height of this resonance at 19.7 kHz is quite similar to that observed for the central transition in ReB_2 [20] of 20.2 kHz and in AlB_2 of 21.8 kHz. However, the difference in spectra for these compounds is more readily apparent in the MAS experiments. High resolution MAS experiments for ReB_2 [20] and AlB_2 [11,12,16-17] yield single, featureless ^{11}B resonances for the central transitions. However, the ^{11}B MAS spectra for WB_2 as a function of magnetic field strength and sample spinning rates shown in Fig. 4.3 reveal the presence of four different groups of boron sites, resonating around 18, 2.5, -16, and -60 ppm.

There is evidence to indicate that the ^{11}B quadrupolar coupling constants for all ^{11}B resonances in each of these four groups of sites are quite small. First, a trend in the ^{11}B quadrupolar frequencies is observed for metal diborides having an AlB_2-type structure. As the metal is taken from further down the groups (families) in the periodic table, the reported ^{11}B quadrupolar

frequencies in the diborides become smaller in magnitude. These quadrupolar frequencies, taken from the literature [1,3,12,28], are given in Table 4.1. This experimental trend has also been reproduced in theoretical calculations of the electric field gradients in metal diborides[29]. However, while this trend is observed for AlB_2-type structures, the WB_2 sample in this study does have a different structure. Nevertheless, the following experimental observations obtained in the current study further suggest rather small ^{11}B quadrupolar frequencies.

Specifically, in contrast to the ^{11}B results for AlB_2[10-17] and ReB_2[20], *v*ariable *o*ffset *c*umulative *s*pectra (VOCS)[30] used in this study were unsuccessful in observing any satellite transitions. Thus the width of the ^{11}B resonance observed from the static sample may place an upper limit on the magnitude of the quadrupolar frequency (ν_Q). This approach has been used previously in the study of transition metal diborides[1] to indicate small quadrupolar frequencies.

Additional experimental evidence for rather small quadrupolar frequencies is also indicated by the ^{11}B spin-lattice relaxation behavior. While the spin-lattice relaxation results are discussed in more detail below, the pertinent point here is that within experimental error the saturation-recovery data at 296 K are fit well by a single exponential that yields a time constant of 2.3 s ± 0.5 s. This same time constant is obtained for saturation-recovery experiments on a static sample whether one uses single-pulse saturation or pulse-train saturation and is also obtained in a MAS experiment using the saturation technique of Yesinowski[25]. For the RF pulses used in this study, we have observed such behavior for ^{11}B in ReB_2[20], which has a ^{11}B quadrupolar frequency of 0.275 MHz. For ReB_2, the RF pulses were able to excite the full ^{11}B spectral resonance, including the satellite transitions. However, a multi-exponential recovery for single-pulse saturation is expected if the quadrupolar frequency is large enough such that the RF pulse only saturates the central transition[31]. Using this same RF power for ^{11}B measurements in AlB_2, which has a ^{11}B quadrupolar

frequency of 0.540 MHz[12], the saturation recovery required the multi-exponential model of Andrew and Tunstall[31] in order to be well fit by the function. As a single exponential recovery is experimentally observed for ^{11}B in WB_2, the quadrupolar frequency in WB_2 must be small enough that the RF is able to fully excite both satellite transitions as well as the central transition.

The ^{11}B MAS spectrum obtained with a spinning rate of 14 kHz in a 11.7 T magnetic field, expanded to show the three groups of the four resonances, is given in Fig. 4.4. The two resonances around 18 and -16 ppm show features which one might assume arise from the second-order quadrupolar interactions. The spectrum has been fit with the summation of three simulations of the central transition for the spin-3/2 ^{11}B nucleus. The simulations of the three sites, all of which are assumed to have trigonal symmetry (and hence an asymmetry of zero) yield the following: a site with an isotropic shift of 25.0 ppm with a ν_Q of 1.25 MHz, a second site with an isotropic shift of 2.9 ppm with a ν_Q of 0.27 MHz, and a third site with an isotropic shift of -10 ppm with a ν_Q of 1.31 MHz. The difficulty with this interpretation of attributing these ^{11}B spectral features in the MAS spectrum to second-order quadrupolar interactions is that the magnitudes of ν_Q of 1.25 MHz and 1.31 MHz are at odds with the spin-lattice relaxation behavior discussed above. The RF used in this study is not capable of fully exciting the full ^{11}B spectrum of nuclei with quadrupolar frequencies of $\geq$ 0.540 MHz. In such a situation using single-pulse saturation, a multi-exponential saturation recovery would be expected[31]. However, as noted above, the ^{11}B saturation recovery data are well fit by a single exponential. This result suggests that the spectral features observed in the MAS spectrum in Fig. 4.4 more likely arise from further unresolved ^{11}B sites rather than from such interactions having larger quadrupolar frequencies. Such an explanation is consistent with all sites having small quadrupolar coupling constants. Otherwise, the satellite transitions from such large quadrupolar interactions would likely have been observed in the *VOCS* spectrum.

Finally, were the spectral features in the MAS spectrum in Fig. 4.4 to truly arise from second-order quadrupolar interactions rather than from overlapping isotropic peaks, -one would expect the magnetic field dependence to be evident in Fig. 4.3. Specifically the resonances at 7.05 Tesla should be both broadened and shifted relative to corresponding peaks at 11.75 Tesla. This is not observed.

As mentioned in the Introduction, the WB_2 phase in the current study possesses a more complex structure than either the AlB_2-type or ReB_2-type metal diborides. Klesnar and co-workers[32] have also encountered complex structures with MoB_2. Specifically, they noted[32] "of the transition metals, molybdenum is unique in forming 'diborides' of both the simple AlB_2 structure type and a more complex type". The reason for bringing molybdenum diboride into this conversation is the proposal by Kiesling[33] of an additional boron atom at the center of the six-membered boron rings. As mentioned by Albert and co-workers[34], "The unusual coordination sphere of the additional, centering boron atom raised controversy in the literature. Further structural investigations led to contradictory results, including partial[32] and absent[35,36] occupation of the boron atom position in question". The ^{11}B MAS results shown in Fig. 4.3 provide spectroscopic evidence in support of "partial occupation" of this site. Specifically, the small lower frequency, *i.e.*, "upfield", resonance at -60 ppm is consistent with such an interpretation. Such "upfield" shifts arising from ring-current effects have been experimentally demonstrated with the ^1H NMR spectra of 1,4-polymethylenene benzenes[37]. For the particular case of transition metal diborides, the "upfield" shift arising from the ring current effect from the six-membered boron ring in VB_2 has been previously calculated[3] to be -55 ppm. The experimental observation of the smaller resonance "upfield" around -60 ppm is consistent with this interpretation of the shift arising from a ring current.

The other three ^{11}B resonances in the MAS spectrum in Fig. 4.3 arise from the "more complex type"[32] of structure also found for WB_2. In order to elucidate bond distances for structural comparisons between AlB_2, WB_2, and ReB_2, the VESTA[38] software package was used; reference patterns from the Joint Committee for Powder Diffraction Standards (JCPDS) were used to simulate the models, respectively. For the AlB_2 structure, there is a single metal-boron bond distance. The bonding in ReB_2 differs from that of AlB_2 in that the metal is typically directly above and below one boron atom and is additionally bonded with the three nearest-neighbor boron atoms in that layer. Nevertheless, in ReB_2, all the metal-boron bond distances are quite similar. The metal directly above or below a boron atom has a bond distance of 2.24(3) angstroms while the bond distance from the metal to the three nearest-neighbor boron atoms is only 2.24(5) angstroms. These metal-boron bond distances in AlB_2 and ReB_2 differ from those observed for WB_2. The tungsten-boron bond distance to all the boron atoms in the flat hexagonal boron ring is 2.32 angstroms. For the other layer with the tungsten directly below a boron atom, the tungsten-boron bond distance is 2.24(7) angstroms. However, there is a lengthening of the tungsten bond distance to the three nearest-neighbor atoms to 2.33(2) angstroms. In this puckered boron ring, the boron-boron bond distance is 1.85 angstroms while the boron-boron bond distance is the flat hexagonal ring is 1.72 angstroms. These differing bond distances give rise to the additional ^{11}B resonances observed for WB_2 as opposed to the single ^{11}B resonances observed for both AlB_2 and ReB_2.

Above, it was also mentioned that the ^{11}B spin-lattice relaxation recovery is consistent with a smaller quadrupolar coupling constant. Specifically, the RF used in this study is able to fully excite both satellite transitions and the central transitions so that recovery is well characterized by a single exponential function. Fig. 4.5 shows the ^{11}B spin-lattice relaxation behavior as a function

of temperature. The NMR results indicate a Korringa[39] mechanism that illustrates the metallic character of the tungsten diboride. Spin-lattice relaxation results from MAS experiments with Yesinowski's[25] technique indicate that all four groups of resonances relax at the same rate, consistent with the observation of a single exponential recovery observed with the static sample.

Since the hyperfine interaction with the conduction charge carriers provides the spin-lattice relaxation in a Korringa[39] mechanism, it may seem surprising initially that, given the different bonding modes for the boron atoms that yield four different spectral resonances, only a single relaxation time is experimentally measured for ^{11}B. Such a result is likely to arise from the high natural abundance (80.1%) and relatively high magnetogyric ratio for ^{11}B [26]. These physical attributes can yield homonuclear dipolar interactions on the order of several kHz in ReB_2[20]. Homonuclear dipolar couplings are known to give rise to a single relaxation time for abundant spin systems. As an example, deuteration of the amino group in γ-glycine[40] yields a ^{1}H T_1 of 78 s for the remaining methylene protons while a single ^{1}H T_1 of only 4 s is measured for the fully protonated material. The comparison demonstrates how effectively the motion of the amine group acts as a relaxation mechanism through dipolar couplings. Similarly the boron dipolar couplings in WB_2, both the ^{11}B homonuclear dipolar coupling and the heteronuclear dipolar coupling to ^{10}B, can explain the observation of a single relaxation time in the static sample resulting from the most effective Korringa relaxation mechanism.

As noted previously, the measured spin-lattice relaxation rates under MAS also indicated that, within experimental error, ^{11}B resonances from all four groups also displayed a single rate of relaxation. We have previously shown for the abundant ^{1}H spin system in ammonium dihydrogen phosphate[41] that high speed MAS did not allow the protons to reach a common spin temperature, *i.e.*, the ^{1}H T_1's of the ammonium and acid species differed beyond experimental error. The

observation of a single relaxation time for ^{11}B in WB_2 under MAS may indicate that although four groups of boron resonances are observed, the hyperfine interactions of the boron atoms in the four groups of resonances with the conduction charge carriers are all quite similar. Alternatively, MAS may not completely suppress the dipolar interactions for the quadrupolar ^{11}B.

Conclusions

The structure of tungsten diboride, WB_2, differs from those of metal diborides with AlB_2- or ReB_2-type structures that have been previously studied by ^{11}B NMR spectroscopy. As opposed to the single ^{11}B resonance reported for the metal diborides having those AlB_2- or ReB_2-type structures, four groups of ^{11}B resonances are found for WB_2. There is also ^{11}B NMR spectral evidence to support the proposal by Kiesling in 1947 of an additional boron atom at the center of some of the six-membered boron rings. The ^{11}B quadrupolar frequencies of all four groups of resonances in WB_2 are all quite small (<20 kHz), in keeping with the trend observed for ^{11}B in metal diborides having the AlB_2-structure as the metal is taken from further down the groups (families) in the periodic table.

Table 4.1. ^{11}B Quadrupolar Frequencies[a], ν_Q, of various Metal Diborides

Compound	ν_Q (MHz)	*Compound*	ν_Q (MHz)	*Compound*	ν_Q (MHz)
MgB_2[b]	0.835			AlB_2[c]	0.540
Groups IVB		*Groups VB*		*Groups VIB*	
TiB_2[d]	0.180	VB_2[e]	0.210	CrB_2[e]	0.320
ZrB_2[d]	0.060	NbB_2[e]	<0.0035	MoB_2[e]	0.115
HfB_2[d]	<0.030	TaB_2[e]	<0.0025	WB_2[f]	small

[a]Quadrupolar frequency $\{(3e^2qQ)/[2I(2I-1)\hbar]\}$.

[b]Ref. 28.

[c]Ref. 12.

[d]Ref. 1.

[e]Ref. 3.

[f]This work. WB_2 differs from the other compounds in this table by not having an AlB_2-type structure.

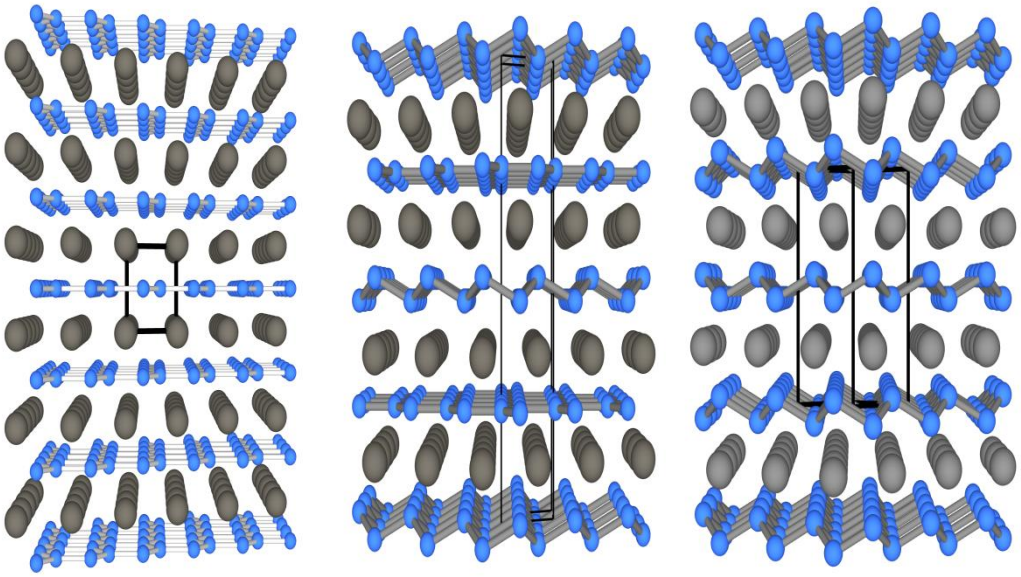

AlB_2-type **WB_2** **ReB_2-Type**

Figure 4.1: Structures of different metal diborides (color online). The metal atoms are represented by the larger gray spheres with the boron atoms by the smaller blue spheres. The black rectangles represent the unit cell.

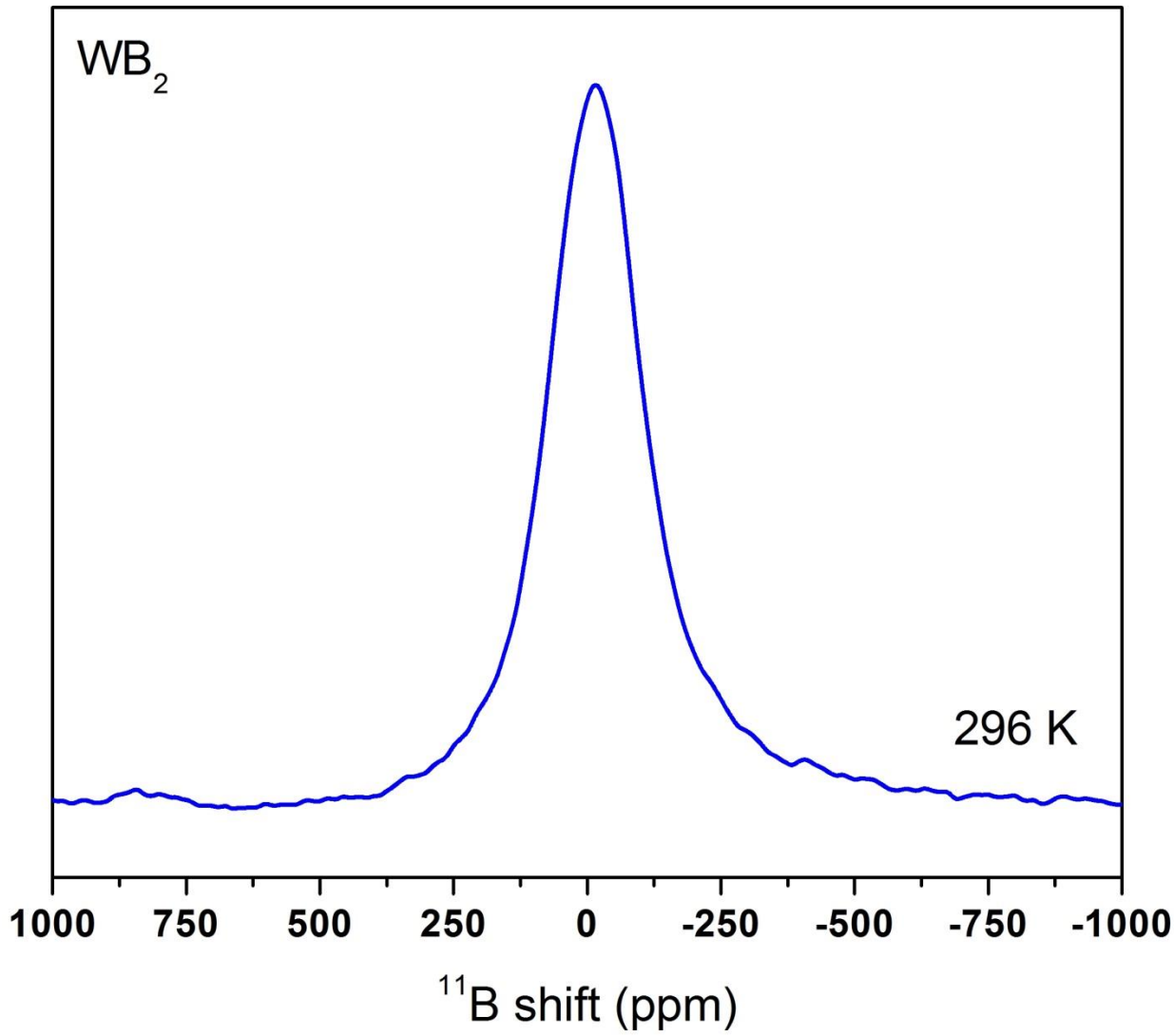

Figure 4.2: ^{11}B NMR spectrum of a static sample of WB_2 at 296 K. No evidence of the satellite transitions were observed in the *VOCS* spectrum.

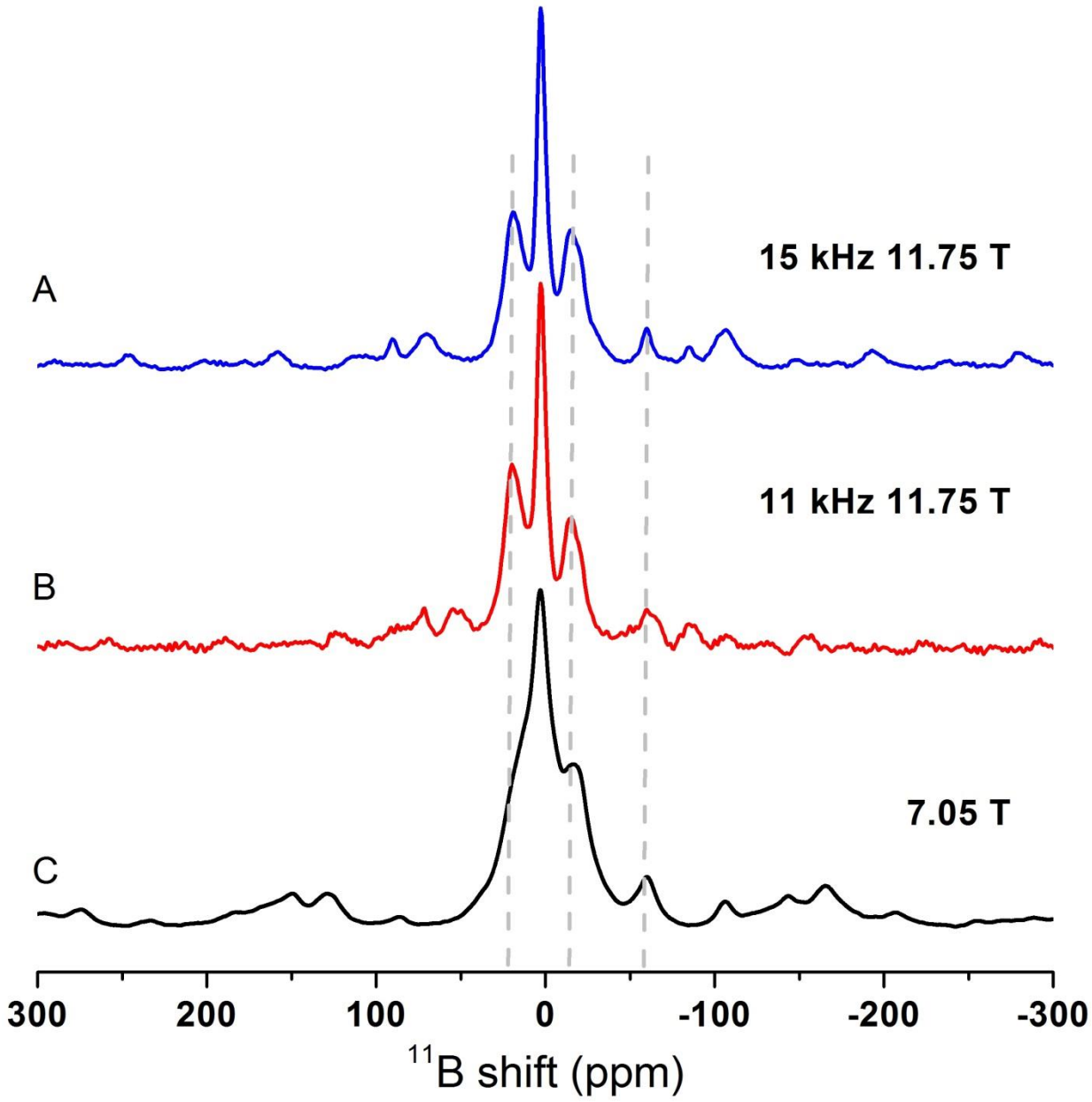

Figure 4.3: ^{11}B MAS spectra of polycrystalline WB_2 at ambient temperature as function of magnetic field and sample rotation rate. Four groups of isotropic resonances are observed. The peaks beyond ±60 ppm are spinning sidebands.

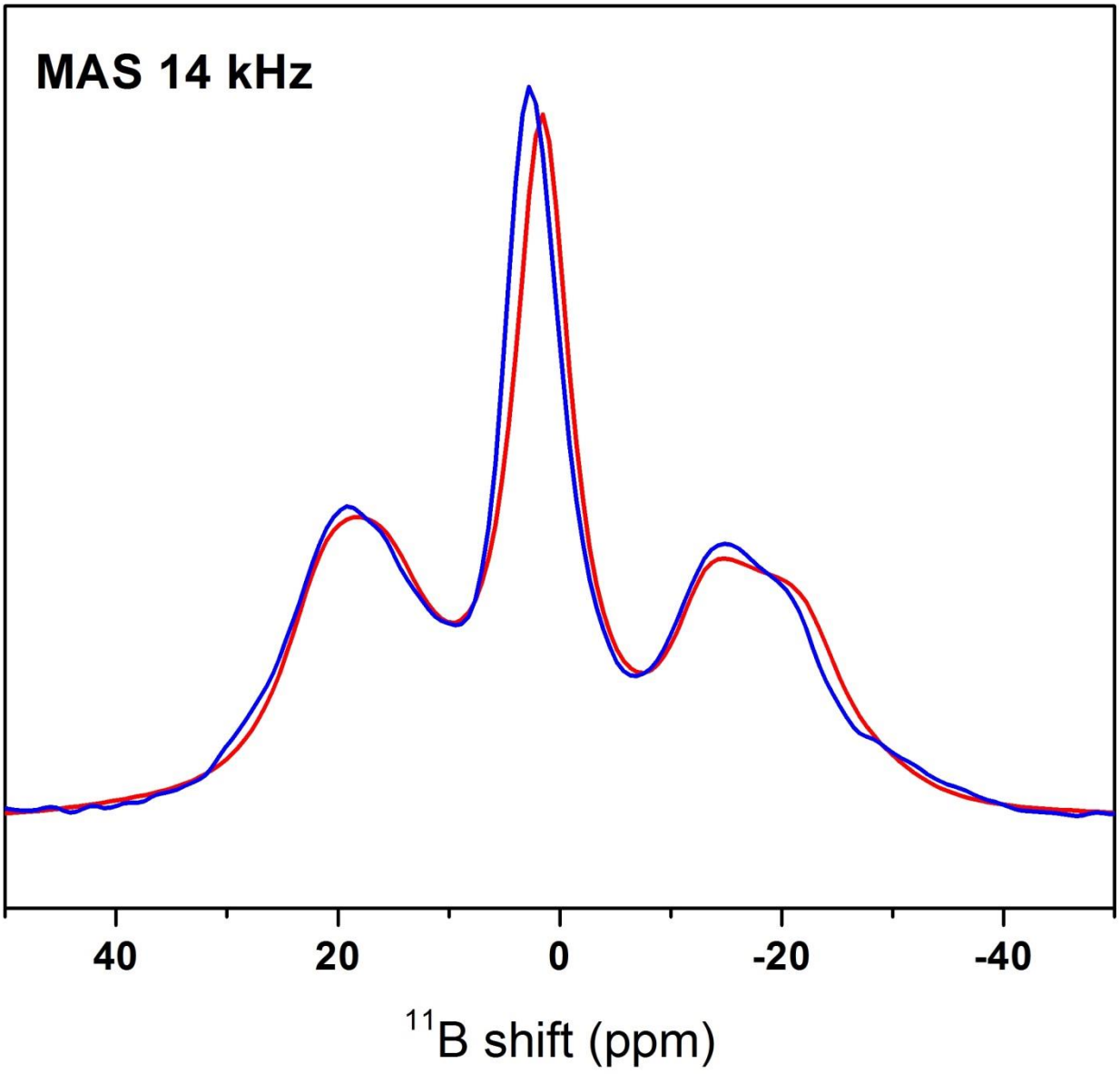

Figure 4.4: ^{11}B MAS spectra of polycrystalline WB_2 at ambient temperature showing the central transitions of three resonances. The smooth red line is the summation of simulations of the central transition for each of the three sites.

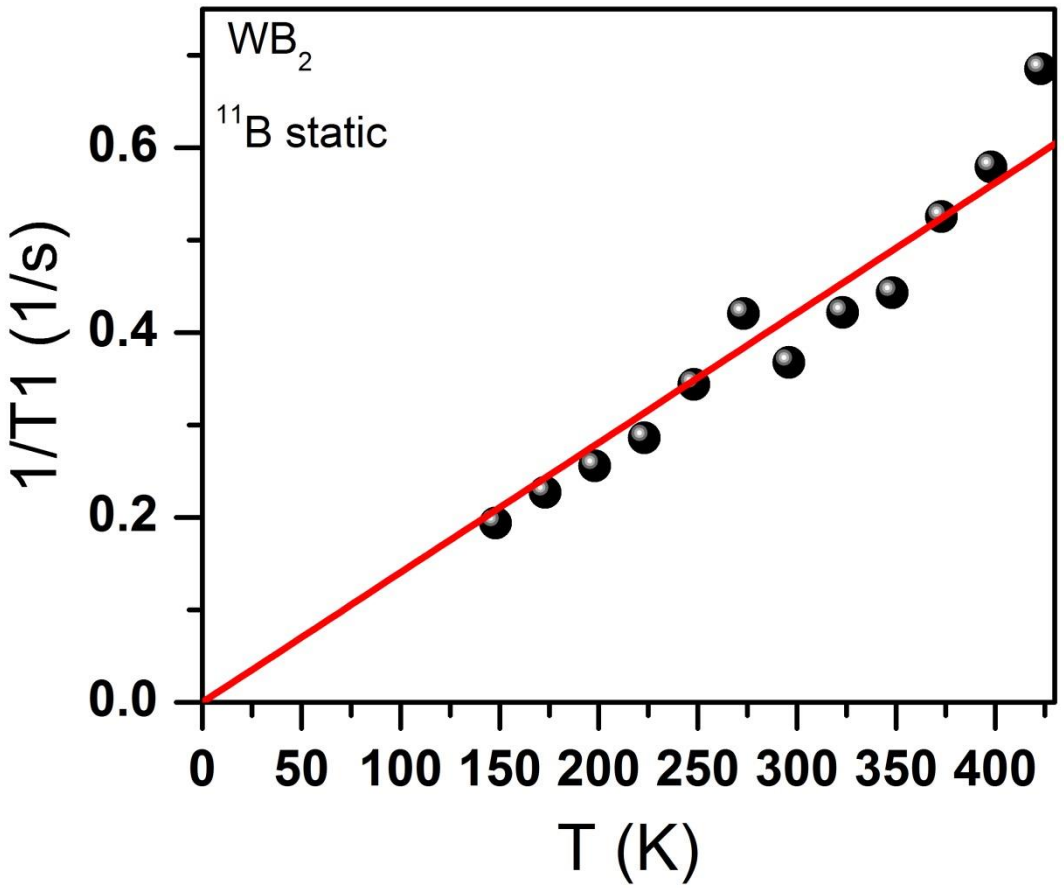

Figure 4.5: The ^{11}B spin-lattice relaxation rate of a static sample of polycrystalline WB_2 as a function of temperature displays a Korringa relationship.

References

(1) Lue, C. S; Lai, W. J. NMR Study of B-*2p* Fermi-level Density of States in the Transition Metal Diborides. *Phys. Stat. Sol. (B)* **2005**, *242*, 1108-1112.

(2) Silver, A. H.; Bray, P. J. NMR Study of Bonding in Some Solid Boron Compounds. *J. Chem. Phys.* **1960**, *32*, 288-292.

(3) Silver, A. H.; Kushida, T. Nuclear Magnetic Resonance in Transition-Metal Diborides. *J. Chem. Phys*. **1963**, 38, 865-872.

(4) Chung, H-Y.; Weinberger, M. B.; Levine, J. B.; Cumberland, R. W.; Kavner, A.; Yang, J-M.; Tolbert, S. H.; Kaner, R. B. Synthesis of Ultra-Incompressible Superhard Rhenium Diboride at Ambient Pressure. *Science* **2007**, *316*, 436-439.

(5) Burdett, J. K.; Canadell, E.; Miller, G. J. Electronic Structure of Transition-Metal Borides with the A1B_2 Structure. *J. Am. Chem. Soc*. **1986**, *108*, 6561-6568.

(6) Kayhan, M.; Hildebrandt, E.; Frotscher, M.; Senyshyn, A.; Hofmann, K.; Alff, L.; Albert, B. Neutron Diffraction and Observation of Superconductivity for Tungsten Borides, WB and W_2B_4, *Solid State Sciences* **2012**, *14*, 1656-1659.

(7) Cheng, X.; Zhang, W.; Chen, X-Q.; Niu, H.; Liu, P.; Du, K.; Liu, G.; Li, D.; Cheng, H-M.; Ye, H.; Li, Y. Interstitial-boron Solution Strengthened WB_{3+x}, *Appl. Phys. Lett*. **2013**, *103*, 171903.

(8) Cheng, X-T.; Xing-Qiu Chen, X-Q.; Li, D-Z.; Li, Y-Y. Computational Materials Discovery: the Case of the W–B System, *Acta Cryst*. **2014**, *C70*, 85–103.

(9) Lech A. T.; Turner, C. L.; Mohammadi, R.; Tolbert, S.H.; Kaner, R. B. Structure of Superhard Tungsten Tetraboride: a Missing Link between MB_2 and MB_{12} Higher Borides, *Proc. Natl. Acad. Sci. U S A*. **2015**, *112*, 3223-3228.

(10) Kopp, J. P.; Barnes, R. G. Nuclear Magnetic Resonance of ^{11}B and ^{27}Al in Aluminum Diboride, *J. Chem. Phys*. **1971**, *51*, 1840 – 1841.

(11) Eastman, M. Examples of Hartmann-Hahn Match Conditions for CP/MAS between Two Half-Integer Quadrupolar Nuclei, *J. Magn. Reson*. **1999**, *139*, 98 - 108.

(12) Baek, S. H.; Suh, B. J.; Pavarini, E.; Borsa, F.; Barnes, R. G.; Bud'ko, S. L.; Canfield, P. C. NMR Spectroscopy of the Normal and Superconducting States of MgB_2 and Comparison to AlB_2, *Phys. Rev. B* **2002**, *66*, 104510.

(13) Papavassiliou, G.; Pissas, M., Karayanni, M.; Fardis, M., Koutandos, S., Prassides, K. ^{11}B and ^{27}Al NMR Spin-lattice Relaxation and Knight Shift of $Mg_{1-x}Al_xB_2$: Evidence for an Anisotropic Fermi Surface, *Phys. Rev. B* **2002**, *66*, 140514(R).

(14) Pavarini, E.; Baek, S. H.; Suh, B. J.; Borsa, F.; Bud'ko, S. L.; Canfield, P. C. NMR Relaxation Rates and Knight Shifts in MgB_2 and AlB_2: Theory Versus Experiments, *Supercond. Sci. Technol.* **2003**, *16*, 147 -151.

(15) Burkhardt, U.; Gurin, V.; Haarmann, F.; Borrmann, H.; Schnelle, W.; Yaresko, A.; Grin, Y. On the Electronic and Structural Properties of Aluminum Diboride $Al_{0.9}B_2$, *J. Solid State Chem.* **2004**, *117*, 389 - 394.

(16) Choi, Y. J.; Lu, J.; Sohn, H. Y.; Fang, Z. Z.; Kim, C.; Bowman, Jr., R. C.; Hwang, S-J. Reaction Mechanisms in the $Li_3AlH_6/LiBH_4$ and $Al/LiBH_4$ Systems for Reversible Hydrogen Storage. Part 2: Solid-State NMR Studies, *J. Phys. Chem. C* **2011**, *115*, 6048 - 6056.

(17) Sevastyanova, L. G.; Gulish, O. K.; Stupnikov V. A.; Genchel, V. K.; Kravchenko, O. V.; Bulychev, B. M.; Lunin, R. A.; Tarasov, V. P. Structure and Properties of Solid Solutions in the Mg-Al-B System, *Cent. Eur. J. Phys*. **2012**, *10*, 189 - 196.

(18) Lue, C. S.; Tao, Y. F.; Su, T. H. Comparative NMR Investigation of the Re-based Borides, *Phys. Rev. B* **2008**, *78*, 033107.

(19) Żogał, O. J.; Fojud, Z.; Herzig, P.; Pietraszko, A.; Lyashchenko, A. B.; Jurga, S.; Paderno, V. N. Crystal Structure, Electric Field Gradient, and Electronic Charge Densities in ReB_2: A Single Crystal X-ray, ^{11}B Nuclear Magnetic Resonance, and First-principles Study, *J. Appl. Phys*. **2009**, *106*, 033514.

(20) Koumoulis, D., Turner, C. L; Taylor, R. E.; Kaner, R. B. ^{11}B NMR Spectral and Nuclear Spin−Lattice Relaxation Analyses of ReB_2, *J. Phys. Chem. C* **2016**, *10*, 2901−2907.

(21) Jaeger, C., Hemmann, F. EASY: A Simple Tool for Simultaneously Removing Background, Deadtime and Acoustic Ringing in Quantitative NMR Spectroscopy—Part I: Basic Principle and Applications , *Solid State NMR*, **2014**, *57-58*, 22-28.

(22) Fenzke, D.; Freude, D.; Frohlich, T.; Haase, J. NMR Intensity Measurements of Half-integer Quadrupole Nuclei, *Chem. Phys. Lett*. **1984**, *111*, 171 - 175.

(23) Mann, P.; Klinowski, J.; Trokiner, A.; Zanni, H.; Papon, P. Selective and Non-selective NMR Excitation of Quadrupolar Nuclei in the Solid State, *Chem. Phys. Lett*. **1988**, *151*, 143 - 160.

(24) Farrar, T. C.; Becker, E. D. *Pulse and Fourier Transform NMR, Introduction to Theory and Methods*; Academic Press: New York, 1971.

(25) Yesinowski, J. P. Finding the True Spin−Lattice RelaxationTime for Half-Integral Nuclei with Nonzero Quadrupole Couplings, *J. Magn. Reson*. **2015**, *252*, 135 −144.

(26) Harris, R. K.; Becker, E. D.; de Menezes, S. M. C.; Goodfellow, R.; Granger, P. NMR Nomenclature, Nuclear Spin Properties, and Conventions for Chemical Shifts (IUPAC Recommendations 2001), *Pure Appl. Chem*. **2001**, *73*, 1795 - 1818.

(27) Bishop, M.; Shahid, N.; Yang, J.; Barron, A. R. Determination of the Mode and Efficacy of the Cross-Linking of Guar by Borate Using MAS ^{11}B NMR of Borate Cross-Linked Guar in Combination with Solution ^{11}B NMR of Model Systems, *Dalton Trans*. **2004**, *17*, 2621 - 2624.

(28) Jung, J. K.; Baek, S. H.; Borsa, F.; Bud'ko, S. L.; Lapertot, G.; Canfield, P. C. ^{11}B NMR and Relaxation in the MgB_2 Superconductor, *Phys. Rev. B* **2001**, *64*, 012514.

(29) Haas, H. Electric Field Gradients in Metal Diborides, *Hyperfine Interactions* **2001**, *136/137*, 731 – 735.

(30) Massiot, D.; Farnan, I.; Gautier, N.; Trumeau, D.; Trokiner, A.; Coutures, J.P. ^{71}Ga and ^{69}Ga Nuclear Magnetic Resonance Study of β-Ga_2O_3: Resolution of Four- and Six-fold Coordinated Ga Sites in Static Conditions, *Solid State NMR* **1995**, *4*, 241–248.

(31) Andrew, E. R.; Tunstall, D. P. Spin-Lattice Relaxation in Imperfect Cubic Crystals and in Non-cubic Crystals, *Proc. Phys. Soc*. **1961**, *78*, 1-11.

(32) Klesnar, H.; Aselage, T. L.; Morosin, B.; Hwei, G. H.; Lawson, A. C. The Diboride Compounds of Molybdenum: MoB_{2-x} and Mo_2B_{5-y}, *J. Alloys Cmpds*. **1996**, *241*, 180 – 186.

(33) Kiessling, R. The Crystal Structures of Molybdenum and Tungsten Borides, *Acta Chem. Scand.* **1947**, *1*, 893 -916.

(34) Frotscher, M.; Klein, W.; Bauer, J.; Fang, C-M.; Halet, J-F.; Senyshyn, A.; Baehtz, C.; Albert, B. M_2B_5 or M_2B_4? A Reinvestigation of the Mo/B and W/B System, *Z. Anorg. Allg. Chem*. **2007**, *633*, 2626 – 2630.

(35) Higashi, I.; Takahashi, Y. Crystal Structure of MoB_2, *J. Less-Common Met*. **1986**, *123*, 277 – 283.

(36) Okada, S.; Atoda, T.; Higashi, I.; Takahashi, Y. Preparation of Single Crystals of MoB2 by the Aluminum-Flux Technique and Some of Their Properties, *J. Mater. Sci.* **1987**, 22, 2993 – 2999.

(37) Waugh, J. S.; Fessenden, R. W. Nuclear Resonance Spectra of Hydrocarbons: The Free Electron Model, *J. Am. Chem. Soc*. **1957**, *79*, 846 - 849.

(38) Momma, K.; Izumi, F. VESTA: a three-dimensional visualization system for electronic and structural analysis. *J. of Appl. Cryst.* **2008**, *41*(3), 653 - 658.

(39) Korringa, J. Nuclear Magnetic Relaxation and Resonance Line Shift in Metals, *Physica* **1950**, *XVI*, 601 - 610.

(40) Taylor, R. E.; Chim,. N.; Dybowski, C. NMR Characterization of Partially Deuterated γ-Glycine, *J. Mol. Struct*. **2006**, *794*, 133 – 137.

(41) Koumoulis, D.; Taylor, R. E. Revisiting $NH_4H_2PO_4$: ^1H MAS, CRAMPS, and Spin−Lattice Relaxation, *J. Phys. Chem. C* **2015**, *119*, 13836 − 13840.

Chapter 5

Introduction

For the past few years, transition metal diborides have attracted a great deal of attention amongst materials researchers due to their combination of outstanding physical properties such as metallic electrical conductivity, high incompressibility, high shear strength, and exceptionally high hardness.[1] All of these attributes are desirable in materials for structural and engineering compounds, and indicate that diborides may be suitable replacements for current metal carbides in next-generation cutting tools.[2] Generally, these properties are also correlated; a high bulk modulus (incompressibility) appears to be a necessary[3], if not sufficient[4], predictor of high hardness.[5] It has been the design philosophy pursued to take advantage of this correlation by attempting to force highly incompressible metals to also become resistant to shear through the introduction of covalent bonds.[6,7] Boron is a small, highly bonded[8] element that is capable of forming bonds to metals[9], thus creating transition metal borides.

As such, we have previously shown that rhenium diboride (ReB_2) is one of the hardest metallic compounds known, with a Vickers hardness under a low applied load (0.49 N) reaching as high as 40.5 GPa.[10] This value is above the arbitrary threshold[3] of 40 GPa commonly accepted for superhard compounds, and gives ReB_2 the distinction of being one of the first superhard metals identified.[11] We have since furthered the scope of our attention to even higher borides, such as WB_4, which we have shown to have the potential to become even significantly harder, achieving a Vickers hardness of up to 57.3 GPa under a 0.49 N load when appropriate solid solutions with metals such as Ta, Mn, and Cr are formed.[12] However, it was in the course of our work with

tungsten tetraboride that we first noticed a peculiarity in the interaction of rhenium and tungsten in the presence of excess boron.[13] While the addition of rhenium was found to increase the hardness of WB_4, this effect was due most apparently to a fine dispersion of ReB_2 found in the arc-melted ingots. Intriguingly, the lattice parameters of the ReB_2 in the composite sample was found to be somewhat larger than that of pure ReB_2, implying the formation of a ReB_2/WB_2 solid solution.

While WB_2 does not take the ReB_2 structure under any known conditions, the native structure of WB_2 (often referred to as the W_2B_4 structure) equally incorporates elements found in two parent types: those of AlB_2 (*P6/mmm*) and ReB_2 (*P6$_3$/mmc*) (Figure 5.1). Given the hybrid nature of the WB_2 structure, it seems intuitive that tungsten might show some ability to form mixed-metal ternaries and solid solutions with materials that take *either* the ReB_2 *or* the AlB_2 structure-types. In agreement with this idea, solid solutions of tungsten with metal borides taking the AlB_2 structure type (e.g. TiB_2) have been reported.[14] Furthermore, it is known that some tungsten-containing ternaries, such as $W_{0.5}Ru_{0.5}B_2$ and $W_{0.5}Os_{0.5}B_2$ may take the ReB_2 structure-type, as first identified by Rogl *et al.*[15–17] and recently revisited by Zelringer and Rogl *et al.*[18]. Unfortunately, little is historically reported about the solid solubility of tungsten in ReB_2 itself, save for a lone mention by Kuz'ma *et al.* in a Soviet-era phase-diagram[19].

Additionally, since our original identification of superhardness in ReB_2, an increasingly large number of theoretical works have appeared in the literature with calculations of hardness using first-principles methods for metal borides of this type.[20–36] Several of these works have made claims to predict the already measured and reported properties of previously synthesized materials, but there are few examples of true predictions followed by experimental validation. Therefore, it is as yet unclear to what extent the experimentalist might find these sorts of calculations to be a

useful guidance for the creation of new compounds with reliably pre-determined properties, and to what extent these works represent *post-hoc* rationalization of properties that have already been determined. A few of these works, however, have made predictions for the properties of solid solutions that are hypothetically synthesizable using ordinary techniques, but the properties for which have not yet been reported. Included among these are several works making predictions for ReB_2-structured WB_2 and for rhenium/tungsten diboride solid solutions.[20,23,31,32,36–38] As a result, experimental realization of such a system, would be an ideal test of these theoretical predictions.

For the reasons mentioned above, solid solutions employing WB_2 as either the host or guest component are worthy systems of study for hard-materials research. From a crystallochemical perspective, a hybrid structure of WB_2 and ReB_2 should lead to relatively straight-forward transformations to other structure types with presumably tunable lattice parameters and properties. From the perspective of the experimentalist, wary of the reliability of guidance taken from theory, it makes an interesting test for the accuracy that can be expected from predictions of this kind.

Here, we thus report the successful synthesis of solid solutions of rhenium diboride and tungsten diboride that take on the superhard ReB_2 structure-type. Additionally, we report the hardness of these solid solutions, and the structural evolution occurring in the ReB_2 lattice as a result of the dissolution of tungsten. Thus far, to our knowledge, the work presented here would appear to be the only detailed experimental study of properties of solid solutions of tungsten and rhenium diborides. We have found that, while tungsten causes a monotonic increase in the lattice parameters of ReB_2, all of the solid solutions maintain super-hardness under low loads, and the hardness of ReB_2 is significantly increased by ~ 17% for small additions of tungsten metal.

Moreover, the bulk modulus of a nearly equimolar W/Re solid solution is basically identical to that of pure ReB_2. This work further allows comparisons of these properties (e.g., hardness) to selected theoretical predictions from the literature to be made, from which we conclude that first-principles hardness models may indeed provide qualitative guidance for the experimentalist in the search for hard metallic phases.

Materials and Methods

Powders of tungsten (99.95%, Strem Chemicals, USA), rhenium (99.99%, CERAC Inc., U.S.A), and amorphous boron (99+%, Strem Chemicals, U.S.A) for X-ray diffraction or crystalline ^{11}B (99.9%, 98.5% ^{11}B enriched, Ceradyne, USA) for neutron diffraction were uniformly mixed in the ratio M : B = 1 : 2.25 using an agate mortar and pestle. For the solid solutions, tungsten was substituted for rhenium at concentrations in the range of 0.5 – 48.0 at.% such that the total M : B ratio was maintained. The slight excess of boron is required to counter-act its evaporation during the process of arc-melting, and to prevent the formation of lower borides of tungsten. Each mixture was consolidated into a 12 mm, ~ 500 mg pellet by means of a hydraulic press (Model 3851, Carver, USA) under a pressure of ~562 MPa. The pellets were then placed in an arc-melting furnace consisting of a water-cooled copper hearth/anode and a non-consumable tungsten cathode. Subsequently, the atmosphere of the furnace was purged several times with ultra-high-purity argon. After removing trace gases in the system by melting several small chips of a titanium/zirconium alloy, an ~100 ampere DC current was applied to the samples, melting them. The fused ingots were then flipped and subjected to the electric arc two additional times in order to ensure homogeneity. Once cooled, the ingots were bisected using a sinter-bonded diamond lapidary sectioning saw (South Bay Technology Inc., USA). One-half of each ingot was crushed

to a powder (-325 mesh) using a Plattner-style, hardened tool-steel mortar (model H-17270, Humboldt Mfg. Co., USA). The powdered samples were washed 3 times with 1.0 M HCl to remove impurities introduced from the steel grinding equipment.

Powder samples for X-ray diffraction (XRD) were placed in a flat-stage holder and the surface was flattened by removing for consistency across scans. All X-ray data were collected on an X'Pert Pro™ Bragg-Bentano geometry powder diffraction system (PANalytical, Netherlands), employing nickel filtered $Cu_{K\alpha}$ radiation ($\lambda_{K\alpha1}$ = 1.540593 Å, $\lambda_{K\alpha2}$ = 1.5444274 Å)[39], 0.04 radian Soller slits, and X'Celerator position sensitive detector. The collected data were subjected to least-squares refinement using the EXPGUI[40] front-end to the GSAS[41] Rietveld refinement software package, from which the lattice parameters were extracted. Samples annealed at 1300 K for 24 hours prior to grinding were found to give results identical to un-annealed (as-synthesized) samples.

To verify the results from X-ray diffraction and to assess any changes in the atomic coordinates of boron in the ReB_2 structure, samples of ReB_2 and $Re_{0.52}W_{0.48}B_2$ enriched in ^{11}B were subjected to neutron time-of-flight (TOF) powder diffraction at the HIPPO Beamline at LANSCE (Los Alamos Neutron Science Center, Los Alamos National Lab, Los Alamos New Mexico). For these experiments, the samples were annealed at 1300 K for 24 hours prior to their coarse grinding (-220 mesh) and subsequent washing with 1.0 M HCl. The powders were placed in sealed vanadium "cans" and subjected to water-moderated thermal neutrons collimated to 1 cm diameter for a total time of 1 h each, whilst their diffraction patterns were collected by an array of ^3He scintillation-counter panels arranged at 144° and 90° about the sample. The neutron diffraction

data were refined from the high-resolution 144° back-scattering panel using the EXPGUI[40] and GSAS[41] Rietveld refinement software packages.

Hardness data were obtained via micro- and nano-indentation of the un-ground half of each ingot. Prior to hardness testing, the samples were first cold-mounted in epoxy (Allied High Tech Products Inc.) and polished to an optically flat surface using a tripodal polisher (South Bay Technology Inc., USA) with SiC polishing papers (120 – 1,200 grit, Allied High Tech Products Inc., USA) followed by diamond films (30 – 0.5 μm, South Bay Technology Inc., USA).

Micro-indentation was performed by the Vickers method using a MicroMet® 2103 micro-hardness tester (Buehler GmBH, Germany) with a pyramid diamond tip. Indentations were made under five loads ranging from 0.49 N to 4.9 N with a dwell time of 15 s. To ensure accuracy, at least 9 randomly chosen spots separated by over 100 micrometers were chosen for indentation at each load. The results reported here represent the averages of these points. The lengths of the diagonals of the indents were then measured with a high-resolution Zeiss Axiotech® 100HD optical microscope (Carl Zeiss Vision GmbH, Germany) and (Eq. 5.1) was used to obtain Vickers micro-indentation hardness values (H_v):

$$H_v = \frac{1854.4P}{d^2} \qquad \text{(Eq. 5.1)}$$

where P is the applied load (in N) and d is the arithmetic mean of the diagonals of the indent (in micrometers).

Nano-indentation was performed using an MTS Nano Indenter XP (MTS, USA) with a Berkovich diamond tip. After calibration of the indenter with a standard silica block, the samples

were indented automatically to a depth of 950 nm at 20 "randomly" pre-determined points, and the resulting load versus displacement plots were averaged. The nano-indentation hardness of the material may be found based on the shape of the loading and un-loading curves by the method of Oliver and Pharr[42] using (Eq. 5.2):

$$H = \frac{P_{max}}{A} \qquad \text{(Eq. 5.2)}$$

where H, P_{max}, and A are nano-indentation hardness, peak indentation load, and projected area of the hardness impression, respectively.[42]

Superhard materials tend to possess high bulk modulus in addition to high hardness. The incompressibility of $Re_{0.52}W_{0.48}B_2$ was measured using synchrotron based radial X-ray diffraction in a diamond anvil cell (DAC).[43] The high pressure experiments were performed in an angle-dispersive geometry at the beamline 12.2.2 of the Advanced Light Source (ALS, Lawrence Berkeley National Lab). Polycrystalline $Re_{0.52}W_{0.48}B_2$ sample was ground to powder with a grain size of <20 μm and then loaded into a ~60-μm- diameter sample chamber in a boron gasket. This gasket (~400 μm in diameter and ~70 μm in thickness) was embedded in a small rectangular Kapton sheet. A piece of ~25-μm-diameter Pt foil was placed on top of the sample to serve as a pressure internal standard. No pressure-transmitting medium was used in order to create a non-hydrostatic environment in the DAC. A monochromatic X-ray beam with a wavelength of 0.4959 Å, and size of 20×20 μm was passed through the sample perpendicular to the loading axis. The 2D diffraction image was collected with program FIT2D[44] at a step of ~4 GPa after calibration of the detector distance and orientation using a LaB_6 standard.

Thermal stability of the powder samples (-325 mesh) was studied in air (non-medical) using a Pyris Diamond thermogravimetric/differential thermal analyzer module (TG-DTA, Perkin Elmer Instruments, USA). Samples were heated up to 200°C at a rate of 20°C/min and soaked at this temperature for 10 min to remove water vapor. They were then heated up to a 1,000°C at a rate of 2°C⁄min and held at this temperature for 120 min. The samples were then air cooled at a rate of 5°C⁄min. X-ray diffraction was carried out on the powders after cooling to determine the resulting phases.

In order to verify the elemental composition, beyond XRD analysis, an $Re_{0.52}W_{0.48}B_4$ sample was analyzed on an FEI Nova 230 high resolution scanning electron microscope (FEI Co., USA), utilizing an UltraDry EDS detector (Thermo-Scientific Inc., USA), four points were randomly selected for elemental spectra, and elemental composition maps were produced, as seen in Figure(s) 5.2 and 5.3. The elemental compositions matched, within error, to the stoichiometry of the sample, and there was no evidence of elemental impurities within the sample (potentially introduced through the synthesis process), seen in Table 5.1. To assess the phase stability of the solid solutions, several samples were thermally annealed over a period of 24 h at a temperature of 1300 K under flowing high-purity argon in a Lindberg/Blue M Mini Mite™ laboratory tube furnace (Thermo-Scientific Inc., USA). The samples were crushed and analyzed by X-ray diffraction using the above procedure. The lattice parameters differed trivially from samples subjected only to arc melting, though the FWHM for the peaks was somewhat reduced, indicating the elimination of some lattice strain.

Results and Discussion

As one might predict on the basis of the WB_2 structure, consisting of one-half ReB_2-type HCP-type layers and one-half AlB_2-type simple hexagonal layers, the maximum solubility of tungsten in ReB_2 is nearly 50%. A sample powder X-ray diffraction pattern for the highest concentration used in this study (48 at.% W) is given in Figure 5.4. The lattice parameters, unit cell volume, and *c*/*a* axial ratios for a selection of solid solutions synthesized for this study are listed in Table 5.2. Both the *a*- and *c*-axes are expanded by incorporation of tungsten into the ReB_2 structure and monotonically increased in absolute value as a function of tungsten concentration. The near- perfect linear trends observed (Figure 5.5 and Figure 5.6) would be predicted by strict adherence to Vegard's law if a hypothetical ReB_2-type tungsten diboride existed. By extrapolating the curves in Figure 5.6, the lattice parameters for such a hypothetical ReB_2-type WB_2 compound may be estimated as a = 2.9159 Å and c = 7.7486 Å. These values can be compared to a = 2.9002 Å and c = 7.4759 Å for pure ReB_2, resulting in a total volume increase of approximately 4.64% in the hypothetical W analogue.

Micro-hardness data are presented in Figure 5.7. Small additions of tungsten in the range of 0.5 – 2 at.% have a relatively large and immediate impact on the hardness of ReB_2, which increases from 40.5 ± 2.8 GPa (1% W addition) to 47.8 ± 3.5 GPa (0.5% W addition) at low (0.49 N) load and from 29.3 ± 0.8 GPa (1% W addition) to 33.9 ± 0.7 GPa (0.5% W addition) at high (4.9 N) load. The addition of larger amounts of tungsten produces less dramatic changes, though all of the solid solutions are at least slightly harder than pure ReB_2. Calculated hardness values for all of the compositions tested are given in tabular form with their corresponding estimated standard errors in Table 5.3.

The nano-indentation data (Figure 5.8) largely corroborate the Vickers micro-hardness data. As the curves heavily overlap for the samples of various concentrations (again emphasizing their similarity in hardness), the inset shows an expanded view of the region of low load where, again, small concentrations of tungsten are found to have a disproportionately large impact on the hardness of ReB_2 even though all concentrations are at least as hard as pure ReB_2. A maximum hardness of 48.12 GPa was found for 0.5% W in ReB_2 at a displacement of 55.4 nm (load of 2.63 mN) compared to 43.99 GPa at 64.0 nm (3.16 mN load) for pure ReB_2. Likewise, all of the tungsten-containing solid solutions synthesized maintained hardness values greater than 40 GPa until well over 200 nm of penetration depth. Table 5.4 summarizes the hardness values obtained at various penetration depths as well as the average hardness found over the range from 60 nm to 900 nm for the various compositions tested; furthermore. All of the compositions tested were superhard.

To examine any crystallographic effects dissolving tungsten in the ReB_2 structure, time-of-flight (TOF) neutron powder diffraction data were obtained for the highest composition obtained (48 at.% W) as well as for pure ReB_2. The background-subtracted, Rietveld-refined powder diffraction patterns are depicted in Figure 5.9 and the relevant crystallographic data can be found in Table 5.5 and Table 5.6. The neutron diffraction data for ReB_2 are in excellent agreement with those observed by Frotscher *et al.* (cf. a = 2.90059 Å c = 7.47745 Å -*versus* our a = 2.900468 Å and c = 7.47734 Å).[45] There is no evidence for preferential site orientation or secondary phases. The fit to the solid solution sample is nearly as good as that for pure ReB_2 ($\chi 2$ = 1.731 versus 2.023), and potentially could be improved toward parity if the thermal parameters were separately refinable for the Re and W atoms without correlation. The discrepancy in lattice parameters between the neutron diffraction and X-ray diffraction samples is most likely due to a

slight difference in zero-point calibration between the two machines. The overall trend in parameters is, however, maintained, as can be seen from the *c*/*a* axial ratios shown in Table 5.2 where the difference between the ratios calculated by the two techniques is less than the error that would be introduced by a discrepancy of 0.25 at. % in tungsten composition (calculated from the trend in Figure 5.5**)**.

The volume of the unit cell as a function of pressure was measured in the DAC under non-hydrostatic conditions. Data was measured at $\varphi = 54.7°$, where φ is the angle between the diffracting plane normal and the maximum stress axis. It is believed that the volume measured at $\varphi = 54.7°$ reflects the compression behavior due to the hydrostatic component of stress.[46,47,48] The compression data was then fit to the second order Birch-Murnaghan equation of state (Equation 5.3) as a function of the normalized pressure (F_v, equation 5.4) and Eularian strain (f_v, equation 5.5) [49,50], as seen below:

$$P = 1.5\, K_0\, [(V/V_0)^{-7/3} - (V/V_0)^{-5/3}] \qquad \text{(Eq. 5.3)}$$

$$f_v = \frac{1}{2}\left(\left(\frac{v_0}{v}\right)^{\frac{2}{3}} - 1\right) \qquad \text{(Eq. 5.4)}$$

$$F_v = \frac{P}{3f_v\,(1+2f_v)^{2.5}} \qquad \text{(Eq. 5.5)}$$

Here the pressure (*P*) is provided by the pressure standard within the test cell, and the change in volume (V_0 at ambient pressure and *V* under pressure) were determined experimentally. Together these allow for the calculation of the normalized pressure (F_v) and the Eulerian strain (f_v). As seen in Figure 5.10, the solid line yields a bulk modulus of 365 ± 4 GPa at ambient pressure with the pressure derivative fixed at 4. This value is higher than WB_2 (K_0=349 GPa)[51] and within error of pure ReB_2 (K_0=367 GPa),[52] emphasizing the key role of the ReB_2 structure type in determining the mechanical properties of these solid-solution based materials. Note that deviations

from linearity at low pressures are common and are likely due to incomplete compression of the sample and thus deviation in the pressure experienced by the sample and the pressure calibrant. The volume compression as a function of pressure is collected, advantageously, through radial diffraction; the X-ray beam runs parallel to the culet of the diamond. In this instance, hydrostatic conditions are not required because the diffraction peaks collected, contain both the high stress and low stress directions. Therefore, hydrostatic conditions are not necessarily assumed, and the hydrostatic changes are calculated directly from the non-hydrostatic data at the magic angle (54.7°). Truly hydrostatic and non-hydrostatic/magic angle data give results that have strong agreement, and as such, either may be used to calculate the bulk modulus of a new material.

Thermogravimetric analysis data are presented in Figure 5.11. These data show little difference in thermal stability of the solid solutions versus data previously published for ReB_2, where oxidation of samples began at approximately the same temperature (~500°C).[10] The qualitative difference between the tungsten-containing samples and pure ReB_2 is an initial rise in mass before the steep drop, which may be ascribed to the formation of WO_3 or a mixed oxide of W/ReO_3 before the temperature is sufficiently hot for the sublimation of Re_2O_7. X-ray diffraction of the end product (a yellow, glassy, microcrystalline mass) corroborates this hypothesis by confirming the presence of WO_3. From the isothermal data at 1000°C (lower inset of Figure 5.11), it may be inferred that the formation of the boron oxidation product (B_2O_3 glass) offers relatively little protection against high-temperature oxidation, as the samples continue to decompose nearly linearly at this temperature.

Whereas the boron network in AlB_2-type borides are formed by filling the interstices of a primitive hexagonal arrangement of metal atoms, ReB_2-type borides are based on an expanded

hexagonal-close-packed metal lattice. From Figure 5.1, it is clear that one consequence of this atomic arrangement is a greater molar volumetric increase upon the addition of B to the pure metal to form ReB_2-type borides than to form AlB_2-structured compounds. For example, from Ti to TiB_2, the lattice parameters increase from a = 2.951 Å and c = 4.684 Å[53] to a = 3.024 Å and c = 3.154 Å[54], whereas for Re to ReB_2, the parameter increase is from a = 2.76 Å and c = 4.458 Å[55] to a = 2.90 Å and c = 7.747 Å. In the case of titanium, these values correspond to a 2.47 % increase in the metal-metal contact distance in *a* and an 8.90 % increase in contact distance in *c*. By contrast, in the case of rhenium, 5.07 % and 49.5 % increases are observed along *a* and *c*, respectively. Therefore, one may conclude that borides of the AlB_2 type can be thought of as relatively true interstitial compounds that obey the Hume-Rothery[56] rules for their formation, whereas borides of the ReB_2 type represent a distinctly layered structure with the insertion of puckered boron nets behaving as though an additional layer of metal had been added. Alternatively, in accordance with the qualitative interpretation offered by Pauling[57], the *small* increase in metal-metal distance for the AlB_2 structure type indicates a *large* degree of metal-metal bonding (at the expense of metal-boron bonding), whereas the much larger increases in compounds of the ReB_2 structure type indicate that metal-metal bonding is virtually eliminated in the *c*-direction and replaced with metal-boron covalent bonds.

This interpretation is further corroborated by the fact that the boron-boron bond distances increase from 1.75 Å in TiB_2 (an example of an AlB_2-structured compound) to 1.83 Å in ReB_2, indicating a decrease in B-B bond order going from planar boron 'sheets' to 'puckered' boron nets, and therefore a concomitant increase in bond order from boron to metal (assuming valance is maintained).[58] Electronic calculations on ReB_2 have shown exactly this effect, with significant electron density localized between boron and rhenium, which has also been used to explain the

extremely high hardness of this compound.[23,36,59] The extreme change in packing density between the two boride types is not detrimental to the hardness of the larger-volume ReB_2-type compounds, but rather a consequence of the covalency that gives rise to the high hardness. Thus the fact that the lattice parameters for $ReWB_2$ solid solutions increase with increasing tungsten is not necessarily be an indication of lowered hardness as long as metal-boron covalency is maintained or increases, and this is strongly suggested by our results.

One may hypothesize, therefore, that other compounds with the ReB_2 structure type might also be superhard. This does indeed appear to be the case as, for example, Du *et al.* have studied the mechanical properties of $W_{0.5}Os_{0.5}B_2$ (a = 2.913 Å c = 7.566 Å), a ternary taking the ReB_2-structure, and measured a low load (0.49 N) hardness of 40.4 ± 1.3 GPa, and a calculated bulk modulus of 354 GPa. Additionally, recent work by Tao *et al*. has examined the MoB_2 system, where there are two structure types available depending on synthetic conditions. Here the structure with more puckering in the boron sheets is found to be harder than the lower-volume AlB_2-type structure. The reported high load (9.8 N) hardness values for AlB_2-type MoB_2 and "Mo_2B_4"-type MoB_2 are 15.2 GPa and 22.0 GPa, respectively, which is a relatively drastic difference of 44.7%.[60] Given that the reported hardness of "W_2B_4"-type WB_2 is 26.1 GPa (0.98 N)[61], an additional 44.7% increase of hardness would result in a compound having a hardness of approximately 37.8 GPa, which is nearly superhard.

Indeed, ReB_2-structured WB_2 has previously been proposed as a candidate hard or superhard compound.[23,31] Chen *et al.* have predicted from *ab initio* calculations that ReB_2-structured WB_2 should be stable *versus* the AlB_2-structured form under ambient conditions.[36] The calculated shear modulus reported for this structural form is 273 to 294 GPa based on GGA and

LDA approximations, respectively (cf. 271.6 to 302 GPa for ReB_2, as determined experimentally [62,63]). Assuming that the correlation between shear modulus and indentation hardness holds,[64] this may be interpreted as a prediction that the hardness of ReB_2-structured WB_2 should have comparable hardness to native ReB_2. This hypothesis was later partially supported by Zhong *et al.*, who used the Voigt-Reuss-Hill (VRH) approximation to calculate shear moduli of 253 GPa and 291 GPa and employed a semi-empirical method to estimated hardness values of 35.7 GPa and 39.1 GPa, for ReB_2-structured WB_2 and native ReB_2, respectively.[31]

Unfortunately, WB_2 takes the "W_2B_4"-type structure under ambient conditions, and a material with the ReB_2-structure polymorph has never been isolated at that stoichiometry. However, some speculation has been offered from theoretical calculations about the properties of W/ReB_2 solid solutions and these compounds were anticipated to also be superhard.[20,32,37] The estimated values for the hardness of $W_{0.5}Re_{0.5}B_2$ is 40.1 GPa and the bulk modulus is 354 GPa according to Du *et al.;*[37] and similar hardness of 40.9 GPa was calculated by Ivanovskii.[65] Our results are in excellent agreement with these claims, as the experimentally determined values for the hardness of $Re_{0.52}W_{0.48}B_2$ are 41.7 ± 0.7 GPa (0.98 N) from micro-indentation and 39.96 GPa (average) from nano-indentation. The measured bulk modulus of 365 ± 4 GPa for the $Re_{0.52}W_{0.48}B_2$ composition is slightly higher than the calculated value of 354 GPa, but in the right range. While there are some discrepancies in the lattice parameters between the predicted values of a = 2.88 Å c = 7.57 Å according to Du[37] and a = 2.8702 Å c = 7.5224 Å according to Tu *et al.* and our experimentally determined values of a = 2.9076 Å and c = 7.6076 Å for ~50 at. % W, the excellent qualitative agreement between the sets of results would seem to indicate that computational methods have quite some value in the prediction of properties of hard materials.

Tu *et al.* further predicted peaks in the hardness of tungsten/rhenium diboride solid solutions at both 10 at. % W and 60 at. % tungsten, predictions that agree well with our experimental results, especially if 60 % is taken to correspond to our data at 48 at. %. The slight variations in hardness that we observe in the range from 10 at. % – 50 at. % W can likely be ascribed to subtle electronic effects. However, none of the previously described theoretical works predict the relatively large increase in hardness that we observe for small amounts of additional tungsten in the range of 0.5 to 2 at. %. The likely cause of this discrepancy is that the theoretical calculations take for granted the perfect stoichiometric ratio, atomic regularity, and homogeneity that may only exist in an ideal compound. All real samples should be expected to have some slight deviations from perfect stoichiometry, many of which will manifest as slight strains on the lattice. A strained crystalline lattice should be expected to contribute to the hardness of the compound. The addition of very small amounts of tungsten may enter the crystalline structure of ReB_2 in such a way as to compensate for these strains and may therefore exert a disproportionately large effect on the measured hardness of the compound. One would not expect to be able to calculate this sort of extrinsic factor given the assumptions made in the theoretical calculations.

Recent interest in the metal-boride field has grown, in part due to the desire for further understanding of the inherent properties of the materials, but also because of the potential applications of these materials. Theoretical calculations are beginning to meet experimental results more frequently and with the increasing accuracy of these computational predictions, they are becoming useful partners and guides for synthesis studies. We note, however, that from atomic-level interactions to mesoscale and continuum properties, many intricacies remain for these borides. Despite this excellent agreement with first principles predictions, the metal-boride family of materials still has many open questions to be answered.[66,67,68]

As far as we are aware, the only other experimental work on these solid solutions was executed as part of a phase-diagrammatic study by Kuz'ma *et al.*, who reported a maximum solubility limit of $Re_{0.81}W_{0.19}B_2$ with lattice parameters a = 2.910 Å and c = 7.590 Å.[19] On the basis of the axial ratio (2.6082), these values correspond well to values along our curve for a boride of formula $Re_{0.65}$ $W_{0.35}B_2$. The discrepancy in the atomic fraction is likely due to poor optimization of the compositions for the samples in the Kuz'ma study, given that most samples prepared in that work were multi-phase ingots, making it much more difficult to estimate the atomic ratios in each phase of the sample. A plausible contribution to the difference between our estimates for maximum tungsten solubility, is a slight boron deficiency in the compounds synthesized in previous works. In the course of optimizing our own synthetic procedure, we have found that a slight excess of boron is necessary to ensure the complete formation of the ReB_2 structured compound. It is important to note that ratios of boron to metal of less than approximately 2.2 : 1 (B : M) during synthesis appear to encourage the formation of the "W_2B_4" phase.

Conclusions

In this work, we have successfully synthesized solid solutions of tungsten in rhenium diboride using an electric-arc furnace. The solubility limit for tungsten in ReB_2 is nearly 50 at. % (maximum composition reported here is 48%), indicating a very high degree of solubility. The lattice parameters for the solid solutions vary linearly along both the *a* and *c* axes with increasing tungsten content. The solid solutions are statistically random up to and including the limiting composition, according to both X-ray and neutron diffraction. All of the compositions tested within the range from 0 – 48 at.% W are superhard according to analyses of both micro-indentation and nano-indentation data and the bulk modulus of 48% W solid solution is nearly identical to the pure ReB_2 material. These results further indicate that ReB_2 structured compounds are superhard.

Table 5.1 Energy-dispersive X-ray Spectroscopy of $Re_{0.52}W_{0.48}B_2$*

	B-K	***W-M***	***Re-M***
ReWB2_pt1	61.27 ±1.02	19.82 ±0.22	18.91 ±0.23
ReWB2_pt2	61.58 ±1.04	17.44 ±0.24	20.97 ±0.33
ReWB2_pt3	60.80 ±1.05	20.70 ±0.85	18.50 ±1.03
ReWB2_pt4	62.18 ±1.09	19.68 ±0.82	18.14 ±1.00

*Energy-dispersive X-ray Spectroscopy of randomly selected points of an $Re_{0.52}W_{0.48}B_2$ sample, in At. %. The locations selected correspond to Fig. 5.2, while Figure 5.3 provides a representative spectra. The consistent ratio of metals (W:Re) are nearly 1:1, within the detection limit of the instrument.

Table 5.2: Lattice Parameters, Cell Volumes, and Axial Ratios for the W/ReB_2 Solid Solutions[a]

Composition	*a* Parameter (Å)	*c* Parameter (Å)	Volume (Å^3)	*c/a* Ratio
ReB_2 (X-Ray)	2.90016(1)	7.47591(8)	54.455	2.5778
ReB_2 (Neutron)	2.900468(24)	7.47734(10)	54.477	2.5780
$Re_{0.995}W_{0.005}B_2$	2.9006(7)	7.4799(2)	54.504	2.5787
$Re_{0.95}W_{0.05}B_2$	2.9014(5)	7.4917(2)	54.618	2.5821
$Re_{0.90}W_{0.10}B_2$	2.9019(3)	7.5056(5)	54.738	2.5864
$Re_{0.80}W_{0.2}B_2$	2.9033(8)	7.5315(6)	54.981	2.5941
$Re_{0.70}W_{0.30}B_2$	2.9046(7)	7.5573(2)	55.220	2.6018
$Re_{0.60}W_{0.40}B_2$	2.9065(7)	7.5884(1)	55.519	2.6108
$Re_{0.52}W_{0.48}B_2$ (X-ray)	2.9076(9)	7.6076(8)	55.701	2.6164
$Re_{0.52}W_{0.48}B_2$ (Neutron)	2.909085(21)	7.61009(10)	55.774	2.6160

[a] Numbers in parentheses represents the uncertainty of the preceding least-significant digit

Table 5.3: Summary of Vickers Micro-Hardness Data

	Vickers Hardness (GPa)				
Composition	**0.49 N**	**0.98 N**	**1.96 N**	**2.94 N**	**4.90 N**
ReB_2	40.45 ± 2.79	35.08 ± 2.21	31.73 ± 1.49	30.30 ± 0.74	29.31 ± 0.77
0.5% W	44.89 ± 1.94	41.19 ± 1.56	38.24 ± 1.21	36.85 ± 1.13	33.85 ± 0.69
1% W	47.47 ± 3.49	42.75 ± 2.39	37.86 ± 2.50	33.81 ± 1.07	32.40 ± 0.92
2% W	42.31 ± 2.38	39.35 ± 1.32	37.91 ± 1.31	34.10 ± 0.77	31.74 ± 0.57
3% W	46.96 ± 1.77	40.00 ± 1.17	36.75 ± 1.28	34.41 ± 0.83	31.97 ± 0.82
4% W	46.86 ± 1.71	41.65 ± 2.01	37.75 ± 1.28	34.82 ± 1.02	30.24 ± 0.66
5% W	41.83 ± 1.06	37.51 ± 1.03	34.11 ± 0.56	32.45 ± 0.38	29.79 ± 0.20
10% W	48.18 ± 1.01	40.69 ± 0.47	37.87 ± 0.25	32.66 ± 0.59	30.58 ± 0.34
20% W	44.69 ± 0.89	37.15 ± 0.37	33.62 ± 0.32	31.72 ± 0.54	29.81 ± 0.09
30% W	43.79 ± 1.58	40.98 ± 0.60	34.99 ± 0.35	34.92 ± 0.48	30.12 ± 0.31
40% W	48.17 ± 0.53	38.03 ± 0.53	34.76 ± 0.71	32.52 ± 0.28	30.31 ± 0.59
48% W	47.20 ± 1.06	41.74 ± 0.70	34.49 ± 0.21	32.10 ± 1.11	30.92 ± 0.92

Table 5.4: Nano-Indentation Hardness at Selected Penetration Depths and the Average over the Range from 60 nm to 900 nm

	Nano-Indentation Hardness (GPa)			
Composition	**at 60 nm**	**at 250 nm**	**at 900 nm**	**Avg(60-900)**
ReB_2	43.39	39.43	34.48	39.44
0.5% W	47.81	40.66	34.25	41.14
1% W	45.88	39.76	34.16	40.00
10% W	44.97	40.17	34.64	40.23
30% W	43.97	39.86	34.11	39.94
48% W	43.37	40.42	34.29	39.96

Table 5.5: Crystallographic Data for ReB_2 from TOF-Neutron Diffraction

ReB_2	
Crystal System	Hexagonal
Space Group	*$P6_3/mmc$*
Lattice Parameters	
$a = b$ (Å)	2.900468(24)
c (Å)	7.47734(10)
V (Å^3)	54.4771(10)
Calculated Density (g/cm^3)	
R_{wp-b}	1.91%
χ^2	1.731

ReB_2	Mult.	Symm.	x	y	z	Frac.	$U_{11=22}$	U_{33}	U_{12}
Re	2	-6m2	1/3	2/3	1/4	1.00	0.00249(3)	0.00309(7)	0.00124(2)
B	4	3m	1/3	2/3	0.54805(5)	1.00	0.00559(5)	0.00630(8)	0.00100(2)

Table 5.6 Crystallographic Data for $Re_{0.52}W_{0.48}B_2$ from TOF-Neutron Diffraction

$Re_{0.52}W_{0.48}B_2$	
Crystal System	Hexagonal
Space Group	*$P6_3/mmc$*
Lattice Parameters	
$a = b$ (Å)	2.909085(21)
c (Å)	7.61009(10)
V (Å^3)	55.7742(9)
Calculated Density (g/cm^3)	
R_{wp-b}	2.41%
χ^2	2.023

$Re_{0.52}W_{0.48}B_2$	Mult.	Symm.	x	y	z	Frac.	$U_{11=22}$	U_{33}	U_{12}
Re	2	-6m2	1/3	2/3	1/4	0.52	0.00088(4)	0.00084(7)	0.00044(2)
B	4	3m	1/3	2/3	0.54403(4)	1.00	0.00439(3)	0.00356(6)	0.00219(2)
W	2	-6m2	1/3	2/3	1/4	0.48	0.00088(4)	0.00084(7)	0.00044(2)

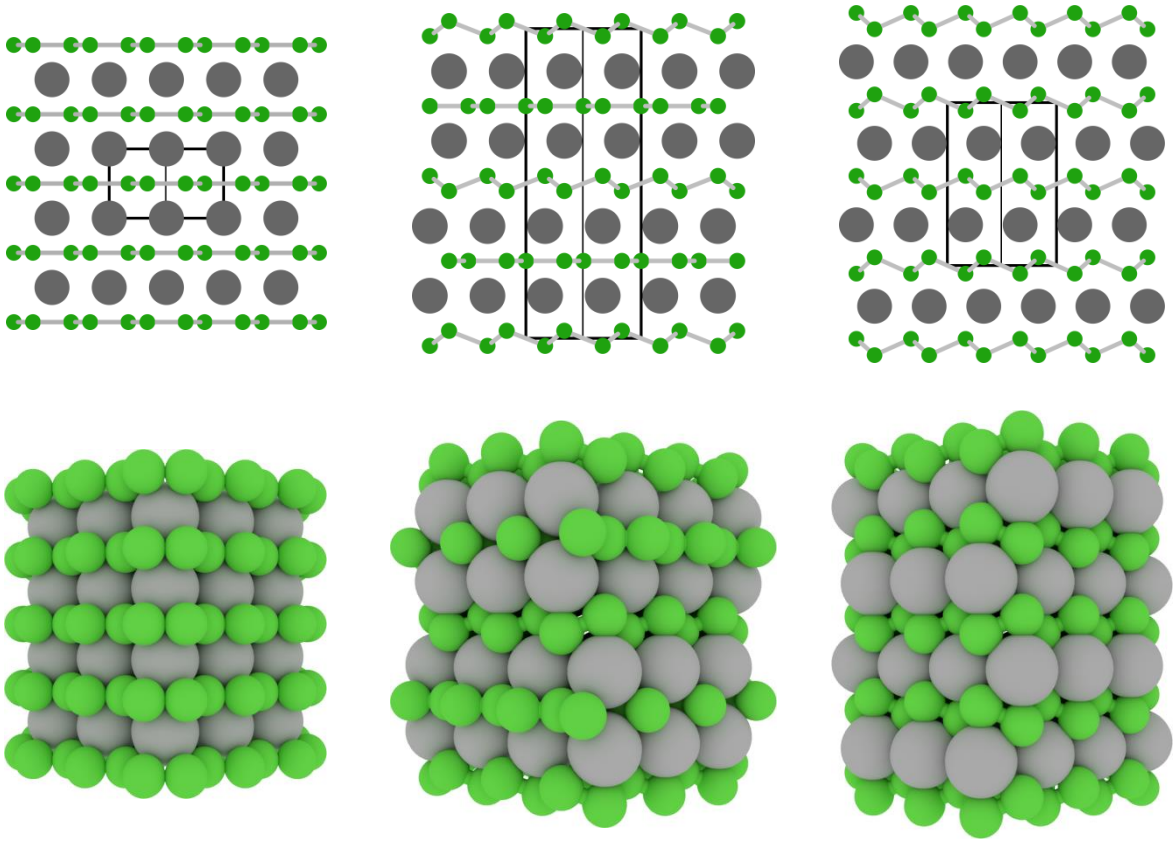

(a) **(b)** **(c)**

AlB_2-type WB_2 **"W_2B_4"-type WB_2** **ReB_2**

Figure 5.1: A comparison of the structures of several diborides structure types. **Top:** A schematic representation of the borides, normal to the [111] crystallographic plane, emphasizing the stacking sequence of the metal atoms. The unit cell for each structure is bounded by the black box. **Bottom:** space filling atomic models of the above structures shown along the same viewing direction, emphasizing the interstitial nature of the boron atomic filling. All structures are drawn to scale.

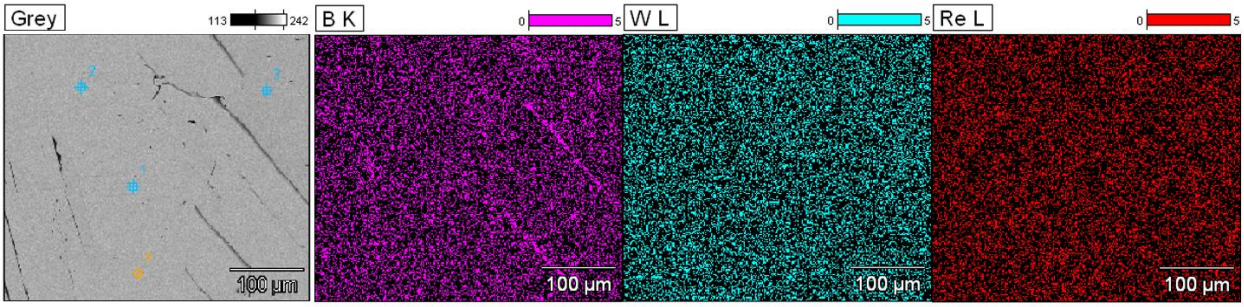

Figure 5.2: Elemental map for an $Re_{0.52}W_{0.48}B_2$ sample, indicating the composition and location of boron (K line), tungsten (L line), and rhenium (L line), respectively. The four randomly selected areas for composition analysis (from Table 5.6) are shown in the gray image. The average grain size is less than 100 µm, and the distribution of tungsten and rhenium is found to be uniform throughout the grains.

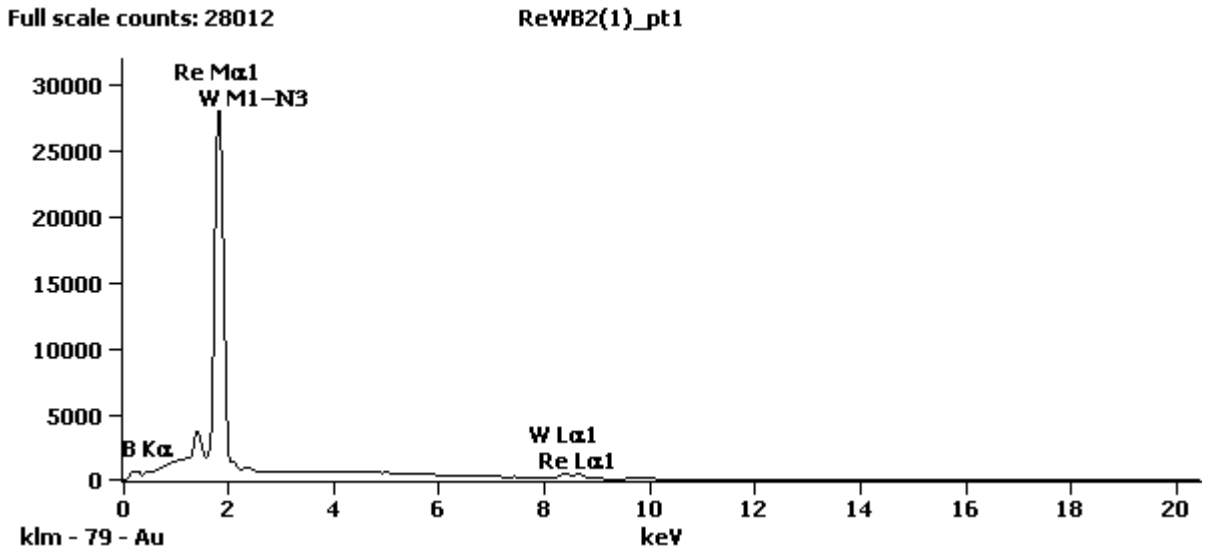

Figure 5.3: EDS Spectra for an $Re_{0.52}W_{0.48}B_2$ sample. Spot 1 (gray image in Figure 5.2) spectra was chosen, but all spectra are nearly identical when overlaid—Table 5.6 shows the difference in composition between the four randomly selected spots.

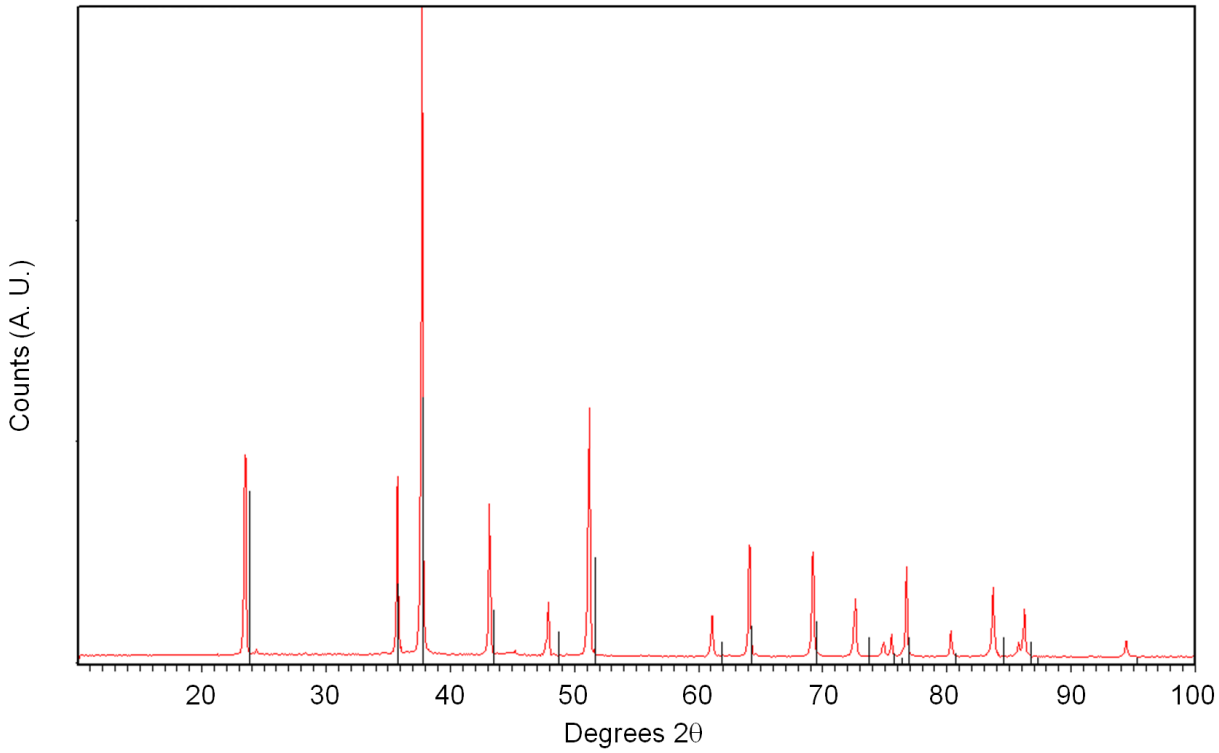

Figure 5.4: Sample X-ray diffraction pattern of a specimen containing 48 at.% tungsten in ReB_2 showing the full pattern shifting of peaks. Peaks having greater {00*l*} character are shifted to a more noticeable extent due to the greater sensitivity of the c-axis to the solubility of tungsten. The black stick pattern represents where the diffraction peaks appear for pure ReB_2.

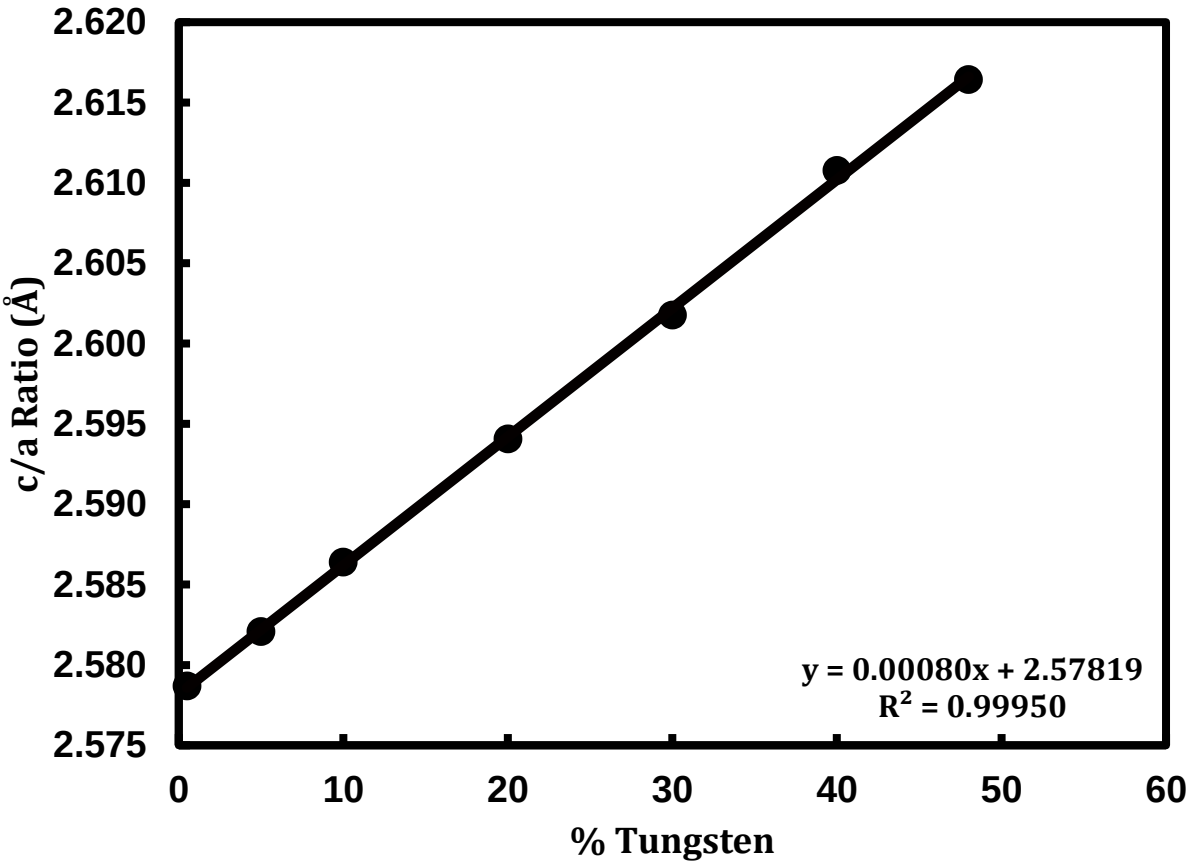

Figure 5.5: A plot of the calculated axial ratio for the ReB_2 structured solid solutions versus tungsten content in atomic percentage. As both values increase monotonically, the axial ratio increases monotonically as well. The linear best-fit equation is given in the lower right corner.

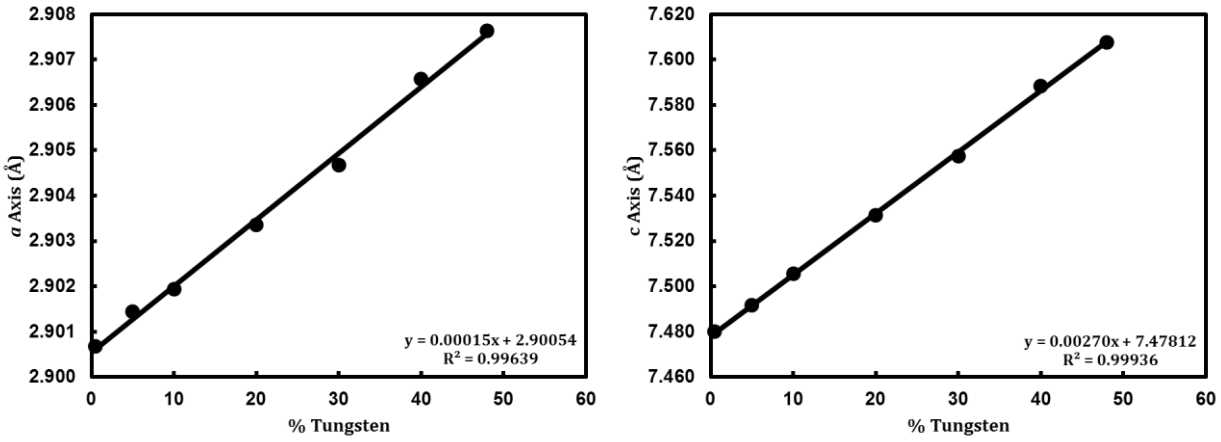

(a) **(b)**

Figure 5.6: Plots of **(a)** the measured *a*-axis and **(b)** the measured *c*-axis for the ReB_2 structured solid solutions *versus* tungsten content in atomic percentage. For both axes, the increase is virtually monotonic, but the rate of change in the *a*-axis parameter is significantly less than seen for the *c*-axis. Linear best-fit equations are shown in the lower right corners. The unconstrained intercepts agree well with the measured lattice parameters for pure ReB_2.

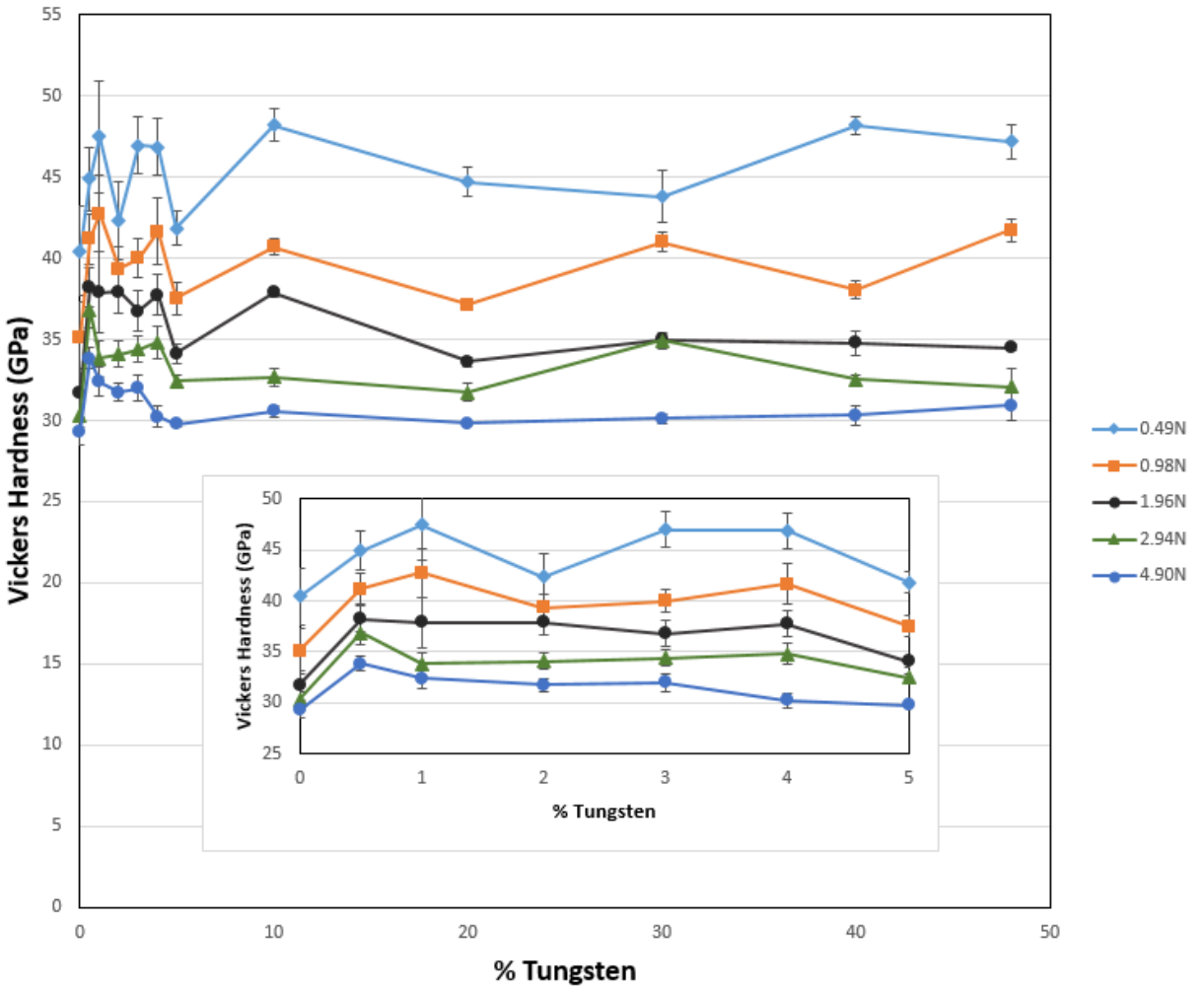

Figure 5.7: Vickers micro-indentation hardness versus metal-basis atomic composition of tungsten for various ReB_2-based solid solutions. Each indentation load is represented from a separate line in the plot. The hardness is dramatically increased with small additions of tungsten atoms, the effect rapidly diminishing as higher solid-solubility is reached, with the plot becoming nearly flat for all loads for every concentration of tungsten from 10 at.% to 48 at.%. **Inset:** A cropped view of the hardness enhancement from 0 – 5 at.% W addition.

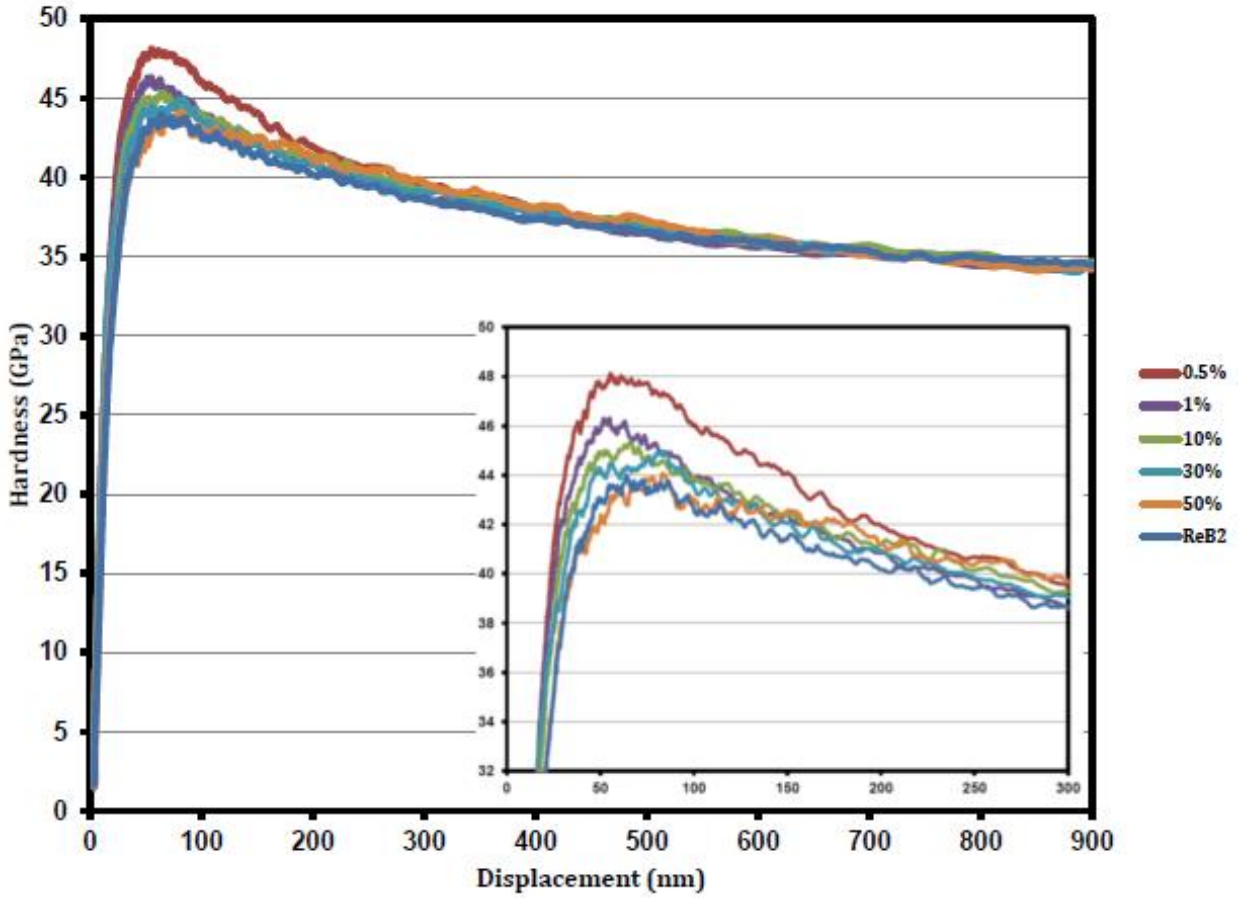

Figure 5.8: Nano-indentation hardness *versus* displacement curves for several concentrations of tungsten dissolved in rhenium diboride. **Inset:** cropped view of the first 300 nm of indentation into the sample surface. All of the solid solutions tested maintained hardness values greater than 40 GPa until at least nm of penetration depth, further indicating superhardness.

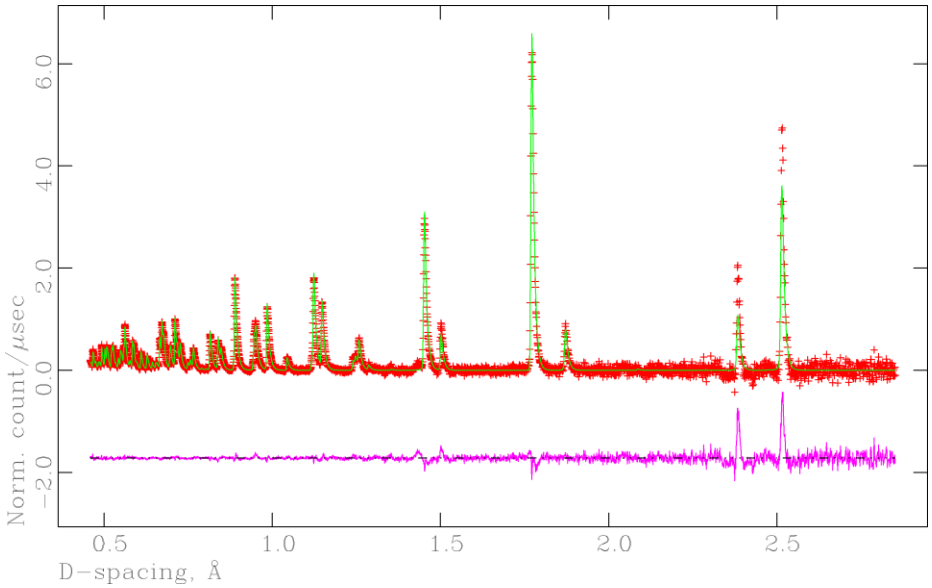

(a)

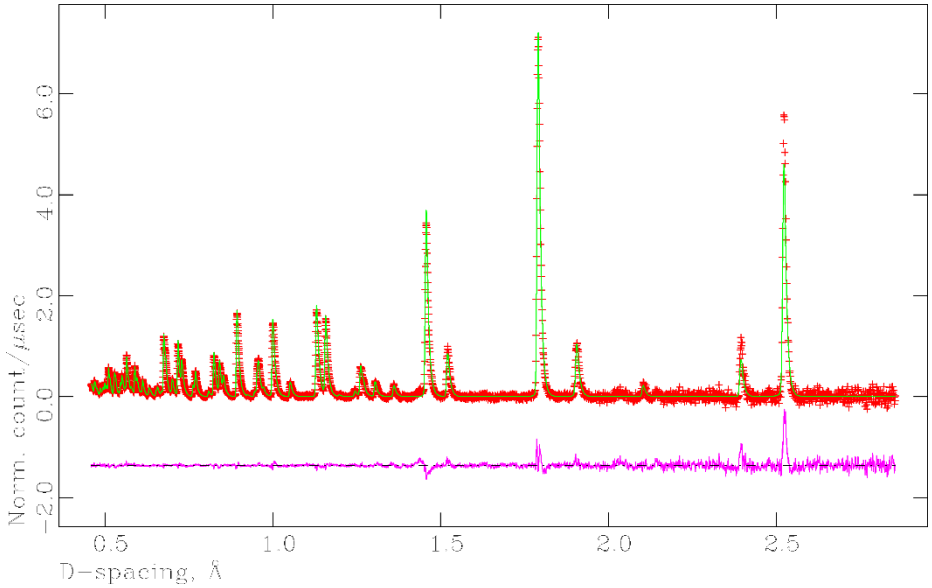

(b)

Figure 5.9: TOF-neutron powder diffraction refinement fit for **(a)** ReB_2 [Statistics: R_{wp} = 1.40%, R_{wp}(background subtracted) = 1.91%, R^2_{free} = 3.41%, χ^2 = 1.731] and **(b)** $Re_{0.52}W_{0.48}B_2$ [Statistics: R_{wp} = 1.77%, R_{wp}(background subtracted) = 2.41%, R^2_{free} = 2.44%, χ^2 = 2.023]. Red (+): observed Green (–): calculated Magenta (–): difference. The background is subtracted for clarity.

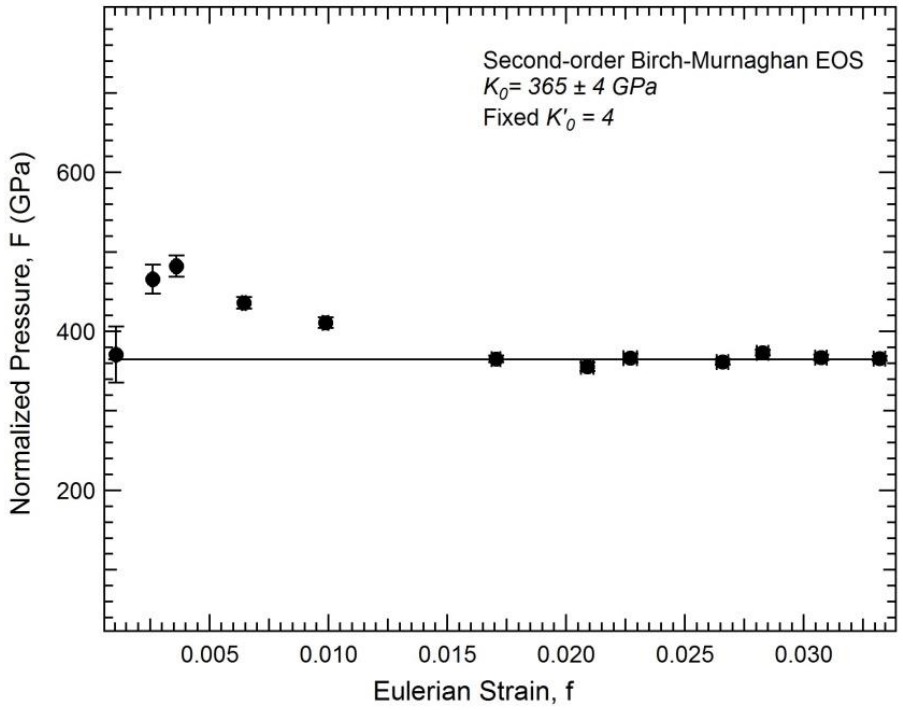

Figure 5.10: Compression data for $Re_{0.52}W_{0.48}B_2$ compressed under non-hydrostatic conditions and collected at $\varphi = 54.7°$ to simulate hydrostatic conditions. The data are plotted in terms of normalized pressure and Eulerian strain. The straight line is a second-order fit to the Birch-Murnaghan equation of state; the variation from the trend line is commonly found at low pressures due to incomplete sample compaction.

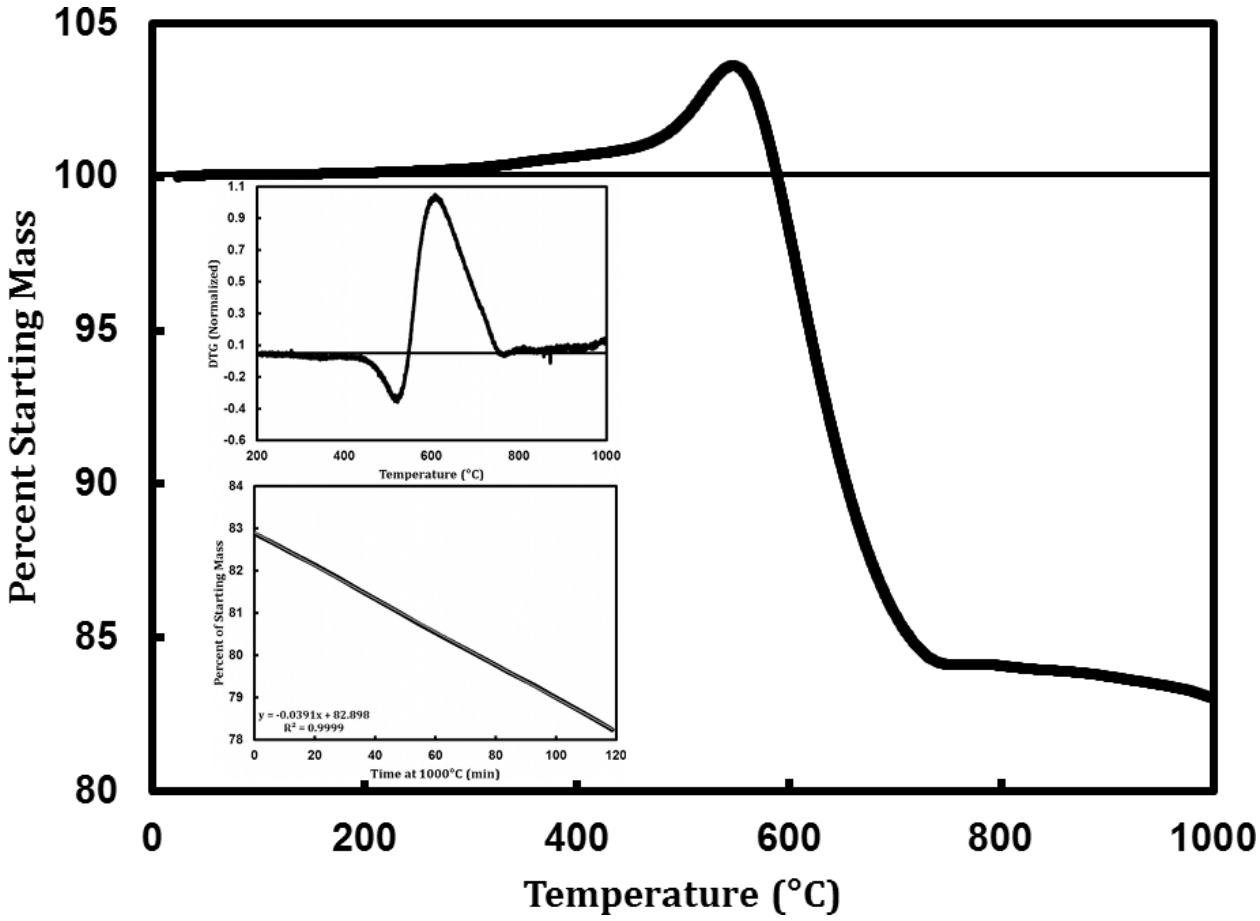

Figure 5.11: Percent mass *versus* temperature plot from the data obtained by thermogravimetric analysis (TGA) of a powdered (-325 mesh) sample containing 25 at.% tungsten under ambient air. The sample is stable to ≈520°C before first gaining mass (due to the formation of WO_3/B_2O_3) and then rapidly losing mass at ≈610°C (due to the volatilization of Re_2O_7). There does not appear to be any thermal stability enhancement from the addition of tungsten to ReB_2 (cf. Levine *et al.*[10]). **Upper Inset:** The normalized differential thermo-gravimetric (derivative) of the above data. **Lower Inset:** The rate of mass loss is nearly linear with time at 1000°C, showing that the sample rapidly reaches a steady-state of oxidation. It is likely that B_2O_3 acts as a flux for Re_2O_7, rather than as an oxygen barrier. The rate law equation is shown in the lower left corner.

References

(1) *Boron and Refractory Borides*; Matkovich, V. I., Ed.; Springer Berlin Heidelberg: Berlin, Heidelberg, **1977**.

(2) Mohammadi, R.; Kaner, R. B. Superhard Materials. In *Encyclopedia of Inorganic and Bioinorganic Chemistry*; Scott, R. A., Ed.; John Wiley & Sons, Ltd: Chichester, UK, 2011.

(3) Sung, C.-M.; Sung, M. *Mater. Chem. Phys.* **1996**, *43*, 1–18.

(4) Brazhkin, V. V.; Lyapin, A. G.; Hemley, R. J. *Philos. Mag. A* **2002**, *82*, 231–253.

(5) Weinberger, M. B.; Levine, J. B.; Chung, H.; Cumberland, R. W.; Rasool, H. I.; Yang, J.-M.; Kaner, R. B.; Tolbert, S. H. *Chem. Mater.* **2009**, *21*, 1915–1921.

(6) Gilman, J. J.; Cumberland, R. W.; Kaner, R. B. *Int. J. Refract. Met. Hard Mater.* **2006**, *24*, 1–5.

(7) Kaner, R. B.; Gilman, J. J.; Tolbert, S. H. *Science* **2005**, *308*, 1268–1269.

(8) Albert, B.; Hillebrecht, H. *Angew. Chemie Int. Ed.* **2009**, *48*, 8640–8668.

(9) Fehlner, T. P. *J. Solid State Chem.* **2000**, *154*, 110–113.

(10) Levine, J. B.; Nguyen, S. L.; Rasool, H. I.; Wright, J. A.; Brown, S. E.; Kaner, R. B. *J. Am. Chem. Soc.* **2008**, *130*, 16953–16958.

(11) Chung, H.-Y.; Weinberger, M. B.; Levine, J. B.; Cumberland, R. W.; Kavner, A.; Yang, J.-M.; Tolbert, S. H.; Kaner, R. B. *Science* **2007**, *316*, 436–439.

(12) Mohammadi, R.; Xie, M.; Lech, A. T.; Turner, C. L.; Kavner, A.; Tolbert, S. H.; Kaner, R. B. *J. Am. Chem. Soc.* **2012**, *134*, 20660–20668.

(13) Mohammadi, R.; Lech, A. T.; Xie, M.; Weaver, B. E.; Yeung, M. T.; Tolbert, S. H.; Kaner, R. B. *Proc. Natl. Acad. Sci. U. S. A.* **2011**, *108*, 10958–10962.

(14) Shibuya, M.; Kawata, M.; Ohyanagi, M.; Munir, Z. A. *J. Am. Ceram. Soc.* **2003**, *86*, 706–710.

(15) Rogl, P.; Nowotny, H.; Benesovsky, F. *Monatshefte für Chemie* **1970**, *101*, 27–31.

(16) Rogl, P.; Nowotny, H.; Benesovsky, F. *Monatshefte für Chemie* **1970**, *101*, 850–854.

(17) Rogl, P.; Rudy, E. *J. Solid State Chem.* **1978**, *24*, 175–181.

(18) Zeiringer, I.; Rogl, P.; Grytsiv, A.; Polt, J.; Bauer, E.; Giester, G. *J. Phase Equilibria Diffus.* **2014**, *35*, 384-395.

(19) Kuz'ma, Y. B.; Lakh, V. I.; Stadnyk, B. I.; Voroshilov, Y. V. *Sov. Powder Metall. Met. Ceram.* **1968**, *7*, 462–466.

(20) Lin, F.; Wu, K.; He, J.; Sa, R.; Li, Q.; Wei, Y. *Chem. Phys. Lett.* **2010**, *494*, 31–36.

(21) Wang, Y. X. *Appl. Phys. Lett.* **2007**, *91*, 101904.

(22) Šimůnek, A. *Phys. Rev. B* **2009**, *80*, 060103.

(23) Hao, X.; Xu, Y.; Wu, Z.; Zhou, D.; Liu, X.; Cao, X.; Meng, J. *Phys. Rev. B* **2006**, *74*, 224112.

(24) Aydin, S.; Simsek, M. *Phys. Rev. B* **2009**, *80*, 134107.

(25) Lazar, P.; Chen, X.-Q.; Podloucky, R. *Phys. Rev. B* **2009**, *80*, 12103.

(26) Zhong, M.-M.; Kuang, X.-Y.; Wang, Z.-H.; Shao, P.; Ding, L.-P.; Huang, X.-F. *J. Alloys Compd.* **2013**, *581*, 206–212.

(27) Liang, Y.; Li, A.; Zhao, J.; Zhang, W. *Mod. Phys. Lett. B* **2009**, *23*, 1281–1290.

(28) Zhou, W.; Wu, H.; Yildirim, T. *Phys. Rev. B* **2007**, *76*, 184113.

(29) Chen, W.; Jiang, J. Z. *Solid State Commun.* **2010**, *150*, 2093–2096.

(30) Soto, G.; Moreno-Armenta, M. G.; Reyes-Serrato, A. *Comput. Mater. Sci.* **2008**, *44*, 628–634.

(31) Zhong, M.-M.; Kuang, X.; Wang, Z.-H.; Shao, P.; Ding, L.-P.; Huang, X.-F. *J. Phys. Chem. C* **2013**, *2*, 10643–10652.

(32) Tu, Y.; Wang, Y. *Solid State Commun.* **2011**, *151*, 238–241.

(33) Tian, Y.; Xu, B.; Zhao, Z. *Int. J. Refract. Met. Hard Mater.* **2012**, *33*, 93–106.

(34) Gao, F. M.; Gao, L. H. *J. Superhard Mater.* **2010**, *32*, 148–166.

(35) Šimůnek, A. *Phys. Rev. B* **2007**, *75*, 172108.

(36) Chen, X.-Q.; Fu, C.; Krčmar, M.; Painter, G. *Phys. Rev. Lett.* **2008**, *100*, 196403.

(37) Du, X. P.; Wang, Y. X. *Phys. Status Solidi - Rapid Res. Lett.* **2009**, *3*, 106–108.

(38) Ivanovskii, A. L. *Prog. Mater. Sci.* **2012**, *57*, 184–228.

(39) Hölzer, G.; Fritsch, M.; Deutsch, M.; Härtwig, J.; Förster, E. *Phys. Rev. A* **1997**, *56*, 4554–4568.

(40) Toby, B. H. *J. Appl. Crystallogr.* **2001**, *34*, 210–213.

(41) Larson, A. C.; Von Dreele, R. B. *Los Alamos Natl. Lab. Rep.* **2000**.

(42) Oliver, W. C.; Pharr, G. M. *J. Mater. Res.* **2011**, *7*, 1564–1583.

(43) Hemley, R. J.; Mao, H. K.; Shen, G.; Badro, J.; Gillet, P.; Hanfland, M.; Häusermann, D. *Science.* **1997**, *276* (5316), 1242-1245.

(44) Hammersley, A. P.; Svensson, S. O.; Hanfland, M.; Fitch, A. N.; Hausermann, D. *Int. Journal of High Pressure Research*. **1996**, *14*, 235-248.

(45) Frotscher, M.; Hölzel, M.; Albert, B. *Zeitschrift für Anorg. und Allg. Chemie.* **2010**, *636*, 1783–1786.

(46) Singh, A. K.; Mao, H. K.; Shu, J.; Hemley, R. J. *Phys. Rev. Lett.* **1998**, *80*(10), 2157.

(47) Singh, A. K. *J. Appl. Phys.* **1993**, *73*, 4278-4286.

(48) Singh, A.K.; Balasingh C.; Mao, H.-K.; Hemley, R.J.; Shu, J. *J. Appl. Phys.* **1998**, *83*, 7567-7575.

(49) Birch, F. *J. Geophys. Res.* **1978**, *83*, 1257.

(50) Meade, C.; Jeanloz, R. *Geophys. Res. Lett.*, **1990**, *17*, 1157.

(51) Yin, S.; He, D.; Xu, C.; Wang, W.; Wang, H.; Li, L.; Zhang, L.; Liu, F.; Liu, P.; Wang, Z.; Meng, C. *High Pressure Research*, **2013**, *33*, 409.

(52) Suzuki, Y.; Levine, J.B.; Migliori, A.; Garrett, J.D.; Kaner, R.B.; Fanelli, V.R.;Betts, J.B. *J. Acoust. Soc. Am.* **2010**, *127*, 2797.

(53) Wood, R. M. *Proc. Phys. Soc.* **1962**, *80*, 783–786.

(54) Deligoz, E.; Colakoglu, K.; Ciftci, Y. O. *Solid State Commun.* **2009**, *149*, 1843–1848.

(55) Swanson, H. *Standard X-Ray Diffraction Powder Patterns. Howard E. Swanson, Ruth K. Fuyat and George M. Ugrinic.*; U.S. Government printing office: Washington, 1954.

(56) Hume-Rothery, W. *Philos. Mag. Ser. 7* **1953**, *44*, 1154–1160.

(57) Pauling, L. *J. Am. Chem. Soc.* **1947**, *69*, 542–553.

(58) Rundle, R. E. *Acta Crystallogr.* **1948**, *1*, 180–187.

(59) Wang, J.; Wang, Y.-J.. *J. Appl. Phys.* **2009**, *105*, 083539.

(60) Tao, Q.; Zhao, X.; Chen, Y.; Li, J. J.; Li, Q.; Ma, Y.; Cui, T.; Zhu, P.; Wang, X. *RSC Adv.* **2013**, *3*, 18317.

(61) Okada, S.; Kudou, K.; Lundström, T. *Jpn. J. Appl. Phys.* **1995**, *34*, 226–231.

(62) Suzuki, Y.; Levine, J. B.; Migliori, A.; Garrett, J. D.; Kaner, R. B.; Fanelli, V. R.; Betts, J. B. *J. Acoust. Soc. Am.* **2010**, *127*, 2797–2801.

(63) Chung, H.-Y.; Weinberger, M. B.; Yang, J.-M.; Tolbert, S. H.; Kaner, R. B. *Apl. Phys. Lett.* **2008**, *92*, 261904.

(64) Teter, D. M. *MRS Bull.* **1998**, *23*, 22–27.

(65) Ivanovskii, A. L. *J. Superhard Mater.* **2012**, *34*, 75–80.

(66) Chrzanowska, J.; Hoffman, J.; Denis, P.; Giżyński, M.; Mościcki, T. *Surface and Coatings Technology* **2015**, *277*, 15-22.

(67) Koumoulis, D.; Turner, C.L.; Taylor, R.E.; Kaner, R.B. *The J. of Phys. Chem. C.* **2016**, *120*, 2901-2907.

(68) Maździarz, M., & Mościcki, T. *J. of Alloys and Compounds*, **2016**, *657*, 878-888.

Chapter 6

Introduction

With the increasing demand for new super-hard materials for cutting tools, the introduction of transition metal borides as candidates for these applications has recently attracted a great deal of attention [1–4]. This trend is driven by a need for greater cutting efficiency compared to tungsten carbide (which is not super-hard) and by the shortcomings of diamond (which is unusable for cutting ferrous materials)[5] and cubic boron nitride (which is very expensive to synthesize and difficult to shape) [6]. Within this growing family of superhard materials, "tungsten tetraboride" (or "WB_4") is of specific interest due to its excellent mechanical properties and its relatively lower cost compared to borides like ReB_2, which contain platinum group metals [3, 7–11]. For instance, tungsten tetraboride demonstrates an extremely high indentation hardness of ~43 GPa by the Vickers method[8] under an applied load of 0.49 N and ~41.7 GPa by nano-indentation at a penetration depth of 95.25 nm, Figure 6.1, and can sustain a differential stress (a lower-bound estimate of compressive yield strength) of up to ~19.7 GPa.[12] Moreover, like ReB_2 [2], it is capable of scratching natural diamond [11]. Furthermore, we have shown that the hardness of this compound may be enhanced by the creation of solid solutions with other transition metals [12]. However, to understand the underlying mechanisms for the hardness enhancements observed in WB_4, and to guide the design of new super-hard borides with tailored mechanical properties, it is crucial to understand the crystal structure of this compound.

Due to the large and often contradictory discrepancies in the published models, this study was undertaken with the goal of revisiting the structure of the highest boride of tungsten using the

additional experimental resource of neutron diffraction in conjunction with X-ray diffraction. Neutron diffraction has a very high scattering cross-section for boron-11, so it is highly complementary to X-ray diffraction, which is heavily weighted towards the considerably more electron dense tungsten. By combining these two methods, we report what we believe is the first correct structure of the highest boride of tungsten. The structure contains some elements previously reported, along with several new ones. Most importantly, the structure provides real insight into the extremely high hardness and solid solution behavior of this relatively low-cost transition metal boride.

The structure of "WB_4" has been a contentious issue since it was first reported by Chretien and Helgorsky in 1961; it was originally assumed, based on its approximate chemical formula alone, to be related to borides of the ThB_4 type (tetragonal, a = 6.34 Å and c = 4.50 Å)[13]. Currently, four distinct experimentally determined, structural "solutions" have been proposed for this compound, the three most plausible of which are illustrated in Figure 6.2. As the history of these attempted solutions has already been explored in some detail in the recent work of Zeiringer *et al*. [14], they will be only briefly summarized here.

In 1965, Romans and Krug [15] produced what has become the most cited structure for "WB_4" in the literature. They refined their data against a lower volume (148.47 $Å^3$ vs. 180.88 $Å^3$), hexagonal unit cell (space group $P6_3/mmc$, a = 5.200 Å c = 6.340 Å) *versus* that originally proposed by Chretien and Helgorsky and made the first approximate atomic coordinates assignment (Figure 6.2a). After assigning the tungsten sites, which they assumed to be fully occupied, the only obvious remaining Wyckoff positions [*12(i)* and *4(f)*] were designated as boron

sites; the resulting B-B bonding structure being justified by relation to the "W_2B_5" structure (which was later demonstrated to be erroneous itself)[16]. A notable consequence of this was the imposition of B-B dimers, or "dumbbells", within the tungsten layers. Independently, Nowotny *et al*. explored the system in 1967 using tungsten borides isolated from eutectic melts of MB-WB_4-B (M = Ni, Rh, Pd, Pt), and assigned the formula $W_{2-x}B_9$ to the highest boride (approximate composition $W_{1.83}B_9$ or $WB_{4.92}$). Perhaps due to indexing contaminating X-ray lines (discussed below), they assigned it to the low-symmetry trigonal group *P-3* with a = 5.206 Å and c = 3.335 Å (Figure 6.2b) [17]. Their structure notably includes the presence of B_6 octahedra in the ordered tungsten vacancy positions and allows for fractional occupancy of one of the remaining tungsten sites.

To resolve the obvious discrepancies in the proposed structures, Lundström and Rosenberg attempted to definitely solve the positions of the boron atoms in 1973, using (then) modern, computerized least-squares refinement and Fourier difference map techniques[18]. To minimize the scattering power mismatch between metal and boron, they refined the presumably isomorphic molybdenum phase denoted "$Mo_{1-x}B_3$" ($x \approx 0.20$) (Figure 6.2c). While the partial occupancy of one of the metal position was re-affirmed in their work, the possibility of boron atoms filling vacancies in the structure was rejected, leaving a large void in the structure. This structure appears to be strongly supported by a recent single-crystal investigation by Zeiringer *et al.*, who refer to the tungsten phase as $W_{1-x}B_3$ (*$P6_3/mmc$*, a = 5.2012 Å c = 6.3315 Å)[14].

Further complicating the matter, a new series of computational-theoretical papers have recently appeared with the goal of identifying the structural origin of properties in WB_4[19–29]. Initially, these theoretical studies ranged from simple acceptance of the standard "WB_4" model of Romans and Krug [25], to a more cautionary tone, noting that "WB_4" as proposed by Romans and Krug is an unstable phase at ambient pressure [27]. Eventually it was realized that the structure,

properties, and stability of the highest boride of tungsten are better accounted for if the B_2 dimers proposed by Romans and Krug were simply removed, as *per* the Lundström and Rosenberg/Zeiringer structure [24, 28], and that this model could be further improved if some of the tungsten sites were treated as fractionally occupied [22]. Most recently, more exotic models have appeared that claim larger unit cells [19,30] and varying stacking orders [29] for the metal layers – hypotheses for which there is no experimental evidence. It should be noted that virtually all modern experimental structural determinations of WB_4 make clear that there is at least one partially occupied site, and computational methods still handle partial occupancy rather poorly – at least partially explaining some of these more exotic structures. Taken together, the calculations reported in these papers only further support the supposition that all previous structural models are incorrect, but do not appear to provide a viable alternative.

Materials and Methods

Samples for X-ray and neutron diffraction were prepared in parallel from the same batch of reagents and using the same methodology. High-purity powders of tungsten (99.95%, Strem Chemicals, USA) and crystalline ^{11}B (99.9%, 99.2% ^{11}B enriched, Ceradyne, USA) were manually mixed (without grinding) in the ratio 1 **:** 12 using an agate mortar and pestle and consolidated into pellets by means of a hydraulic jack press (Carver, USA) under a pressure of ~562 MPa. The pellets were placed on a water-cooled copper hearth, sealed inside a bell jar, and purged several times with ultra-high-purity argon followed by rough vacuum before being arc melted under one atmosphere of ultra-high-purity argon using ~100 ampere DC current and a non-consumable tungsten cathode. The samples were crushed to powders using a hardened steel mortar and pestle

(Humboldt) and wet-ground under methanol/ethylene glycol at low speed in a planetary mill (Pulverisette 5/2™, Fritsch, Germany) using stainless steel media until the majority passed through a 635 mesh (20 micron) screen (Humboldt, USA). The sieved powders were stirred for 2 hours under three successive aliquots of excess HCl to remove contaminating residue from the grinding and milling media. The sub-micron fraction of each sample was separated by repeated suspension in methanolic ammonia, the fastest settling fraction being retained. This procedure was found to minimize the contamination of foreign elements to below the detection limit of the energy dispersive X-ray spectroscopic analyzer (EDAX™, EDAX Inc., U.S.A) mounted to our SEM (JEOL JSM 6700 F, Japan).

Nano-indentation was also performed using an MTS Nano Indenter XP (MTS, USA) with a Berkovich diamond tip. After calibration of the indenter with a standard silica block, the samples were indented automatically over-night to a depth of 900 nm at 20 randomly pre-determined points and the resulting load versus displacement plots were averaged. The nano-indentation hardness of the material may be found based on the shape of the loading and un-loading curves by the method of Oliver and Pharr [41].

Samples for powder X-ray diffraction were deposited directly from methanolic suspension onto silicon (511) "zero-background" plates. Excess sample was removed by a razor blade until nearly perfectly flat. Diffraction patterns were collected from 10° to 156° 2θ using an X'Pert Pro™ Bragg-Bentano geometry laboratory X-ray diffractometer (PANalytical, Netherlands), employing nickel filtered $Cu_{K\alpha}$ radiation ($\lambda_{K\alpha1}$ = 1.540593 Å, $\lambda_{K\alpha2}$ = 1.5444274 Å) (42), rotating sample stage, 0.04 radian Soller slits, and X'Celerator position sensitive detector.

Neutron diffraction data were collected from the HIPPO (High-Pressure Preferred Orientation) beam line at LANSCE (Los Alamos Neutron Science Center, Los Alamos National Lab, Los Alamos New Mexico). This is a neutron time-of-flight machine using 5 banks of ^{3}H-detector tube panels. Due to the extremely high thermal neutron absorption cross-section of residual ^{10}B, even in our highly enriched samples (and of natural W itself) this beamline was selected due to its very high neutron flux, accommodation of large samples, and multiplicity of detector banks. Powdered samples on the order of 1 cm^3 in volume were loaded into vanadium foil "cans" and irradiated by water-moderated neutrons collimated to 1 cm diameter, while data were collected for a cumulative collection time of 6 hours. This unusually long collection time was necessary for the sake of higher signal to noise ratio. Powder X-ray and neutron diffraction data were subjected to simultaneous Rietveld refinement[43] using the EXPGUI[44] front-end to the GSAS[45] Rietveld refinement software package. Primarily the data from the 150° and 90° neutron collection banks were used due to their combination of high resolution and accuracy.

Single crystals of $WB_{4.2}$ containing natural boron where isolated from a crushed ingot obtained using the same arc-melting procedure described above. A suitable crystal was selected and mounted on a loop filament on an APEX-II™ CCD diffractometer (Bruker, Germany). Using the Olex2[46] structure solution program, the structure was solved by the 'charge flipping' method and refined using Gauss-Newton minimization with 16 parameters and without retraints. $WB_{4.2}$: hexagonal, space group *P6$_3$/mmc* (no. 194), *a* = 5.1998(15) Å, *c* = 6.3299(19) Å, *V* = 148.22(6) Å^3, μ(Mo$_{K\alpha}$) = 66.740 mm^{-1}, *T* = 293 K, *Dcalc* = 8.8402 g/cm^3, 1587 reflections

measured ($12.9° \leq 2\Theta \leq 59.14°$), 97 unique ($R_{int}$ = 0.0575, R_{sigma} = 0.0232) which were used in all calculations. The final R_1 was 0.0884 (I >= 2u(I)) and wR_2 was 0.1894 (all data).

Results and Discussion

The ambiguity in experimental determinations of the highest boride of tungsten stems primarily from the difficulties surrounding the Rietveld analysis of X-ray crystallographic data for a compound containing both very electron poor (boron, Z = 5) and very electron rich (tungsten, Z = 74) elements. Although the ratio of boron to tungsten is large, it is not so large that its core electron contribution to the diffraction pattern strongly influences the structure factor. This situation is exacerbated by three further issues: 1) the imprecision with which the compound's stoichiometry is known, 2) the synthetic necessity to include excess B, which takes on the β-boron structure, in order to produce WB_4 rather than WB_2 and 3) both the partial occupancy and vacancies of tungsten sites.

However, the very large contrast of the diffraction contribution of the two elements can be significantly decreased using neutron diffraction. Though the ratio of the X-ray diffraction cross-sections for tungsten and boron is large, the diffraction cross-section for thermal neutrons is roughly comparable. Thus, by simultaneous refinement of powder patterns obtained using both techniques, it becomes possible to distinguish between several possible structures. In some ways, our approach has similarities to the methods used previously by Lundström and Rosenberg, who used $Mo_{1-x}B_3$, which they assumed to be iso-structural with WB_4, as a model. The lower atomic number of molybdenum was used to enhance the overall contribution of boron to the X-ray diffraction structure factor for the molybdenum compound. Here we also strive to increase the

contribution of boron to the diffraction structure factor, but we do that by moving from X-rays to thermal neutrons. We believe the method described here is superior, since no assumptions need to be made about similarities between W and Mo borides, and the structure is determined for the native compound.

The primary complication of this procedure is the presence of a secondary phase. We have found that the approximate eutectic composition W:B = 1:12 most reliably produces the highest boride of tungsten without additional tungsten-containing phases. The excess boron crystallizes exclusively as the β-rhombohedral phase, without crystallographically identifiable dissolution of tungsten, and crystalline grains are found throughout arc melted ingots (Figure 6.6 and Figure 6.7). Conversely, the extreme chemical inertness and mechanical robustness of crystalline boron precludes post-synthetic separation, necessitating the simultaneous refinement of both phases. It should further be noted that boron is strongly adhered even to the macroscopic crystallites, reducing the possibility of obtaining high quality single-crystal data, and virtually eliminating the possibility of collecting high-quality neutron diffraction data, even if small crystals were readily obtainable.

While β-boron produces only trivial interference with the X-ray diffraction pattern, its presence poses a more formidable challenge for the analysis of the neutron diffraction data, where its many intense diffraction peaks heavily overlap those of the tungsten phase. Furthermore, the structure of β-boron is not known precisely, presumably due to a large amount of structural disorder at the interstices between icosahedra [31–37]. The neutron diffraction experiment produces an exceptionally complex pattern due to strong diffraction from the secondary β-rhombohedral

boron phase, which necessitates the simultaneous refinement of both phases. Nevertheless, the structure of the *β*-rhombohedral boron phase was found to be satisfactorily modeled by a slight modification of the atomic coordinates proposed by Hoard *et al.* [35]

The powder X-ray diffraction pattern of a crushed ingot of nominal composition WB_{12} made with isotopically enriched ^{11}B (i.e. $W^{11}B_{12}$), (Figure 6.4a) may be readily indexed against a hexagonal unit cell with dimensions a = 5.2001 Å and c = 6.3388 Å in the space groups *P62c*, *P63mc* or *P6$_3$ /mmc*. A few contaminating lines are noticeable and fully indexable against *β*-rhombohedral boron, as would be expected given the large molar excess of boron in the reaction mixture. Most of the contaminating lines, with the exceptions of those at 11.92° 2θ [$(10\text{-}2)_{boron}$], 16.19° 2θ [$(110)_{boron}$], 17.57° 2θ [$(104)_{boron}$], and 19.09° 2θ [$(20\text{-}1)_{boron}$] are of similar magnitude (<1%) and are on the same order as the diffraction lines from WB_x arising from residual $Cu_{K\beta}$ radiation. While we have found no evidence supporting the *P-3* trigonal structure proposed by Nowotny *et al.*[17], comparison of our X-ray diffractographs to reflections presented in their work leads us to conclude that they mis-assigned the highest intensity *β*-boron peak (observable in our data at 17.56° 2θ in Figure 6.4a) to the tungsten boride pattern. Using our data, we can readily replicate this reduction in symmetry of the unit cell, thus accounting for the discrepancy.

Here, we have chosen the highest symmetry group, *P6$_3$ /mm*, in which there are three crystallographic positions [Wyckoff *2(b)*, *2(c)*, and *2(d)*] that may be occupied by tungsten atoms. One of these positions [Wyckoff *2(d)*] is completely unoccupied, and thus one-third of the tungsten atoms are systematically absent, leaving 'voids' in the structure. Rietveld analysis against a base model consisting only of tungsten atoms and a hexagonal net of boron yielded a fractional

occupancy of approximately 2/3 for the tungsten atom at Wyckoff *2(c)*, centered on coordinates (0, 0, 1/4). The last remaining tungsten site, Wyckoff *2(d)*, at (1/3, 2/3, 1/4), is fully occupied.

Of the previous work on this subject, the structure derived by Zeiringer *et al*. from single crystal data (and related to that proposed by Lundström and Rosenberg) is the most similar to ours. However, repeated attempts at refining this 'boron-deficient' model where only voids are left for the partially occupied tungsten site, against the neutron powder diffraction data, made it immediately obvious that this model could not fully account for the observed peak intensities (Figure 6.4c). Fourier difference maps (Figure 6.5) subsequently revealed significant and unaccounted for diffraction density on Wyckoff *6(h)* at approximately (0.24, 0.12, 1/4) and (0.26, 0.13, 1/4). A boron atom inserted into either of these positions refined to (0.24, 0.12, 1/4) with an occupancy of approximately 1/3. The resulting model thoroughly accounts for the observed X-ray and neutron diffraction intensities (Figure 6.4c) and is compatible with our own single crystal measurements. Intriguingly, Lundström and Rosenberg mentioned peaks in their own Fourier maps corresponding to approximately 17% boron occupancy of the Wyckoff *6(h)*, which they subsequently dismissed. Had they further refined their structure with such sites occupied, they may very well have reached a similar result as we provide here (though with slightly different fractional occupancies).

Our final structure has a stoichiometry of approximately $WB_{4.2}$ and is presented in Figure 6.6 with the crystallographic parameters listed in Table 6.1. This analysis leads us to draw structural conclusions that have not been reported previously. Specifically, we find that a trigonal cluster of boron randomly fills the crystallographic position around the partially occupied tungsten

site. Due to the relative site-occupancies of these atoms (2/3 for W and 1/3 B), and the unrealistically short bond distance that would result if both types of atoms were to be present simultaneously, it is clear that this position is, in fact, not 'partially' occupied, but always filled *either* by tungsten *or* by the boron cluster. This arrangement places the atoms of the boron cluster exactly within bonding distance to the hexagonal boron nets and therefore gives rise to a subset of slightly distorted cuboctahedra distributed between tungsten planes. The average incidence of these cuboctahedra would therefore be approximately two for every three unit cells. The effective "void" space in this structure is thus very small, and the cuboctahedra have the potential to provide robust bonding between boron layers.

The structure expounded by Romans and Krug[15] may serve as an instructive, and perhaps cautionary, example of incomplete data being accepted in the scientific literature. It is explicitly stated in their work that their conjectural B_2 dimer units were placed, *ad hoc*, in order to fulfill their calculated stoichiometry (derived from microprobe analysis). At no point was this final structure subject to refinement or further analysis, nor could it have been, given the crudity of the diffraction pattern and the lack of modern computational tools. In fact, the presence of boron dimers as a crystallographic entity is exceptionally rare, with few such examples available in the scientific literature. The nearest example being the compound $IrB_{1.5,}$ wherein there is apparent dimerization of boron in what can be imagined as a Peierls-type distortion of the well-known boron chain structural motif. The existence of B_2 dimers would furthermore have contradicted the firmly established rule described by Kiessling[38], which states that as boron content increases, the structural motifs of boron atoms transition from isolated atoms, to chains, to nets, to polyhedra (or

portions thereof). Nevertheless, this structure has been cited, usually without qualification, no fewer than some 35 times in the literature on "WB_4", and quite frequently in the past five years.

The structure proposed here may be imagined as a highly defective version of a hypothetical *P6/mmc* (AlB_2-type) WB_2 structure. As such, if all of the possible tungsten sites were fully occupied, a structure with idealized W-W and B-B distances would result. Conversely, the absent tungsten sites appear to give rise to the opportunistic formation of slightly distorted cuboctahedral boron cages. This finding is especially satisfying in light of the stoichiometric position of $WB_{4.2}$ between MB_2-type compounds, which contain exclusively boron 'nets', and MB_x phases with $x > 2$, such as UB_{12}. The motifs in these higher boron-content materials are increasingly dominated by polyhedral sub-units. This analogy is especially apparent when a somewhat fictional representation of this tungsten boride (where *all 6(h)* sites are shown occupied) is compared against the cubic packing of a scaled UB_{12}, as in Figure 6.9. Consequently, the predominant distinctions between these two structure types are: (1) $WB_{4.2}$ is hexagonal, while most dodecaborides are cubic; (2) the occurrence of cuboctahedra in MB_{12} structures is one per metal atom, whereas it is one for every four metal atoms in $WB_{4.2}$; and (3) the cuboctahedra of $WB_{4.2}$ are randomly distributed. These differences can be rationalized by noting that the formation of dodecaborides containing well-ordered cuboctahedra depends strongly on the radius of the metal atom with Y (1.80 Å)[39] and Zr (1.60 Å)[39] being, respectively, the largest and smallest metals forming dodecaborides under ambient pressure [40]. In comparison, the radius of W is only 1.39 Å [39], which is too small to accommodate one cuboctahedral cage per metal atom.

In our model, we have established that not all of the *6(h)* sites are occupied by boron, and neither are all of the *2(b)* sites vacant of tungsten; instead, vacancies and concomitant occupancies of these sites appear to follow a random distribution. According to our Rietveld results, the occupancy of tungsten in Wyckoff *2(b)* approaches exactly 2/3 and that of boron in Wyckoff *6(h)* approaches exactly 1/3. If this is the case, each unit cell contains, on average, one boron 'trimer' to replace each tungsten absence. If the cuboctahedra are so arranged as to lead to maximal spacing, no two cuboctahedra would ever coincidentally occupy any part of the same unit cell, leading to a minimum of lattice strain. There is, however, a possibility of these occupancies being somewhat variable in spacing, particularly as a function of the excess boron used to drive the formation of the higher boride phase, as evidenced by the large spread in lattice parameters reported in the literature. We believe the lattice parameters presented here represent an upper limit for the binary system.

The model proposed here is supported by data presented by Cheng *et al*. [21], who, using aberration corrected high-resolution transmission electron microscopy, claimed to have *visualized* "interstitial boron" in $WB_{4.2}$. Nevertheless, the authors hypothesized that the "true" formula for the compound is WB_3, a composition they arrived at using particle swarm computational methods assuming full occupancies. In light of the microscopic evidence, they were forced to modify this formula to WB_{3+x} where $x \approx 0.343 - 0.375$. Had the authors combined these two pieces of information, for instance by providing crystallographic positions for their "interstitial" boron, they would have found that full tungsten occupancy and boron occupancy in the sites they visualized are mutually exclusive. This contradiction would have been apparent if they had refined the X-ray diffraction pattern reported in their own work, and is presumably the reason they did not assign a

definitive crystallographic structure. Had the partial occupancy of tungsten been included in their proposed formula, they would have arrived at $W_{0.833}B_{3.343}$ – $W_{0.833}B_{3.75}$ = $WB_{4.01}$ – $WB_{4.05,}$ which is fairly close to the value of $WB_{4.2}$ reported here.

Conclusions

In this work, we have presented a new crystal structure for the highest boride of tungsten, obtained by the simultaneous refinement of X-ray and neutron scattering data. The structure of this material has been debated for more than half a century, but the need for a definitive structure has increased dramatically in recent years, since the discovery that $WB_{4.2}$ is both super-hard and can serve as the parent phase for a large family of solid-solutions that are even harder [8,11,12]). While the crystal structure reported here contains some elements postulated previously – sites that are only partly occupied by tungsten, for example [14,17,18,22] – the structure has many new elements as well. The most important of these is the fact that the partially occupied tungsten sites that do not contain W atoms contain boron timers, and these trimers are within the appropriate distance to couple with the boron layers, producing slightly distorted boron cuboctahedral boron cages. We postulate that this cage structure is the primary bonding motif responsible for the remarkable hardness of $WB_{4.2}$.

We conclude by considering the implications of this new crystal structure to the hardness of $WB_{4.2}$. As mentioned above, $WB_{4.2}$ is capable of hosting a wide range of solute atoms, and these solute atoms can have a profound effect on hardness, even at very low concentration [12]. Having an accurate model for $WB_{4.2}$ provides valuable insight toward understanding these phenomena and more directly predicting the means of manipulating the crystal chemistry of this compound.

For a low volume, high symmetry, binary compound, the unit cell of $WB_{4.2}$ contains an unusually large number of unique crystallographic sites. By carefully tailoring a solid solution scheme, it may be possible to specifically select guest atoms to replace only the fully occupied tungsten site, only the partially occupied site, or both. It may further be possible to introduce other metals or heteroatoms at the vacant *2(d)* position, replacing the cuboctahedra with metal atoms or, conversely, enhancing the frequency and regularity with which they occur [9]. Changes in the spatial distribution of boron cuboctahedra upon doping with metal heteroatoms could turn out to be the basis for the extraordinary changes in hardness that can be achieved at doping levels of just a few percent. Perhaps most importantly, however, the existence of an accurate crystal structure for $WB_{4.2}$ should aid the rational design of new super-hard solid solutions using computational methods. As such, this new crystal structure has real potential to lead to improvements in next generation super-hard materials.

Table 6.1: Relevant Crystallographic Data for the Highest Boride of Tungsten*

Atom	***x***	***y***	***z***	***Occupancy***	***Uiso***
W1	2/3	1/3	1/4	1	0.00195
W2	0	0	1/4	0.6412(6)	0.0013
B1	0.33167(11)	0	0	1	0.00171
B2	0.11887(11)	0.23775(23)	1/4	0.3569(11)	0.0044

Atom	U_{11}	U_{22}	U_{33}	U_{12}	U_{13}	U_{23}
W1	0.00287(4)	0.00287(4)	0.00011(7)	0.001435(2)	0	0
W2	0.00191(8)	0.00191(8)	0.00009(15)	0.00096(4)	0	0
B1	0.001424(1)	0.001350(3)	0.002326(2)	0.000673(1)	0.00040(5)	0.00079(10)
B2	0.00779(19)	0.00312(26)	0.00074(21)	0.00156(13)	0	0

* Numbers in parentheses represent the uncertainty of the proceeding least significant figure.

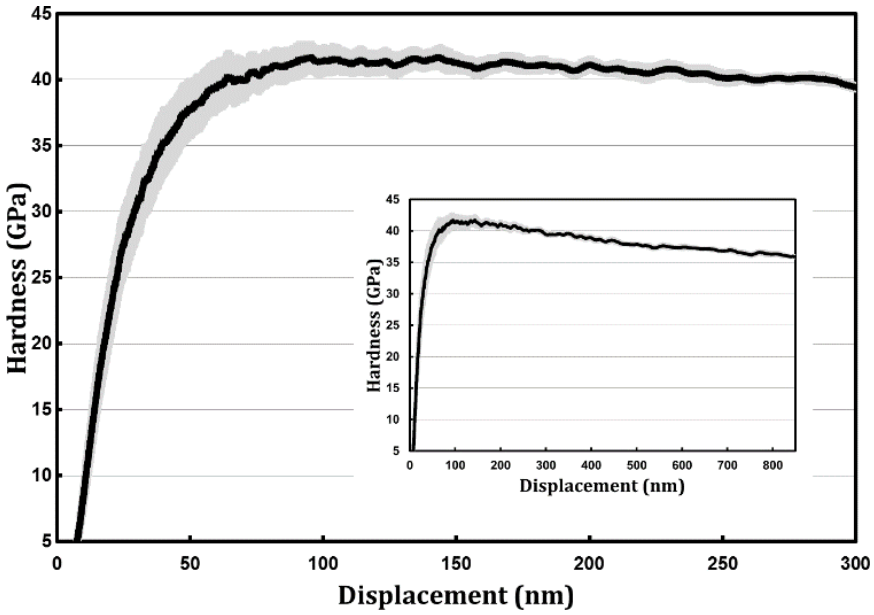

Figure 6.1: Plot of average nano-indentation hardness versus displacement for 20 measurements on WB_4, indicating super-hardness (hardness above 40 GPa) from ~60 nm displacement to ~250 nm. The average hardness over this range is 40.9 ± 1.1 GPa with a maximum value of 41.7 ± 1.3 GPa at 95.25 nm. The shaded area represents the 95% confidence interval. **Inset:** The full hardness curve from 0 – 850 nm. The average value of hardness from 60 – 850 nm is 39.7 ± 0.8 GPa. Numbers following the ± sign represent standard deviations.

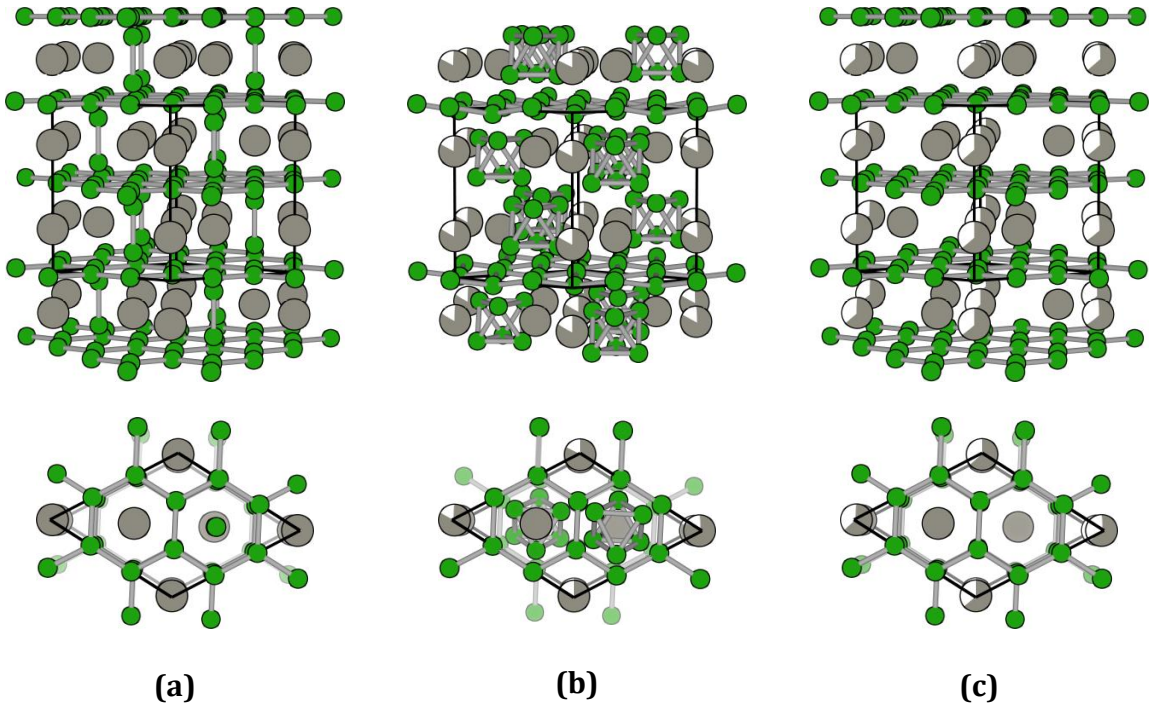

Figure 6.2: Comparison of the various proposed structures of WB_4. **(a)** The structure of "WB_4" by Romans and Krug(15) **(b)** The structure of "$W_{1.83}B_9$" according to Nowotny *et al.*[17] and **(c)** The structure of "$W_{1-x}B_3$" following Lundström and Rosenberg[18] and Zeiringer *et al*.[14] Green spheres represent boron atoms and grey spheres represent tungsten atoms. Partial occupancy is indicated by partial sphere-filling. Bonds are shown to clarify the spatial arrangement. (All models produced using VESTA)[48]

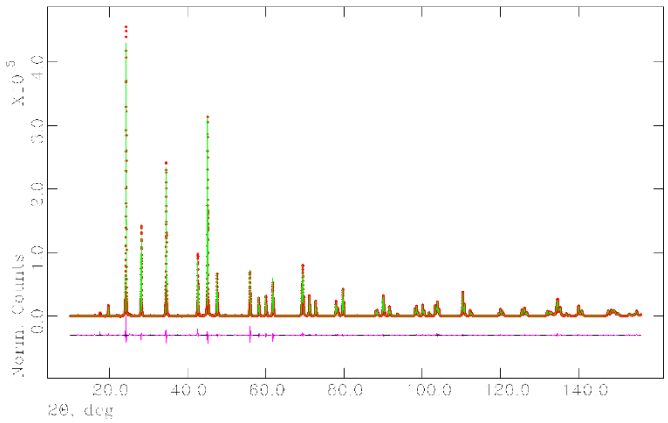

(a)

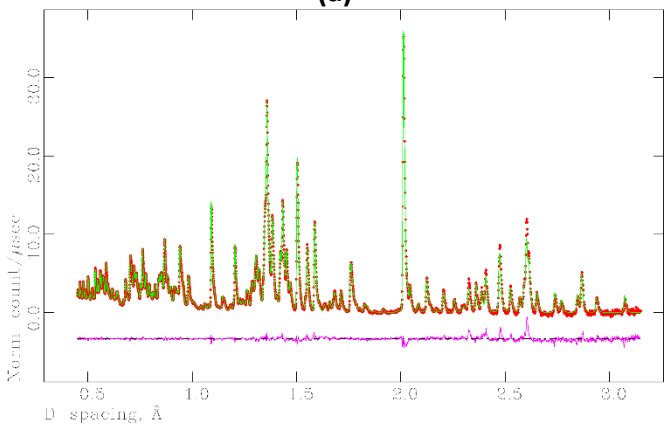

(b)

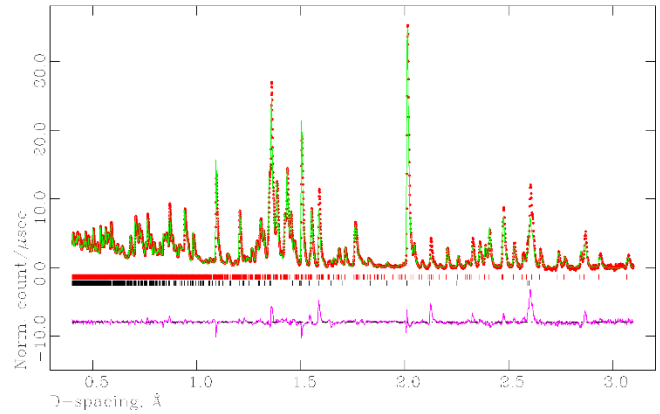

(c)

Figure 6.3: (a) X-ray and **(b)** neutron powder diffraction patterns for the highest boride of tungsten. Red points indicate observed data, the green line represents the fit against the final model. The difference between the two is shown beneath (magenta line). The background has been subtracted for clarity. **(c)** is the best fit to the neutron diffraction data without the inclusion of the trigonal boron clusters.

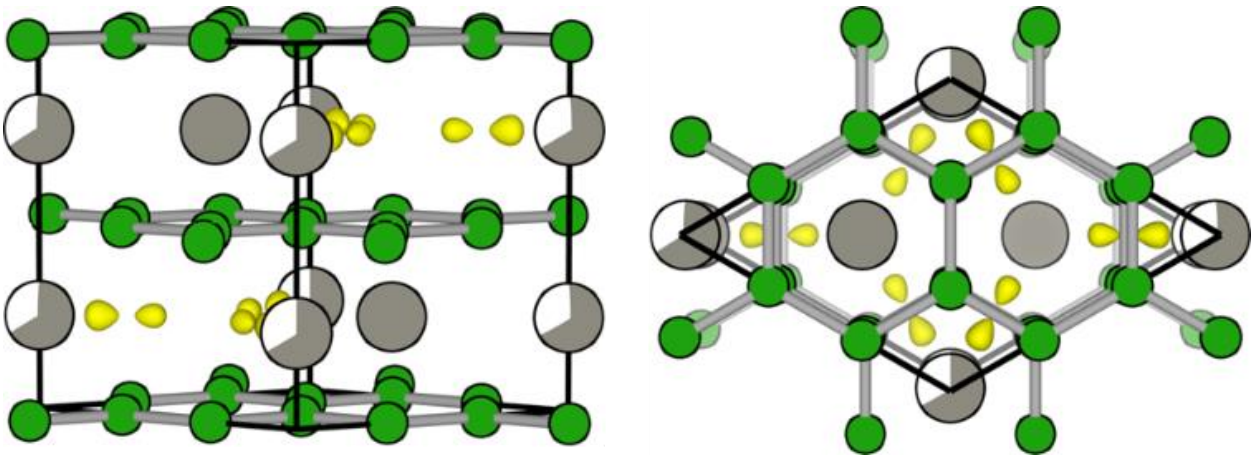

Figure 6.4: 3-dimentional Fourier difference map (yellow) from the neutron refinement overlaid on the boron-deficient model structure lacking interstitial boron. Green spheres represent boron atoms and grey spheres represent tungsten atoms.

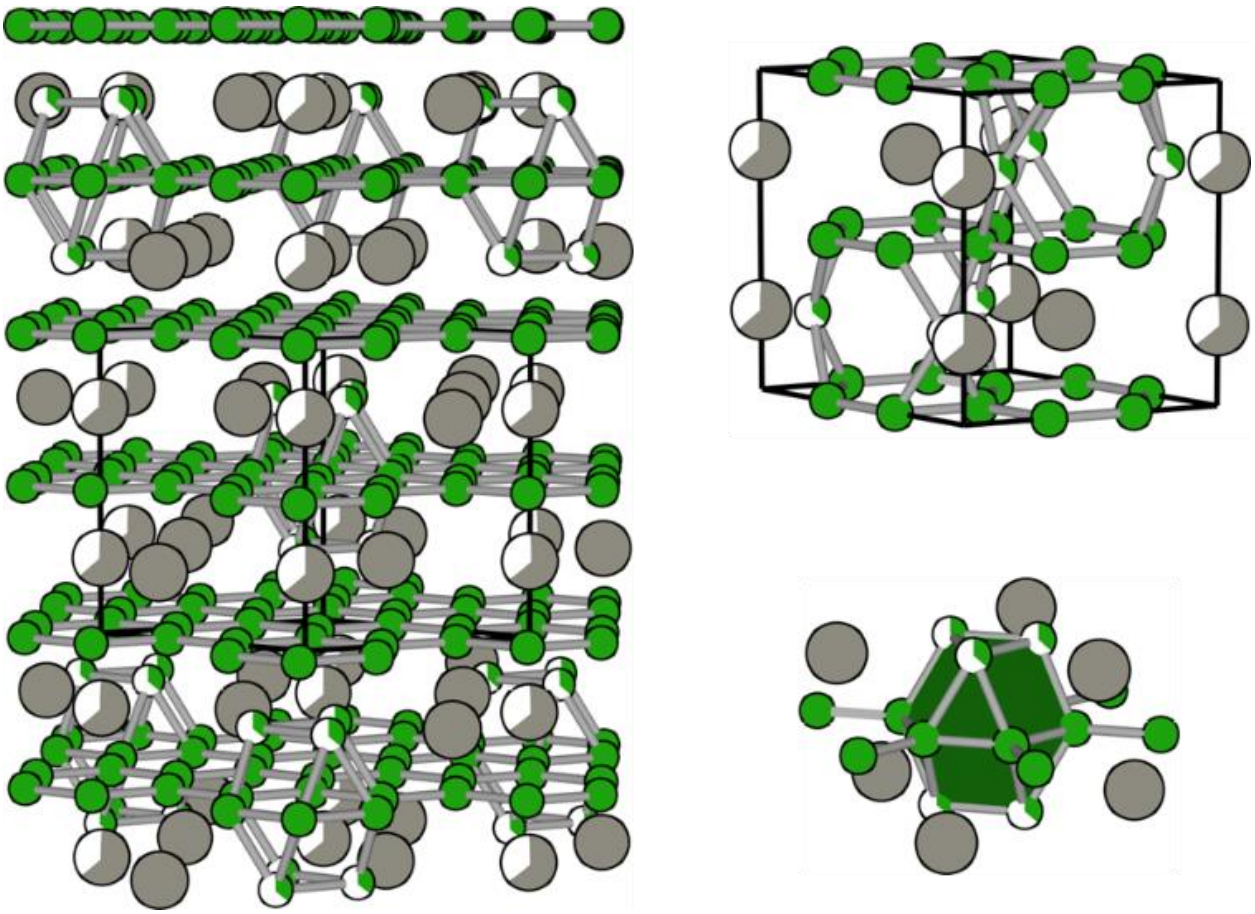

Figure 6.5: The proposed structure of the highest boride of tungsten.

Figure 6.6: Backscattered electron SEM image of a fractured ingot of an arc-melted sample in the ratio W:B of 1:12. Light regions are the tungsten-containing phase.

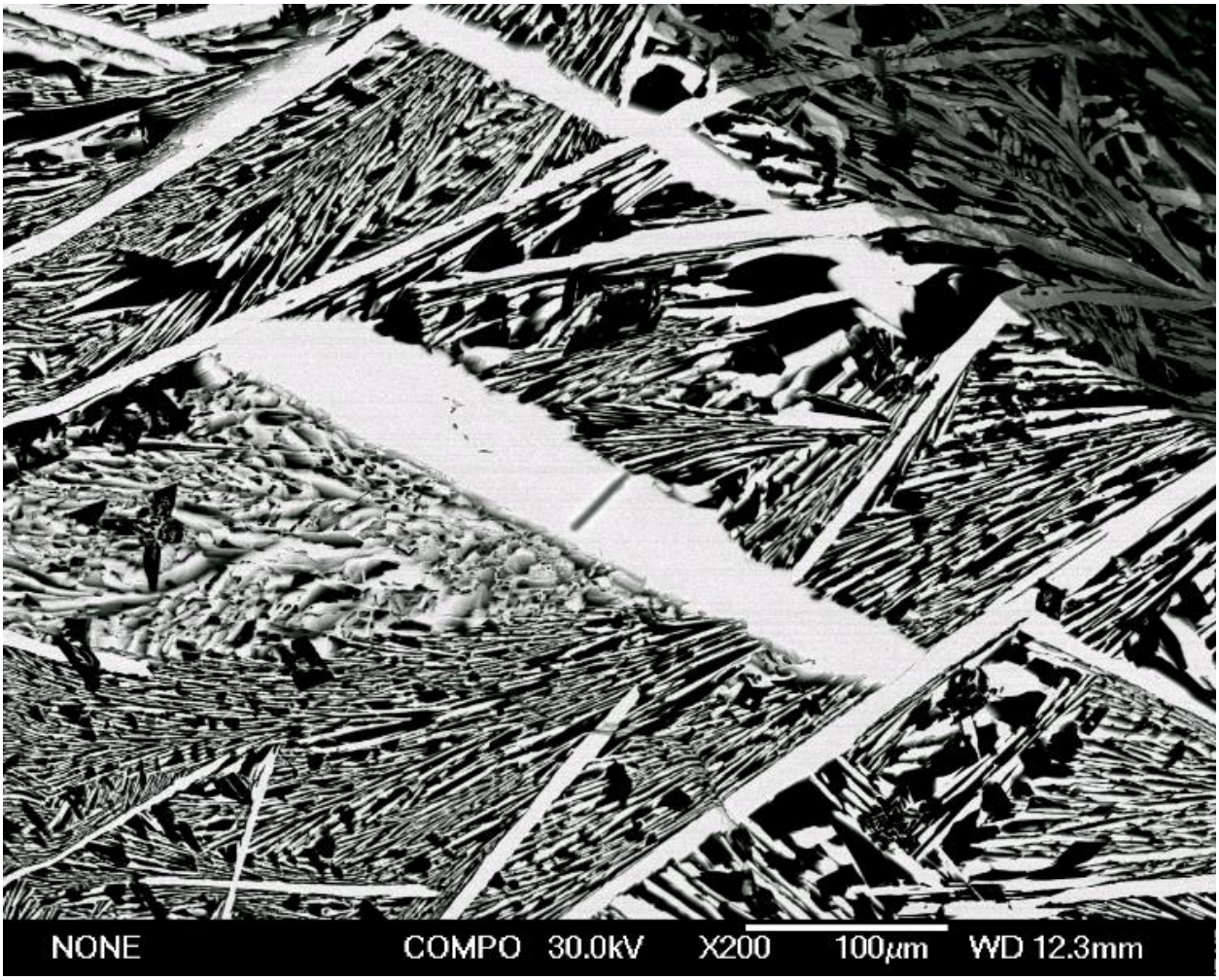

Figure 6.7: SEM image of a sectioned $W^{11}B_{12}$ ingot in backscattered electron (compositional) mode indicating compositional uniformity of $WB_{4.2}$ (bright) grains.

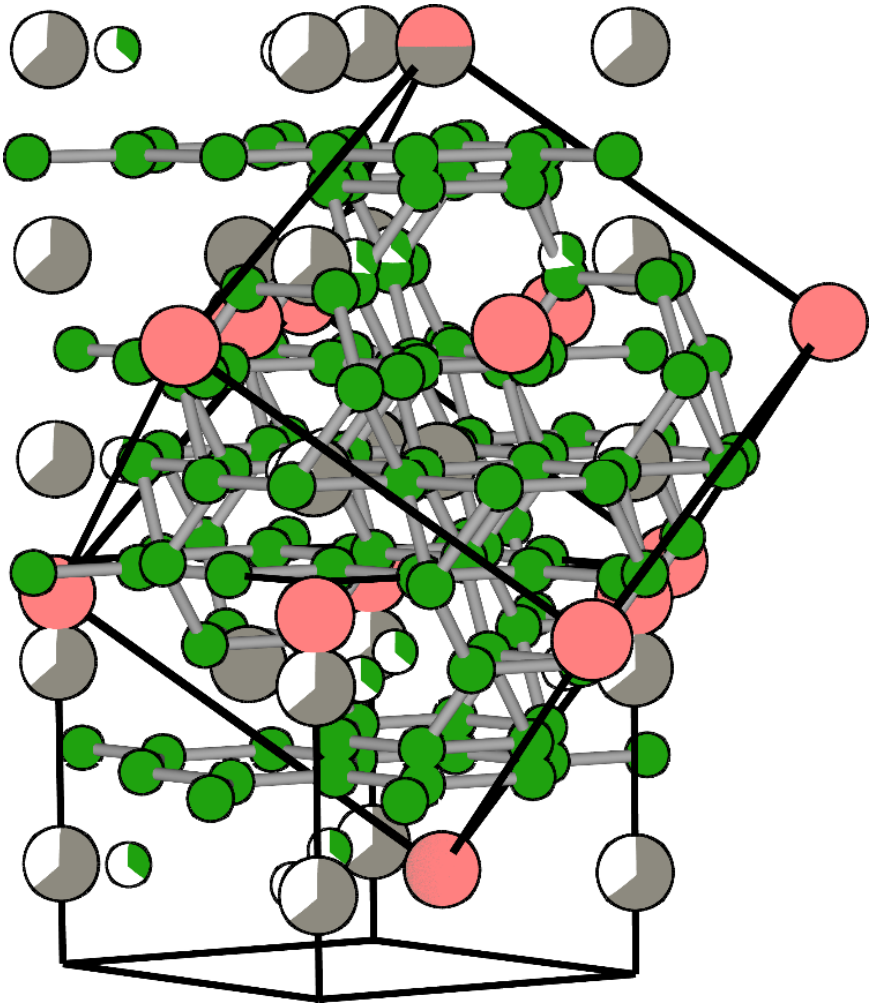

Figure 6.8: Overlay of the UB_{12} structure type on $WB_{4.2}$ showing a close similarity.

References

(1) Cumberland, R.W.; Weinberger, M.B.; Gilman, J.J.; Clark, S.M.; Tolbert, S.H.; Kaner, R.B. Osmium Diboride, An Ultra-Incompressible, Hard Material. *J. Am. Chem. Soc.*, **2005**, 127:7264–7265.

(2) Chung, H.Y.; Weinberger, M.B.; Levine, J.B.; Kavner, A.; Yang, J.M.; Tolbert, S.H.; Kaner, R.B. Synthesis of ultra-incompressible superhard rhenium diboride at ambient pressure. *Science*, **2007**, 316:436–9.

(3) Kaner R.B.; Gilman J.J.; Tolbert S.H. Materials science. Designing superhard materials. *Science*, **2005**, 308:1268–9.

(4) Levine, J.B.; Tolbert, S.H.; Kaner, R.B. Advancements in the Search for Superhard Ultra-Incompressible Metal Borides. *Adv. Funct. Mater.*, **2009**, 19:3519–3533.

(5) Komanduri R.; Shaw MC. Wear of synthetic diamond when grinding ferrous metals. *Nature*, **1975**, 255:211–213.

(6) Cook, M.; Bossom, P. Trends and recent developments in the material manufacture and cutting tool application of polycrystalline diamond and polycrystalline cubic boron nitride. *Int. J. Refract. Met. Hard. Mater.*, **2000**, 18:147–152.

(7) Brazhkin, V.V.; Lyapin, A.G.; Hemley, R.J. Harder than diamond: Dreams and reality. *Philos. Mag. A*, **2002**, 82:231–253

(8) Mohammadi, R.; Lech, A.T.; Xie, M.; Weaver, B.E.; Yeung, M.T.; Tolbert, S.H.; Kaner, R.B. Tungsten tetraboride, an inexpensive superhard material. *Proc. Natl. Acad. Sci.*, **2011**, 108:10958–10962.

(9) Mohammadi, R.; Xie, M.; Lech, A.T.; Turner, C.L.; Kavner, A.; Tolbert, S.H.; Kaner, R.B. Toward Inexpensive Superhard Materials: Tungsten Tetraboride-Based Solid Solutions. *J. Am. Chem. Soc.*, **2012**, 134:20660–20668.

(10) Xie, M.; Mohammadi, R.; Mao, Z.; Armentrout, M.M.; Kavner, A.; Kaner, R.B.; Tolbert, S.H. Exploring the high-pressure behavior of superhard tungsten tetraboride. *Phys. Rev. B*, **2012**, 85:64118.

(11) Gu, Q.; Krauss, G.; Steurer, W. Transition Metal Borides: Superhard versus Ultra-incompressible. *Adv. Mater.*, **2008**, 20:3620–3626.

(12) Xie, M.; Mohammadi, R.; Turner, C.L.; Kaner, R.B.; Kavner, A.; Tolbert, S.H. Lattice stress states of superhard tungsten tetraboride from radial x-ray diffraction under nonhydrostatic compression. *Phys. Rev. B*, **2014**, 90(10), p.104104.

(13) Chretien, A.; Helgorsky, J. On New Boride Compositions of Molybdenum and Tungsten, MoB_4 and WB_4. *Comptes. Rendus.* **1961**, 252:742–744.

(14) Zeiringer, I. *et al*. Crystal Structure of $W_{1-x}B_3$ and Phase Equilibria in the Boron-Rich Part of the Systems Mo-Rh-B and W-{Ru,Os,Rh,Ir,Ni,Pd,Pt}-B. *J. Phase Equilibria Diffus*., **2014**.

(15) Romans, P.A.; Krug, M.P. Composition and crystallographic data for the highest boride of tungsten. *Acta Crystallogr.,* **1966**, 20:313–315.

(16) Kiessling, R.; Wetterholm, A.; Sillén, L.G.; Linnasalmi, A.; Laukkanen, P. The Crystal Structures of Molybdenum and Tungsten Borides. *Acta Chem. Scand.*, **1947**, 1:893–916.

(17) Nowotny, H.; Haschke, H.; Benesovsky, F. Bor-reiche Wolframboride. *Monatshefte für Chemie. / Chem. Mon.,* **1967**, 98:547–554.

(18) Rosenberg, I.; Lundström, T. The crystal structure of the molybdenum boride $Mo_{1-x}B_3$. *J. Solid State Chem.,* **1973**, 6:299–305.

(19) Liang, Y.; Gou, Y.; Yuan, X.; Zhong, Z.; Zhang W. Unexpectedly hard and highly stable WB_3 with a noncompact structure. *Chem. Phys. Lett.,* **2013**, 580:48–52.

(20) Zang, C.; Sun, H.; Chen, C. Unexpectedly low indentation strength of WB_3 and MoB_3 from first principles. *Phys. Rev. B,* **2012**, 86:180101.

(21) Cheng, X. *et al*. Interstitial-boron solution strengthened WB_{3+x}. *Appl. Phys. Lett.,* **2013**, 103:171903.

(22) Gou, H.; Li, Z.; Wang, L.; Lian, J.; Wang, Y. Peculiar structure and tensile strength of WB_4: nonstoichiometric origin. *AIP Adv.,* **2012**, 2:12171.

(23) Zhang, R.F. *et al*. Stability and Strength of Transition-Metal Tetraborides and Triborides. *Phys. Rev. Lett.,* **2012**, 108:255502.

(24) Liang, Y. *et al*. An unexpected softening from WB_3 to WB_4. *Europhys. Lett.,* **2012**, 98:66004.

(25) Wang, M.; Li, Y.; Cui, T.; Ma, Y.; Zou, G. Origin of hardness in WB_4 and its implications for ReB_4, TaB_4, MoB_4, TcB_4, and OsB_4. *Appl. Phys. Lett.,* **2008**, 93:101905.

(26) Zhang, M.; Yan, H.; Wei, Q.; Wang, H. Universal ground state hexagonal phases and mechanical properties of stoichiometric transition metal tetraborides: TMB_4 (TM=W, Tc, and Re). *Comput. Mater. Sci.,* **2014**, 68:371–378.

(27) Zhao, E.; Meng, J.; Ma, Y.; Wu, Z. Phase stability and mechanical properties of tungsten borides from first principles calculations. *Phys. Chem. Chem. Phys.,* **2010**, 12:13158–65.

(28) Liang, Y.; Yuan, X.; Zhang, W. Thermodynamic identification of tungsten borides. *Phys. Rev. B.*, **2011**, 83:220102.

(29) Liang, Y. et al. Polytypism in superhard transition-metal triborides. *Sci. Rep.*, **2014**, 4:5063.

(30) Cheng, X.-Y., Chen, X.-Q., Li, D.-Z., Li, Y.-Y. Computational materials discovery: the case of the W-B system. *Acta Crystallogr. Sect. C, Struct. Chem.*, **2014**, 70:85–103.

(31) Bullett, D.W. in *AIP Conference Proceedings* (AIP), **1986**, pp 249–259.

(32) Bullett, D.W. in *AIP Conference Proceedings* (AIP), **1991**, pp 21–28.

(33) Albert, B.; Hillebrecht, H. Boron: Elementary Challenge for Experimenters and Theoreticians. *Angew. Chemie. Int. Ed.*, **2009**, 48:8640–8668.

(34) Widom, M.; Mihalkovič, M. Symmetry-broken crystal structure of elemental boron at low temperature. *Phys. Rev. B.*, **2008**, 77:064113.

(35) Hoard, J.L.; Sullenger, D.B.; Kennard, C.H.L.; Hughes, R.E. The structure analysis of *β*-rhombohedral boron. *J. Solid State Chem.*, **1970**, 1:268–277.

(36) Werheit, H. *et al*. Isotopic phonon effects in *β*-rhombohedral boron—non-statistical isotope distribution. *J. Phys. Condens. Matter.*, **2012**, 24:175401.

(37) Favia, P.; Stoto, T.; Carrard, M.; Stadelmann, P.-A.; Zuppiroli, L. Order and Disorder in Boron Phases. *Microsc. Microanal. Microstruct.*, **1996**, 7:225–234.

(38) Kiessling, R. The Borides of Some Transition Elements. *J. Electrochem. Soc.*, **1951**, 98:166–170.

(39) Pauling, L. Atomic Radii and Interatomic Distances in Metals. *J. Am. Chem. Soc.*, **1947**, 69:542–553.

(40) Placa, S.; La Binder, I.; Post, B. Binary dodecaborides. *J. Inorg. Nucl. Chem.*, **1961**, 18:113–117.

(41) Oliver, W.C.; Pharr, G.M. An improved technique for determining hardness and elastic modulus using load and displacement sensing indentation experiments. *J. Mater. Res.*, **2011**, 7:1564–1583.

(42) Hölzer, G.; Fritsch, M.; Deutsch, M.; Härtwig, J.; Förster, E. $K_{\alpha\{1,2\}}$ and $K_{\beta\{1,3\}}$ x-ray emission lines of the 3d transition metals. *Phys. Rev. A.*, **1997**, 56:4554–4568.

(43) Rietveld, H.M. A profile refinement method for nuclear and magnetic structures. *J. Appl. Crystallogr.*, **1969**, 2:65–71.

(44) Toby, B.H. EXPGUI , A graphical user interface for GSAS. *J. Appl. Crystallogr.*, **2001**, 34:210–213.

(45) Larson, A.C.; Von Dreele, R.B. General Structure Analysis System (GSAS). *Los Alamos Natl Lab Rep*. **2000**

(46) Dolomanov, O. V.; Bourhis, L.J.; Gildea, R.J; Howard, J.A.K.; Puschmann, H. OLEX2 : a complete structure solution, refinement and analysis program. *J. Appl. Crystallogr.*, **2009**, 42:339–341.

(47) Momma, K.; Izumi, F. VESTA : a three-dimensional visualization system for electronic and structural analysis. *J. Appl. Crystallogr.,* **2008**, 41:653–658.

Chapter 7

Introduction

The concept of creating superhard borides by incorporating boron into the dense structure of transition metals such as ruthenium (Ru), osmium (Os) and rhenium (Re) has become well established over the past few years.[1,2] With increasing demand for high-performance and long-lasting cutting and forming tools, the members of this expanding class of superhard metals hold promise to address the shortcomings of traditional tool materials. Those shortcoming include their high cost (silicon nitride, cubic boron nitride, and diamond), their inability to cut ferrous metals due to chemical reactions (diamond), instability in the presence of humidity (cubic boron nitride) and relatively low hardness (tungsten carbide).[3] In contrast, rhenium diboride (ReB_2) has demonstrated exciting properties including high hardness (>40 GPa),[4] the ability to scratch diamond,[5] excellent electrical conductivity,[6] a high shear modulus (267-273 GPa),[7,8] and straightforward synthesis under ambient pressure.[5] Unfortunately, however, rhenium is a member of the platinum group metals and therefore is prohibitively expensive. The on-going search for new superhard borides with increased hardness and reduced cost of production has recently led to tungsten tetraboride (WB_4), an inexpensive member of this growing family of superhard materials.

Although some early studies looked at the synthesis and crystallography of WB_4,[9,10] its superhard nature was not explored until 2002 by Brazhkin *et al*.[11] After we discussed the potential applications of this superhard boride in a *Science* Perspective in 2005,[1] a few studies examined its mechanical properties both in bulk and thin film form.[12-14] Recently, we examined the hardness and high-pressure behavior of WB_4 in some detail.[15,16] Using microindentation, nanoindentation,

and *in situ* high-pressure X-ray diffraction, we measured a Vickers hardness of 43.3 GPa (under an applied load of 0.49 N), a nanoindentation hardness of 40.4 GPa (at a penetration depth of 250 nm), and a bulk modulus of 326-339 GPa for WB_4 samples synthesized by arc melting at ambient pressure.[16] Under an extremely high pressure of ~42 GPa (~415,000 atm), WB_4 exhibits a unique second-order phase transition that can be attributed to its very strong but non-flexible cage-like crystal structure.[17] Additionally, we showed that by adding ~1 at.% rhenium (Re) to WB_4, the Vickers hardness (under a 0.49 N applied load) increases from 43.3 GPa to 49.8 GPa due to a dispersion hardening mechanism obtained from the formation of an ReB_2-type second phase. This work thus showed that extrinsic component could modify the hardness in this system.[16]

Although the formation of a second phase is one way to enhance the mechanical properties, single phase materials are usually preferred because of the non-uniformity that the second phase introduces in the structure of the matrix. Solid-solution hardening is often considered as an alternative route to improve the hardness and other mechanical properties of crystalline materials without adding an extrinsic component to the structure and properties of the host material.[18] This hardening method can arise from two entirely different mechanisms: size mismatch[19] and/or valence electron count difference[20] between the atoms of solute and solvent. Indeed, the formation of solid solutions of hard ruthenium diboride (RuB_2) with osmium (Os) previously demonstrated some promising improvements in hardness.[21] In a recent study we used a similar approach to examine the possibility of further enhancing the hardness of WB_4 by individually doping it with 0-50 at.% tantalum (Ta), manganese (Mn) and chromium (Cr).[22] We found that when Ta and Mn are each added to WB_4, three very distinct increases were seen in its Vickers hardness curves, under all applied loads between 0.49 and 4.90 N, when plotted against composition (0-50 at.% Ta or Mn). A sharp increase in hardness at low concentrations of ~2 at.% Ta or 4 at.% Mn was

observed and attributed to the valence electron difference between W (group 6) and Ta (group 5) or Mn (group 7), the two broad peaks at maximum solubility (~20 at.% Ta or Mn) and high concentrations (~40 at.% Ta or Mn) were associated with atomic size mismatches between W (1.41 Å) and Ta (1.49 Å) or Mn (1.32 Å),[23] with changes in interfaces between grains, and with dispersion hardening from TaB_2 or MnB_4, respectively.

In the case of chromium (Cr) in WB_4, however, only two hardness peaks were seen at ~10 and 40 at.% Cr. While the broad peak at ~ 40 at.% Cr was clearly due to the dispersion hardening of CrB_2 and CrB_4, we could not draw certain conclusion about the origin of the relatively broad peak that was observed at ~10 at.% Cr. The maximum solubility of Cr in WB_4 is ~10 at.% Cr, so it is unclear if this peak is due to the atomic size mismatch between W (1.41 Å) and Cr (1.30 Å)[24] at maximum solubility, to electronic structure changes, despite the fact that W and Cr are isoelectronic (group 6), or to some interfacial/grain boundary effects. Conversely, understanding the answer to this question is a key component of our ability to create new hard solid solutions based on rational design.

To clarify this, we have embarked on the current study, where we have designed a similar, but much cleaner system, by creating solid solutions of molybdenum (Mo) in WB_4. Lying in the same column of the Periodic Table (group 6), Mo has the same number of valence electrons as W and Cr. In addition, since Mo has a close atomic radius to W (W = 1.41 Å, Mo = 1.39 Å, note B = 0.78 Å)[24] and both WB_4 and MoB_4 are hexagonal and crystallize in the *$P6_3/mmc$* space group, with almost identical lattice parameters,[10,16,23,24] one would expect to obtain an extended range when solid solutions of Mo inWB_4 can be created. These facts should lead to the absence of solid-solution hardening due to either atomic size mismatch or dispersion hardening from a second phase. In this work, we thus, report the synthesis of molybdenum-doped tungsten tetraboride solid

solutions containing a broad range of Mo concentrations varying from 0-50 at.% (i.e.$W_{1-x}Mo_xB_4$ with x = 0.00-0.50). An investigation of the changes in load-dependent Vickers hardness across the entire solubility range of Mo from 0-50 at.% indicates that the hardness of WB_4 can be significantly increased by adding Mo to WB_4, and the underlying hardening mechanism(s) can be understood.

Materials and Methods

To synthesize the samples in each concentration, powders of pure tungsten (99.95%, Strem Chemicals, USA), molybdenum (99.9%, Strem Chemicals, USA) and amorphous boron (99+%, Strem Chemicals, USA) were blended thoroughly using a digital vortex mixer, followed by grinding in an agate mortar and pestle set, to achieve a uniform mixture. The ratio of boron to tungsten was kept constant at 12:1 in all samples to stabilize the structure of WB_4 and inhibit the formation of the thermodynamically favorable phase, tungsten diboride (WB_2).[10,16] The mixture was then compacted to a pellet in a steel die using a hydraulic Carver press and applying a pressure of ~2,000 lbs. The pellets each weighing ~500 mg were synthesized, under high-purity argon at ambient pressure, in a home-made arc melting furnace using a maximum applied AC current of ~130 amps sustained for ~3 minutes. The as-synthesized ingots were dissected using a sinter-bonded diamond lapidary sectioning saw (South Bay Technology Inc., USA). Half of each ingot was crushed into a fine powder, using a hardened-steel mortar and pestle set, for powder X-ray diffraction and thermal gravimetric experiments. The other half was mounted in epoxy at room temperature using a cold-mount resin and hardener epoxy set (Allied High Tech Products Inc., USA). The mounted sample was polished with a tripod polisher (South Bay Technology Inc., USA) using polishing papers of grit sizes ranging from 120-1200 (Allied High Tech Products Inc.,

USA), followed by abrasive films containing diamond particles ranging from 30 - 0.5 μm in size (South Bay Technology Inc., USA), to achieve an optically smooth surface for elemental analysis and hardness testing.

Energy-dispersive X-ray spectroscopy (EDS) and powder X-ray diffraction (XRD) were used to examine the elemental composition and phase purity of the samples, respectively. EDS analysis was carried out on the polished samples using an EDAX detector mounted on a scanning electron microscope (JEOL JSM 6700 F, Japan). For phase identification, powder X-ray diffraction (XRD) was performed on the crushed-to-powder samples using an X'Pert Pro™ powder X-ray diffraction system (PANalytical, Netherlands). XRD patterns were collected from the powder samples using a $Cu_{K\alpha}$ X-ray radiation (λ = 1.5418 Å) and the following scan settings: scan range 2θ = 10-140 deg, step size = 0.0167 deg, time per step = 85.1 s and scan speed = 0.025 deg/s. The patterns were then compared with reference patterns available in the Joint Committee on Powder Diffraction Standards (JCPDS) database to determine the phases present in the samples.

Once the purity of the samples was confirmed, we performed hardness testing on the polished samples. Hardness measurements were carried out using a MicroMet® 2103 microindentation system (Buehler Ltd., USA) equipped with a pyramid diamond indenter tip with Vickers geometry. To study the load-dependent hardness of WB_4-Mo solid solutions, five different loads of 0.49 (low load), 0.98, 1.96, 2.94 and 4.90 N (high load) were applied to the surface of the samples with a dwell time of 15 s. To ensure accurate measurements, the samples were indented at least 20 times at randomly chosen spots under each load. The lengths of the diagonals of the impression marks, created by the indenter on the surface of the samples, were then measured using a high-resolution Zeiss Axiotech® 100HD optical microscope (Carl Zeiss Vision GmbH,

Germany) under a total magnification of 500×. The Vickers microindentation hardness values (H_V, in GPa), under various applied loads, were calculated using the following equation:[16]

$$H_V = 1854.4\ P / d^2 \qquad \text{(Eq. 7.1)}$$

where P is the applied load in Newtons (N) and d is the arithmetic mean of the diagonals of the indent mark in micrometers.

Thermal gravimetric analysis was utilized to test the thermal stability of the hardest solid solution in the WB_4-Mo system, $W_{0.97}Mo_{0.03}B_4$. Using a Pyris Diamond thermogravimetric/differential thermal analyzer unit (TG-DTA, Perkin Elmer Instruments, USA), a powder sample of this superhard solid solution was heated up to 200 ºC in air, at a rate of 20 ºC/min, and soaked at this temperature for 20 minutes to remove any moisture. The sample was then heated to 1000 ºC at a rate of 2 ºC/min and held at this temperature for 120 minutes. The sample was next air cooled to room temperature at a rate of 5 ºC/min. In order to compare the thermal stability of this solid solution with that of a conventional cutting tool material, we repeated our TGA experiment on a tungsten carbide powder sample (WC, 99.5%, Strem Chemicals, USA) in air using the same experimental conditions. The solid products of the thermal reactions were identified using powder X-ray diffraction.

Results and Discussion

Energy-dispersive X-ray spectroscopy (EDS) confirmed the absence of any impurity elements in the as-synthesized samples. Using this technique, we also verified the desired stoichiometry of the elements comprising the samples synthesized at each concentration, 0-50 at.%

Mo in WB_4. A selection of the X-ray diffraction (XRD) patterns of the synthesized compounds in the WB_4-Mo system is shown in Fig. 7.1.

Figure 7.1 shows that single phase solid solutions of Mo in WB_4 can be formed over the entire composition range studied (0-50 at.%). The bottom pattern corresponds to WB_4 (JCPDS, Ref. Code: 00-019-1373) and no softer impurity phases such as WB_2 (which has major peaks at 2θ = 25.683, 34.680 and 35.275º) are observed. All samples, however, do contain some extra crystalline boron which is not observable within the resolution of our powder X-ray diffraction instrument. Table 7.1 reports the lattice parameters and important *d*-spacings for a number of WB_4-Mo solid solutions. It can be observed from the data in this Table that the lattice parameters of WB_4 increase almost linearly with the addition of Mo, with R^2-values of 0.85 for *a*, 0.86 for *c* and 0.86 for *V*. Similar trends are seen for the changes for each individual sample in the *d*-spacing.

The changes in Vickers hardness for solid solutions of Mo in WB_4, under loads ranging from 0.49-4.90 N, are shown in Fig. 7.2. This figure displays a clear indentation size effect (ISE) for all the solid solutions. This phenomenon, which has also been observed in the hardness behavior of other superhard borides,[2,5,22] is an inherent property of these compounds and likely arises from the load dependent opening of new slip systems, from an elastic-plastic deformation transition, and/or from initiation and propagation of sub-surface cracks.[2,16] It is also observed from Figure 7.2 that the Vickers hardness, under an applied load of 0.49 N (low load) starts at 43.3 ± 2.9 GPa for pure WB_4, and then shows a relative sharp increase in hardness that peaks at 50.3 ± 3.2 GPa with a concentration of just 3 at.% Mo. After the peak, the hardness decreases almost linearly with a very gradual slope to a value of 39.6 ± 0.94 GPa for 50 at.% Mo addition. Similar trends are seen for the other hardness loads (0.98, 1.96, 2.94 and 4.90 N). For example, Vickers hardness under high load (4.90 N) shows a 15.9% increase from 28.1 ± 1.4 GPa for pure WB_4 to

33.4 ± 0.9 GPa, again peaked at $W_{0.97}Mo_{0.03}B_4$; after the peak, it again decreases linearly to 26.0 ± 0.8 GPa for the $W_{0.50}Mo_{0.50}B_4$ solid solution. The high-load hardness of the hardest solid solution in this series ($W_{0.97}Mo_{0.03}B_4$, H_V = 33.4 GPa) is at least 23% higher than that of the conventional cutting tool material, WC, with a Vickers hardness of 25.6 GPa measured under applied loads greater than 4.90 N.[3]

Since our EDS area mapping and XRD results (Figure 7.1 and Table 7.1) have eliminated the formation of any second phase(s) during the synthesis of the samples, the complete solubility of Mo in WB_4 argues strongly against the idea that dispersion/precipitation hardening is at the root of the sharp hardness peak present at ~3 at.% Mo in Fig. 7.2. Moreover, it appear unlikely that the hardening arises from size mismatch effects. This conclusion is based both on the close atomic radii of W (1.41 Å) and Mo (1.39 Å),[24] and on the fact that hardening due to atomic size mismatch generally appears as a broad deviate from Vegard's law near the end of solubility region.[23,25] The sharp peak in hardness seen at a low concentration of 3 at.% Mo in WB_4 does not follow any of the standard trends for a size mismatch based phenomenon. We must conclude, therefore, that this peak in the hardness is due to changes in the structure and bonding of WB_4 when doped with Mo.

In our previous study,[23] we attributed the sharp peaks observed in the Vickers hardness data for Ta and Mn doped WB_4 at low concentrations (~2 at.% Ta or 4 at.% Mn) to an electronic structure effect. Located in different columns of the Periodic Table, Ta (group 5) and Mn (group 7) each have a different number of valence electrons than W (group 6), imposing a change in the Fermi level of WB_4 when they substitute for W atoms. Either raising or lowering the valence electron counts, compared to W, should change the overall valence electron concentration (VEC)[21] as one varies the concentration of Ta or Mn in WB_4.[27] This, in turn, can change the mechanical properties, likely by influencing the strength of various metal-boron or metal-metal bonds in the

system.[22] Because the cohesive energy of a metallic solid is very sensitive to the details of the Fermi energy, the appearance of a sharp peaks in concentration-dependent hardness of WB_4-Ta and WB_4-Mn at low concentrations seems reasonable.[23] These low-concentrations may approach the optimal dopant levels that cause complete filling of σ bonding states between the *d* orbitals of the metals and the *p* orbitals of boron. Such doping would thus maximize the bond covalency.[21,22] Note that we could not verify the presence or absence of a low-concentration peak in the WB_4-Cr system in our previous study because of the overlap of such a peak with the observed hardness resulting from the limited solubility of Cr in WB_4 (<10 at.%). Because of the isoelectronic nature of W and Cr, it was assumed that no such peak existed, but the question can be resolved using our current electronically comparable system, WB_4-Mo, since W, Cr and Mo are all isoelectronic (group 6).

Here we find that upon adding small amounts of Mo to WB_4, the sharp peak is still observed in the Mo concentration dependent hardness (Fig. 7.2) at a low concentration of ~3 at.% Mo. To understand this result, we must first consider the unique crystal structure of WB_4. We have very recently shown, using neutron diffract experiments, that the structure of WB_4 consists of alternating hexagonal layers of boron and tungsten atoms, with some tungsten atoms (1/3) missing and their positions occupied by boron trimers.[18] Since both Mo and W have the same number of valence electrons (group 6), one would not expect to see this peak unless the atoms of Mo substitute for the boron trimers rather than for W atoms. The difference between the number of valence electrons for Mo and for boron trimers could change the total VEC and again result in stronger metal-boron bonds, leading to enhanced hardness. We note that the VEC is theoretically predicted to be optimized at around a 3% change, in good agreement with our results.[21] In support of this idea, we note that in contrast to the system examined here, $Os_{1-x}Ru_xB_2$ solid solutions,[22]

which also contain two elements from the same group of the Periodic Table (ruthenium (Ru) and osmium (Os), both group 8), show no enhance of hardening due to electronic structure changes. The structure of the $Os_{1-x}Ru_xB_2$ system is much simpler than WB_4, however, and has no sites that can be occupied by either metal or by boron. As a result, in that system, it therefore appears that the Fermi level remains constant, regardless of the dopant concentration. Hence, it appears that the unique structure of WB_4, with sites that can be occupied either by metal atoms or by boron trimers, allows for remarkable enhancements in hardness at very low hetero-atom doping levels.

After substituting for some of the boron trimers, as the concentration of Mo in WB_4 exceeds ~3 at.%, the molybdenum atoms likely begin substituting for tungsten atoms in the lattice, causing the linear hardness trends seen in Fig. 7.2. For this region (5-50 at.% Mo), it seems that the solid solutions mostly follow Vegard's law with a very low slope, as the atoms of W and Mo have similar radii and equal valence electron counts. Therefore, the size mismatch and the change in the energy profile of nearest neighbors are expected to be small, maintaining the symmetric motion of natural dislocations and making Vegard's law dominant in the hardness behavior of this system at medium to high dopant concentrations.

Based on these results, we suggest that the relatively broad peak that we observed in the Cr concentration dependent Vickers hardness curves for the WB_4-Cr system below ~10 at.% Cr in our past study[23] may well have been due to the overlap of two solid-solution hardening mechanisms: an electronic structure change due to the substitution of Cr for boron trimers, similar to the WB_4-Mo system, and hardening due to the atomic size mismatch between W (1.41 Å) and Cr (1.30 Å). Moreover, in previously studies systems with a difference in electron count (WB_4-Mn and WB_4-Ta), it may be that substitution of Mn and Ta for boron trimers also played a significant role.

It is interesting to speculate about the trends in hardness for Mo concentrations above 50 at.% Mo, as the structure moves gradually from WB_4 toward MoB_4 (known as $Mo_{0.8}B_3$, hexagonal *P6₃/mmc*).[24] Based on the data of Fig. 7.2, we interpret that the hardness should likely fall on a flat line sloping slightly downward, i.e. following Vegard's law. This is because the crystal structures and lattice constants of both end members (WB_4 and MoB_4) are very similar.[5,6,27] Mo atoms have less electron density than W atoms, however, and this should lead to reduced electronic repulsion in MoB_4 compared to WB_4, and thus lower hardness for MoB_4.[28] Similar behavior has been observed for other hard solid solutions.[28,29,30] By linearly extrapolating the hardness data shown here for the WB_4-Mo system (Fig. 7.2) beyond 50 at.% Mo, we estimate hardness values of ~23.9 and 35.9 GPa for MoB_4 under applied loads of 4.90 and 0.49 N, respectively. Note that our attempts to synthesize phase-pure MoB_4 by arc melting, even in the presence of excess boron, were not been successful due to the formation of the thermodynamically favorable phase molybdenum diboride (MoB_2).[31] Also, to our knowledge no reliable experimental or theoretical data are available in the literature for the hardness of MoB_4.

In an effort to further assess the suitability of these materials for applications such as cutting, the thermal stability of the hardest solid solution of WB_4 with Mo, i.e. $W_{0.97}Mo_{0.03}B_4$, is compared to that of WC in Fig. 7.3. Figure 7.3 shows that both materials are thermally stable in air up to ~400 ºC, which is similar to that of pure WB_4. The products of the thermal reactions include WO_3 and $B(OH)_3$ for $W_{0.97}Mo_{0.03}B_4$ and WO_3 for WC, as identified by powder X-ray diffraction. The higher weight gain for $W_{0.97}Mo_{0.03}B_4$ may be due to the formation of $B(OH)_3$ (boric acid) in $W_{0.97}Mo_{0.03}B_4$ while WC likely forms the gaseous product CO_2, which is lost during the thermal oxidation reaction. Thermal stability is important in cutting tool applications, where the local temperature can exceed several hundred degrees Celsius.

Conclusions

By successfully synthesizing WB_4 solid solutions with Mo and taking a systematic approach to the study of their Vickers hardness, we have demonstrated that the hardness of superhard transition metal borides can be enhanced by creating solid solutions with other transition metals, even metals that are isoelectronic with the parent. We found that the Vickers hardness, under applied loads of 4.90 and 0.49 N, respectively, increases from 28.1 and 43.3 GPa for pure WB_4 to 33.4 and 50.3 GPa for the solid solution containing 3 at.% Mo. This solid solution ($W_{0.97}Mo_{0.03}B_4$) is thermally stable up to ~400 ºC in air, and therefore has potential as a substitute for WC in tool applications. The results of this study suggest that not only can one metal substitute for another in the WB_4 crystal structure, but that metals can also substitute for boron trimers, thus changing the electronic structure of the lattice and resulting in a different type of solid solution hardening. This new possibility of substituting metals for boron may change our criteria for designing new superhard borides based on our understanding of their structures and possible hardening mechanisms.

Table 7.1. Lattice parameters and important *d*-spacings for WB_4 and its selected solid solutions with Mo, as measured using powder X-ray diffraction. Error values are given in parentheses.

Compound	**a(Å)**	**c(Å)**	**V(Å^3)**	d_{100}**(Å)**	d_{101}**(Å)**	d_{002}**(Å)**	d_{110}**(Å)**	d_{112}**(Å)**
WB_4	5.1985(4)	6.3371(7)	148.32	4.502072	3.670172	3.168565	2.599273	2.009608
$W_{0.97}Mo_{0.03}B_4$	5.1991(6)	6.3370(1)	148.34	4.502516	3.670384	3.168790	2.599529	2.009707
$W_{0.95}Mo_{0.05}B_4$	5.1997(2)	6.3379(3)	148.40	4.503055	3.670852	3.168945	2.599840	2.009966
$W_{0.90}Mo_{0.10}B_4$	5.2001(3)	6.3386(5)	148.44	4.503384	3.671168	3.169299	2.600030	2.010145
$W_{0.80}Mo_{0.20}B_4$	5.2003(1)	6.3391(3)	148.46	4.503558	3.671358	3.169544	2.600131	2.010254
$W_{0.70}Mo_{0.30}B_4$	5.2004(5)	6.3396(6)	148.48	4.503645	3.671522	3.169847	2.600181	2.010354
$W_{0.60}Mo_{0.40}B_4$	5.2011(3)	6.3398(1)	148.52	4.504242	3.671833	3.169813	2.600526	2.010505
$W_{0.50}Mo_{0.50}B_4$	5.2012(3)	6.3400(5)	148.53	4.504346	3.671967	3.170015	2.600585	2.010584

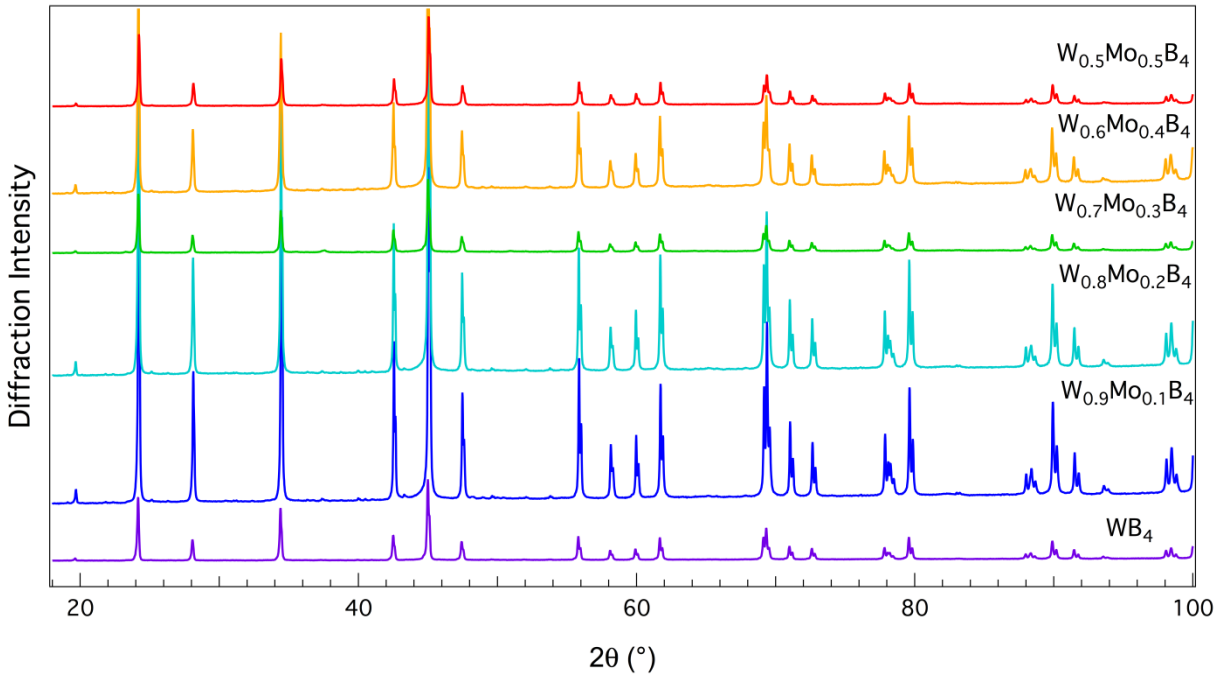

Figure 7.1. Selected X-ray diffraction patterns of tungsten tetraboride (WB_4) solid solutions with molybdenum (Mo). The bottom pattern corresponds to pure WB_4 (JCPDS, Ref. Code: 00-019-1373). These patterns show that Mo is completely soluble in WB_4 over the entire composition range studied from 0-50 at.%.

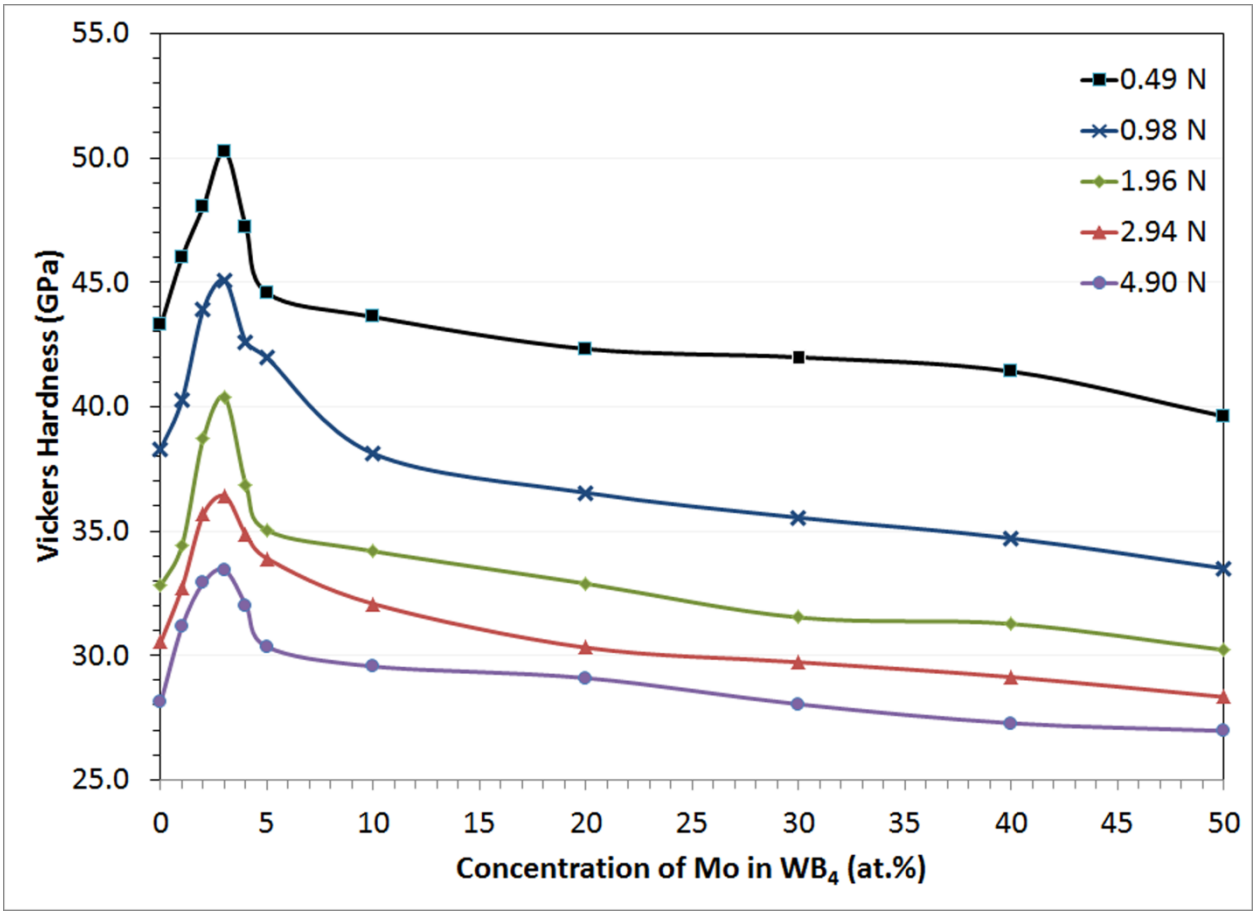

Figure 7.2. Vickers hardness of WB_4 solid solutions with Mo, ranging in concentration from 0-50 at.%, under applied loads of 0.49 (low load), 0.98, 1.96, 2.94 and 4.90 N (high load). The standard deviations of the mean hardness values under the applied loads of 0.49, 0.98, 1.96, 2.94 and 4.90 N are, respectively, within 3.51, 3.41, 2.72, 1.88 and 1.79 GPa.

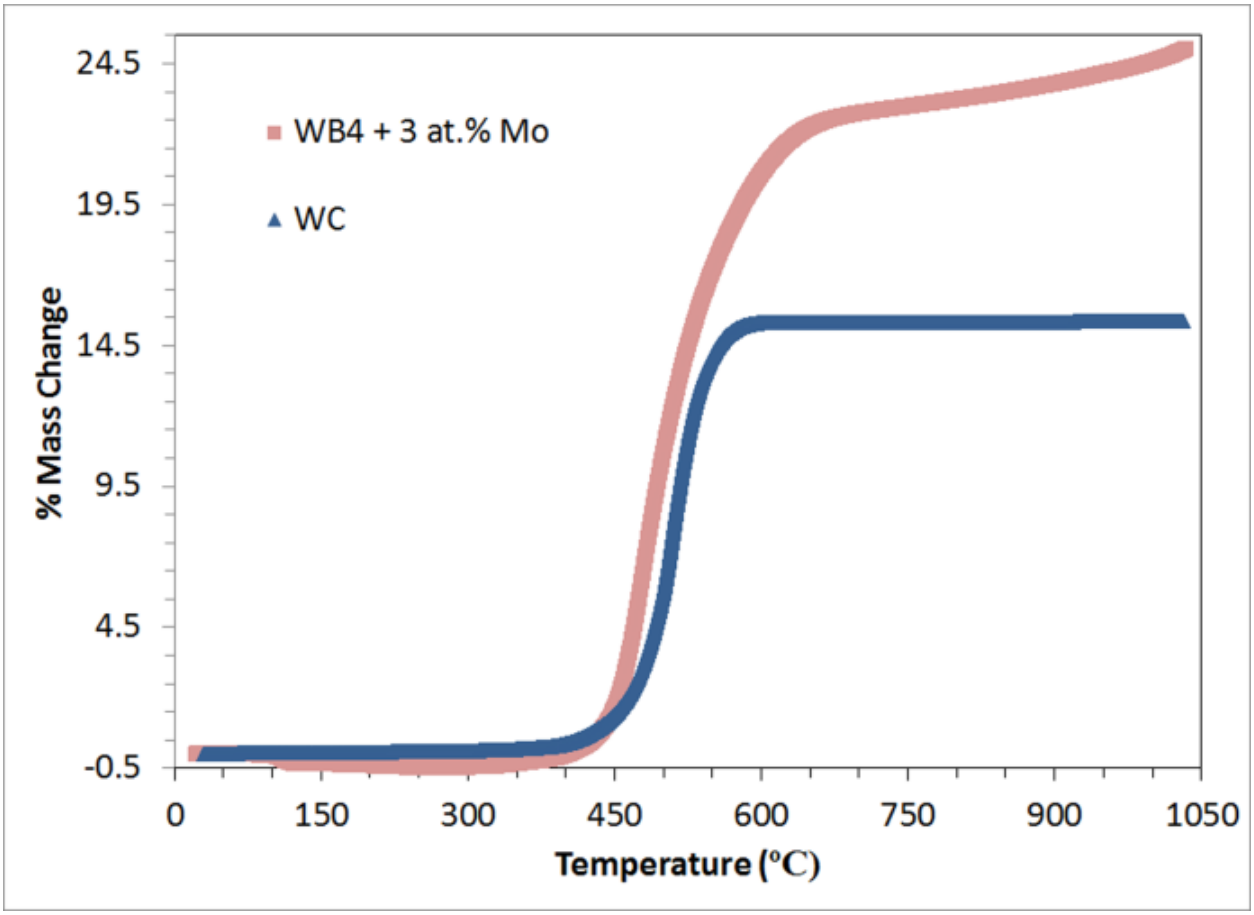

Figure 7.3. Thermal stability of the hardest solid solution of WB_4 with Mo, $W_{0.97}Mo_{0.03}B_4$, compared to the traditional cutting tool material, WC. It is observed that both materials are thermally stable in air up to ~400 ºC.

References

(1) Kaner, R. B.; Gilman, J. J.; Tolbert, S. H. Materials Science-Designing Superhard Materials. *Science* **2005**, *308*, 1268-1269.

(2) Levine, J. B.; Tolbert, S. H.; Kaner, R. B. Advancements in the Search for Superhard Ultra-Incompressible Metal Borides. *Adv. Funct. Mater.* **2009**, *19*, 3519-3533.

(3) Mohammadi, R.; Kaner, R. B. Superhard Materials. In *Encyclopedia of Inorganic and Bioinorganic Chemistry*; Scott, R. A., Ed.; John Wiley: Chichester, **2012**; DOI: 10.1002/9781119951438.eibc2076.

(4) Chung, H. Y.; Weinberger, M. B.; Yang, J. M.; Tolbert, S. H.; Kaner, R. B. Correlation between Hardness and Elastic Moduli of the Ultraincompressible Transition Metal Diborides RuB_2, OsB_2, and ReB_2. *Appl. Phys. Lett.* **2008**, 92, 261904 (3 pp).

(5) Chung, H. Y.; Weinberger, M. B.; Levine, J. B.; Kavner, A.; Yang, J. M.; Tolbert, S. H.; Kaner, R. B. Synthesis of Ultra-Incompressible Superhard Rhenium Diboride at Ambient Pressure. *Science* **2007**, *316*, 436-439.

(6) Levine, J. B.; Nguyen, S. L.; Rasool, H. I.; Wright, J. A.; Brown, S. E.; Kaner, R. B. Preparation and Properties of Metallic, Superhard Rhenium Diboride Crystals. *J. Am. Chem. Soc.* **2008**, *130*, 16953-16958.

(7) Levine, J. B.; Betts, J. B.; Garrett, J. D.; Guo, S. Q.; Eng, J. T.; Migliori, A.; Kaner, R. B. Full Elastic Tensor of a Crystal of the Superhard Compound ReB_2. *Acta Mater.* **2010**, *58*, 1530-1535.

(8) Tkachev, S. N.; Levine, J. B.; Kisliuk, A.; Sokolov, A. P.; Guo, S. Q.; Eng, J. T.; Kaner, R. B. Shear Modulus of Polycrystalline Rhenium Diboride Determined from Surface Brillouin Spectroscopy. *Adv. Mater.* **2009**, *21*, 4284-4286.

(9) Suzuki, Y.; Levine, J. B.; Migliori, A.; Garrett, J. D.; Kaner, R. B.; Fanelli, V. R.; Betts, J. B. Rhenium Diboride's Monocrystal Elastic Constants. *J. Acoust. Soc. Am.* **2010**, *127*, 2797-2801.

(10) Romans, P. A.; Krug, M. P. Composition and Crystallographic Data for the Highest Boride of Tungsten. *Acta Cryst.* **1966**, *20*, 313-315.

(11) Itoh, H.; Matsudaira, T.; Naka, S.; Hamamoto, H.; Obayashi, M. Formation Process of Tungsten Borides by Solid State Reaction between Tungsten and Amorphous Boron. *J. Mater. Sci.* **1987**, *22*, 2811-2815.

(12) Brazhkin, V. V.; Lyapin, A. G.; Hemley, R. J. Harder than Diamond: Dreams and Reality. *Philos. Mag.* **2002**, *82*, 231-253.

(13) Gu, Q.; Krauss, G.; Steurer, W. Transition Metal Borides: Superhard versus Ultra-Incompressible. *Adv. Mater.* **2008**, *20*, 3620-3626.

(14) Liu, C.; Peng, F.; Tan, . N.; Liu, J.; Li, F.; Qin, J.; Wang, J.; Wang, Q.; He, D. Low-Compressibility of Tungsten Tetraboride: a High Pressure X-ray Diffraction Study. *High Pressure Res.* **2011**, *31*, 275-282.

(15) Rau, J. V.; Latini, A.; Teghil, R.; De Bonis, A.; Fosca, M.; Caminiti, R.; Albertini, V. R. Superhard Tungsten Tetraboride Films Prepared by Pulsed Laser Deposition Method. *ACS Appl. Mater. Interfaces* **2011**, *3*, 3738-3743.

(16) Mohammadi, R.; Lech, A. T.; Xie, M.; Weaver, B. E.; Yeung, M. T.; Tolbert, S. H.; Kaner, R. B. Tungsten Tetraboride, an Inexpensive Superhard Material. *P. Natl. Acad. Sci. USA* **2011**, *108*, 10958-10962.

(17) Xie, M.; Mohammadi, R.; Zhu, M.; Armentrout, M. M.; Kavner, A.; Kaner, R. B.; Tolbert, S. H. Exploring the High-Pressure Behavior of Superhard Tungsten Tetraboride. *Phys. Rev. B* **2012**, *85*, 064118 (8 pp).

(18) Lech, A. T.; Turner, C. L.; Mohammadi, R.; Tolbert, S. H.; Kaner, R. B. Structure of Superhard Tungsten Tetraboride: A Missing Link between MB_2 and MB_{12} Higher Borides. *P. Natl. Acad. Sci. USA* **2051**, *112*, 3223-3228.

(19) Dieter, G. E. *Mechanical Metallurgy*; McGraw Hill: New York, 1986.

(20) Sha, J. B.; Yamabe-Mitarai, Y. Saturated Solid-Solution Hardening Behavior of Ir-Hf-Nb Refractory Superalloys for Ultra-High Temperature Applications. *Scripta Mater.* **2006**, *54*, 115-119.

(21) Jhi, S. H.; Ihm, J.; Louie, S. G.; Cohen, M. L. Electronic Mechanism of Hardness Enhancement in Transition-Metal Carbonitrides. *Nature* **1999**, *399*, 132-134.

(22) Weinberger, M. B.; Levine, J. B.; Chung, H. Y.; Cumberland, R. W.; Rasool, H.; Yang, J. M.; Kaner, R. B.; Tolbert, S. H. Incompressibility and Hardness of Solid Solution Transition Metal Diborides: $Os_{1-x}Ru_xB_2$. *Chem. Mater.* **2009**, *21*, 1915-1921.

(23) Mohammadi, R.; Xie, M.; Lech, A. T.; Turner, C. L.; Kavner, A.; Tolbert, S. H.; Kaner, R. B. Toward Inexpensive Superhard Materials: Tungsten Tetraboride-Based Solid Solutions. *J. Am. Chem. Soc.* **2012**, *134*, 20660-20668.

(24) Egami, T.; Waseda, Y. Atomic Size Effect on the Formability of Metallic Glasses. *J. Non-Cryst. Solids* **1984**, *64*, 113-134.

(25) Lundstrom, T.; Rosenberg, I. The Crystal Structure of the Molybdenum Boride $Mo_{1-x}B_3$. *J. Solid State Chem.* **1973**, *6*, 299-305.

(26) Zhou, Y. C.; Chen, J. X.; Wang, J. Y. Strengthening of Ti_3AlC_2 by Incorporation of Si to Form $Ti_3Al_{1-x}Si_xC_2$ Solid Solutions. *Acta Mater.* **2006**, *54*, 1317-1322.

(27) Gou, H.; Li, Z.; Wang, L. M.; Lian, J.; Wang, Y. Peculiar Structure and Tensile Strength of WB_4: Nonstoichiometric Origin. *API Adv.* **2012**, *2*, 012171 (9 pp).

(28) Wang, M.; Li, Y. W.; Cui, T.; Ma, Y. M.; Zou, G. T. Origin of Hardness in WB_4 and Its Implications for ReB_4, TaB_4, MoB_4, TcB_4, and OsB_4. *Appl. Phys. Lett.* **2008**, *93*, 101905 (3 pp).

(29) Hoffman, D. C.; Lee, D. M. Chemistry of the Heaviest Elements – One Atom at a Time. *J. Chem. Educ.* **1999**,*776*, 3317-347.

(30) Pershina, V.; Bastug, T.; Fricke, B. Relativistic Effects on the Electronic Structure and Volatility of Group-8 Tetraoxides MO4, Where M=Ru, Os, and Element 108, Hs. *J. Chem. Phys.* **2005**,*7122*, 12430171-1243079.

(31) Onoe, J. Relativistic Effects on Covalent Bonding: Role of Individual Valence Atomic Orbitals. *J. Phys. Soc. Jpn.* **1997**, *66*, 2328-2336.

(32) *ASM Handbook*, Volume 3: Alloy Phase Diagrams, 10^{th} Ed., ASM International, Materials Park, OH, USA, **1992**.

Chapter 8

Introduction

Metal borides represent an interesting class of covalently bound compounds with a wide range of mechanical, thermal and electronic properties.[1–4] These compounds have a broad variety of crystal lattices and different arrangements of boron atoms, ranging from isolated boron atoms ($Cr_2B_{(rhomb)}$) and networks of boron atoms ($TaB_{2(hex)}$) to skeletons of boron atoms ($UB_{12(cub)}$, $YB_{66(cub)}$).[1,2] Among the different borides, tungsten tetraboride (WB_4) represents a very interesting boride system due to its unique defect structure, which allows for hosting a wide variety of other transition metals in the lattice, forming alloys.[5–7] Addition of different transition metals has shown a dramatic increase in the mechanical properties of alloys of WB_4, which being already superhard (Vickers hardness $H_v \geq 40$ GPa), experience a further increase in hardness and toughness.[6,7]

Superhard materials are commonly used in the machining industry as cutting tools as only these superior materials can effectively work the stronger super-alloys used today. The primary focus of superhard materials development has solely relied on new compositions and chemical tuning of the crystal structure. While these intrinsic effects are fundamental to the development of such materials, there is a strong possibility that overall hardness can be dramatically enhanced using extrinsic effects following a completely orthogonal approach.

This chapter investigates the effects of group IV transition metals (titanium, zirconium and hafnium) on the hardness and thermal stability of the resulting alloys with tungsten tetraboride. Being in group IV, these metals possess two less valence electrons compared to tungsten (4 and 6 valence electrons respectively), therefore, greater electronic effects on the structure and properties

of corresponding alloys of WB_4 can be expected. In addition the atomic sizes of such metals is almost equal to that of tungsten in case of titanium (Ti = 140 Å, W = 135 Å)[8] and significantly bigger for zirconium and hafnium (Zr = 155 Å, Hf = 155 Å)[8], increasing the effects of atomic size mismatch on the mechanical properties. Moreover, titanium, zirconium and hafnium possess different higher boride phases, which is especially prominent in the case of latter two metals. Although zirconium and hafnium have the same atomic radii due to lanthanide contraction[8], their atomic radii are different in a twelve coordinate environment (with hafnium being slightly smaller than zirconium), which results in only zirconium having a dodecaboride phase (ZrB_{12}).[9,10] On the other hand, hafnium readily forms a β-rhombohedral boron doping phase (HfB_{50}), which being significantly harder that pure β-boron, can provide additional extrinsic routes of hardening the corresponding alloy of WB_4 due to tungsten tetraboride phase requiring excess boron in order to avoid the formation of the lower boride phases (WB_2).

Here we report the changes and differences in the structure, surface morphology and their respective effects on the hardness of the alloys of WB_4 with Ti, Zr, and Hf, as well as their thermal stability, and give possible explanations of the mechanisms of the properties' changes in each case.

Materials and Methods

In order to prepare the samples of the alloys of WB_4 with Ti, Zr and Hf metal powders of high-purity were used: tungsten (99.95%, Strem Chemicals, U.S.A.), amorphous boron (99+%, Strem Chemicals, U.S.A.), titanium (99%, Johnson Matthey Chemical Products, U.S.A.), zirconium (99.5%, Strem Chemicals, U.S.A.) and hafnium (99.8%, Materion, U.S.A.). The molar ratios of tungsten to boron was kept at 1:12 in order to prevent the formation of secondary boride phases of tungsten (WB_2).[11,7] The powders of appropriate metals were weighted according to the

calculated values for each sample of the alloys of WB_4 with Ti, Zr and Hf: $W_xTi_{1-x}B_4$, $W_xZr_{1-x}B_4$ and $W_xHf_{1-x}B_4$ (x=0.0-0.5). To ensure that the mixture were homogeneous, the samples were then thoroughly mixed in an agate mortar. The samples of mixtures of metal powders were then pressed into pellets using a hydraulic press (Carver) using an applied loading of 10 tons. The pressed samples were then loaded into the arc-melter chamber and arc-melted in argon atmosphere using a current of 70 amps for 3-5 minutes.

In order to carry out further analysis the arc-melted samples were cut into halves using a diamond saw (South Bay Technology Inc. U.S.A.). One half was to be used for powder XRD analysis, while the other was to be used for hardness measurements and EDS analysis. The first half of the cut sample was crushed using a steel pestle and mortar set into a fine sub 40 micron powder. The other half was placed into an epoxy encapsulation using epoxy/hardener set (Allied High Tech Products Inc., U.S.A.) for two days. After curing the epoxy in an oven for 1 hour at 50 ^oC, the samples were polished to an optically flat surface using a polishing station (South Bay Technology Inc., U.S.A.) and silicon carbide papers of 120-1200 grit sizes (Allied High Tech Products Inc., U.S.A.), followed by diamond films with particle size ranging from 30 to 1 micron (South Bay Technology Inc., U.S.A.).

The samples were then subjected to powder X-ray diffraction (PXRD) analysis and energy-dispersive X-ray spectroscopy (EDS) analysis in order to verify the composition and purity of the boride phases. The polished samples were checked for phase purity using an UltraDry EDS detector (Thermo Scientific, U.S.A.) attached to a FEI Nova 230 high resolution scanning electron microscope (FEI Company, U.S.A.). Powder XRD analysis was carried out on the crushed powder samples using Bruker D8 Discover Powder X-ray Diffractometer (Bruker Corporation, Germany). Powder XRD patterns were collected using a Cu Kα X-ray beam (λ=1.5418 Å) in the 5-100^o 2θ

range with a step size of 0.0355°, scan speed of 0.1055°/sec and time per step of 256.9 sec. The collected patterns were then cross-referenced against the patterns in the database of the Joint Committee on Powder Diffraction Standards (JCPDS) to identify the phases present in the XRD patterns.

Hardness measurements were performed on the polished samples using MicroMet 2103 Vickers microhardness tester (Buehler Ltd, U.S.A.) with a pyramidal diamond indenter tip. Each sample was indented 20 times in randomly chosen spots on the sample at each applied load (0.49, 0.98, 1.96, 2.94 and 4.9 N of force, low to high respectively). In order to calculate the Vickers hardness values (H_v, GPa) the diagonals of each indent was measured under a total magnification of 500x using a high resolution optical microscope, Zeiss Axiotech 100HD (Carl Zeiss Vision GmbH, Germany) and the following formula was used (Equation 8.1):

$$H_v = \frac{1854.4F}{d^2} \tag{8.1}$$

where F is the applied loading in Newtons (N) and d is the arithmetic average length of the diagonals of each indent in microns. The hardness values for all 20 indents for each respective loading were then averaged and plotted on the hardness graphs (Figure 8.2a-c). All calculated average hardness values under each applied load of 0.49, 0.98, 1.96, 2.94 and 4.9 N have a standard deviation within 4.31, 3.45, 2.92, 2.03 and 1.41 GPa respectively.

Thermogravimetric analysis was performed using a Pyris Diamond TGA/DTA unit (TG-DTA, Perkin-Elmer Instruments, U.S.A.). The samples were heated in an air atmosphere from 25 to 200 °C at a rate of 20 °C/min, held at 200 °C for half an hour to remove any moisture in the sample, heated from 200 to 1000 °C at a rate of 2 °C/min, held at 1000 °C for two hours and then

cooled from 1000 to 25 ^{o}C at a rate of 5 ^{o}C/min. In order to identify the resulting phases XRD analysis was performed.

In order to confirm the composition and purity of the samples energy-dispersive X-ray spectroscopy (EDS) was utilized. Additionally, powder X-ray diffraction (XRD) was used to verify the composition and phase purity of the samples. Figure 8.1a-c shows the powder XRD patterns respectively for the alloys $W_xTi_{1-x}B_4$, $W_xZr_{1-x}B_4$ and $W_xHf_{1-x}B_4$. Due to the stoichiometry used for the preparation of the samples, all of them contain excess crystalline boron, which cannot be observed under ordinary powder XRD.

Powder XRD patterns of the alloys of WB_4 and Ti ($W_xTi_{1-x}B_4$) are shown in Figure 8.2a. These patterns indicate that Ti is soluble in WB_4 at below 20 at.%; at greater concentrations a secondary phase, TiB_2 (JCPDS ref code: 01-075-0967), appears and its peaks corresponding to could be observed. It should be noted that peaks corresponding to WB_2 (JCPDS ref code: 01-073-1244) were not observed for $W_xTi_{1-x}B_4$ samples. Powder XRD patterns of the alloys of WB_4 and Zr ($W_{xZr1-x}B_4$) are showed in Figure 8.2b. These patterns indicate that Zr is soluble in WB_4 at below 10 at.%; at a concentration of Zr of 20 at.% a secondary phase, ZrB_{12} (JCPDS ref code: 03-065-7806), appears and its corresponding peaks can be observed. Peaks corresponding to WB_2 (JCPDS ref code: 01-073-1244) were observed at 40 at.% Zr for $W_xZr_{1-x}B_4$ samples. Powder XRD patterns of the alloys of WB_4 and Hf ($W_xHf_{1-x}B_4$) are showed in Figure 8.2c. These patterns indicate that Hf is soluble in WB_4 at below 8 at.%. At 10 at.% Hf, a secondary phase, HfB_{50} (β-rhombohedral boron doping phase, JCPDS ref code: 01-086-2400) and at 30 at.% Hf, HfB_2 (JCPDS ref code: 01-089-3651) could be observed. Peaks corresponding to WB_2 (JCPDS ref code: 01-073-1244) were observed at 30 at.% Hf for $W_xHf_{1-x}B_4$ samples. Formation of ZrB_{12} and HfB_{50} is thermodynamically favorable, due to them being the highest borides for Zr and Hf respectively.[1]

Confirming the composition and purity of the samples using powder XRD and EDS, Vickers microindentation hardness measurements were performed on each of the samples under applied loads of 0.49 to 4.9 N of force. The results of the hardness measurements are shown in Figure 8.2a-c.

For the $W_xTi_{1-x}B_4$ alloy, under the 0.49 N loading, the hardness increases to 50.9 ± 2.2 GPa, compared to 43.3 ± 2.1 GPa for pure WB_4 (corresponds to 0 at.% Ti on the graph) at the concentration of 8 at.% Ti.[6] With increasing concentration of Ti, the hardness decreases to 36.3 ± 1.71 GPa at 50 at.% Ti which could be attributed to the formation of TiB_2 secondary phase, having exceeded the solubility limit for Ti in WB_4. Similar observations can be made for the measurements done under other loads (0.98, 1.94, 2.94, and 4.9 N).

For the $W_xZr_{1-x}B_4$ alloy, under the 0.49 N loading, the hardness increases to 55.9 ± 2.7 GPa, at the concentration of 8 at.% Zr, followed by a decrease to 45.1 ± 2.6 GPa at 10 at.% Zr. With increasing concentration of Zr, the hardness increases slightly to 46.9 ± 2.3 GPa at 20 at.% Zr, followed by a decrease to 42.6 ± 2.2 GPa at 30 at.% Zr and then increases to 45.6 ± 2.3 GPa at 50 at.% Zr, which could be attributed to the formation of a metal dodecaboride, ZrB_{12} (hardness of ~40 GPa at 0.49 N of force)[12], secondary phase and its competition with WB_4 at higher concentrations of Zr.

For the $W_xHf_{1-x}B_4$ alloy, under the 0.49 N loading, a broad peak at 4-6 at.% Hf, with the hardness increase of 51.3 ± 2.9 GPa and 51.6 ± 2.8 GPa, respectively. This broad peak is followed by a decrease of hardness to 42.2 ± 2.7 GPa at 10 at.% Hf and a gradual increase to 45.4 ± 2.2 GPa at 50 at.% Hf, which can be attributed to exceeding the solubility limit of Hf in WB_4 and the formation of the β-rhombohedral boron doping phase, HfB_{50}, hardening the excess boron. HfB_{50}

has a hardness of ~40 GPa at 0.49 N compared to 34.2 GPa 0.49 N for a sample of crystalline β-rhombohedral boron.[13–15]

Results and Discussion

The structure of WB_4 has been investigated for many years.[7,11] Most recently Lech et al. demonstrated that the crystal structure of WB_4 not only contains partially filled tungsten sites (one-third of W atoms are systematically absent) but also boron trimer sites.[5] Therefore, this unique defective structure of WB_4 could be one of the causes of the hardening for the alloys of WB_4 with Ti, Zr and Hf (Figure 8.2a-c).[6] Being group IV elements, Ti, Zr and Hf have two less valence electrons than tungsten. Occupying position of the systematic absences of tungsten, these metal atoms can expand the number of boron vacancies.[6]

For the alloy of WB_4 with Ti ($W_xTi_{1-x}B_4$), this valence electron difference in combination with the similar, yet slightly greater size of Ti atom (1.40 Å, compared to 1.35 Å for W)[8] can explain the hardness increase at 8 at.% Ti. Titanium atoms occupy the positions devoid of tungsten atoms and the increase in hardness is due to solid-solution hardening. TiB_2 is the highest boride of Ti, however, it can also form β-rhombohedral boron doping phase (TiB_{50})[16].

Due to the relatively smaller X-ray cross section of titanium (compared to tungsten), this phase does not appear in XRD, however, it can be seen using EDS (Figure 8.3). This can explain the smooth decrease of hardness at concentrations of Ti greater than 10 at.%. As the concentration of Ti increases, it starts to form TiB_2 secondary phase, which is while being the hardest AlB_2-type diboride (hardness of 35 GPa at 0.49 N of force)[17], is still softer than pure WB_4. In addition, it can be noted that TiB_2 phase is located in the tungsten reach areas (WB_4) and given the high melting temperature of this phase (3225 ^oC, compared to 2020 ^oC for WB_4)[16,18], we can draw a conclusion

that TiB_2 precipitates out first from the melt and provides a template pattern for the further precipitation of WB_4 phase. This combined with the formation of a β-rhombohedral boron doping phase, TiB_{50} (hardness of 36.4 GPa at a load of 0.49 N)[14] provide no extrinsic hardening for the $W_xTi_{1-x}B_4$ alloy decreases the overall hardness.

For the alloy of WB_4 with Zr ($W_xZr_{1-x}B_4$), valence electron difference, metal size mismatch (Zr = 1.55 Å, W = 1.35 Å)[8] in combination with the drastic change of surface morphology (Figure 8.4) can provide a partial explanation of the sharp hardness peak at 8 at.% Zr. Similarly to titanium, zirconium atoms can occupy the positions devoid of tungsten atoms and the increase in hardness is due to solid-solution hardening. In contrast to titanium, zirconium's highest boride phase is a metal dodecaboride ZrB_{12}.[16] Moreover, while Zr also possesses a β-rhombohedral boron doping phase (ZrB_{50}) it does not readily form it due to the availability of a higher boride, ZrB_{12} (Figure 8.5).

Comparing the phase diagrams for the W-boron and Zr-boron systems, it can be noted that there is a similarity to the way both WB_4 and ZrB_{12} form.[18,19] It was previously reported that the formation of metal dodecaborides (MB_{12}) is very much dependent on the size of the metal atom in order to accommodate a cuboctahedron unit of boron atoms with zirconium (1.55 Å) and yttrium (1.80 Å), being the smallest and largest metal atoms, respectively, capable of forming dodecaboride structures.[9,10] While, tungsten atom is too small to accommodate a cuboctahedron boron unit and form a dodecaboride, it can be proposed that that $W_xZr_{1-x}B_4$ alloy can form a meta-stable dodecaboride that decomposes to the hexagonal WB_4 structure at low concentrations of Zr, with the 8 at.% Zr being the optimal amount as seen by the drastic change of surface morphology (Figure 8.4).[7,10] Similar changes in surface morphology and as a result in hardness can be expected for other transition metals capable of forming dodecaboride species: scandium and yttrium.

Hardness changes at concentrations of zirconium greater than 10 at.% may be attributed to the following reasons: at below 20 at.% zirconium, ZrB_{12} secondary phase appears, which hardens the material through dispersion-hardening mechanism. At greater concentrations of zirconium, ZrB_{12} and WB_4 phases, being the highest borides of zirconium and tungsten respectively, compete with one another. The hardness of $W_xZr_{1-x}B_4$ gently increases as it approaches 50 at.% Zr and more ZrB_{12} is formed.

For the alloy of WB_4 with Hf ($W_xHf_{1-x}B_4$), valence electron difference, metal size mismatch (Hf = 1.55 Å, W = 1.35 Å)[8] may provide an explanation of the broad hardness peak at 4-6 at.% Hf. Similarly to titanium and zirconium, hafnium atoms can occupy the positions missing tungsten atoms and the increase in hardness is due to solid-solution hardening. Similarly to titanium, hafnium's highest boride phase is a diboride HfB_2, however, it also forms the β-rhombohedral boron doping phase, HfB_{50}.[13] In contrast to TiB_{50}, hafnium has a large enough X-ray cross section for the HfB_{50} phase to appear in powder XRD spectrum (Figure 8.1c). Although due to lanthanide contraction, for most purposes zirconium and hafnium have essentially the same atomic radius (1.55 Å)[8], in contrast to zirconium, hafnium does not form a dodecaboride phase under ambient pressure, however, it can be synthesized with application of 6.5 GPa of pressure.[9] This is due to the fact that in a twelve coordinate environment zirconium and hafnium have different metallic radii: 1.603 and 1.580 Å, respectively.[9]

HfB_{50} phase appears as secondary phase at 10 at.% Hf (Figure 8.1c). Figure 8.6 shows the elemental maps of a sample of an alloy of WB_4 with 10 at.% Hf ($W_{0.90}Hf_{0.10}B_4$). It can be noted that hafnium is present not only in tungsten rich areas (showing the presence of Hf in WB_4 lattice) but also in boron rich areas (forming HfB_{50}). As the concentration of hafnium increases it extrinsically hardens WB_4 by hardening the excess crystalline boron (Figure 8.2c).

Table 8.1 compares the values of hardness for the hardest compositions of alloys of WB_4 with Ti, Zr and Hf with those of pure WB_4 and the hardest WB_4 alloy reported, $W_{0.93}Ta_{0.02}Cr_{0.05}B_4$.[6] Both $W_{0.93}Ta_{0.02}Cr_{0.05}B_4$ and $W_{0.92}Zr_{0.08}B_4$ have similar total secondary metal content, 7-8 at.%, and while $W_{0.92}Zr_{0.08}B_4$ is slightly softer than $W_{0.93}Ta_{0.02}Cr_{0.05}B_4$ at low load (0.49 N), it exhibits increased hardness values at higher loads, indicating a smaller influence of the indentation size effect due to the extremely fine surface morphology of the that sample (Figure 8.5).

Oxidation resistance is an important parameter for materials used for cutting and machining tools. As such, in order to test the thermal stability of the samples of alloys of Ti, Zr and Hf with WB_4 thermogravimetric analysis was performed on the samples with the compositions corresponding to the hardest alloys. Figure 8.7 summarized the results.

The TGA data shows that alloys of Ti, Zr and Hf with WB_4 have enhanced oxidation properties in comparison to the pure WB_4 and the hardest tantalum-chromium alloys of WB_4 ($W_{0.93}Ta_{0.02}Cr_{0.05}B_4$). $W_{0.92}Ti_{0.08}B_4$, $W_{0.92}Zr_{0.08}B_4$ and $W_{0.94}Hf_{0.06}B_4$ are stable up to ~460 ^oC, ~510 ^oC and ~490 ^oC respectively, compared to ~400 ^oC for pure WB_4 and ~420 ^oC for $W_{0.93}Ta_{0.02}Cr_{0.05}B_4$ alloy. The products of oxidation reaction were WO_3 and TiO_2 for $W_{0.92}Ti_{0.08}B_4$, WO_3 and ZrO_2 for $W_{0.92}Zr_{0.08}B_4$, and WO_3 and HfO_2 for $W_{0.94}Zr_{0.06}B_4$ samples, as determined by PXRD analysis. Thus shows an increase of almost 100 ^oC in oxidation temperature for the zirconium alloy of WB_4 with a comparable hardness to that of $W_{0.93}Ta_{0.02}Cr_{0.05}B_4$.

Conclusions

Alloys of WB_4 with group IV transition metals, Ti, Zr and Hf, were synthesized and their hardness and thermal stability was characterized. These metals are interesting due to the higher boride phases they can form: metal dodecaboride and β-rhombohedral boron doping phases. $W_{0.92}Ti_{0.08}B_4$, $W_{0.92}Zr_{0.08}B_4$, $W_{0.94}Hf_{0.06}B_4$ showed the highest values of hardness (at 0.49 N applied load) for their respective alloys at 50.9, 55.9 and 51.6 GPa respectively, compared to 43.3 GPa for pure WB_4. In addition, the alloys of WB_4 with zirconium and hafnium showed extrinsic hardness capabilities at higher concentrations of zirconium and hafnium. Alloys of WB_4 with zirconium showed drastic changes in the surface morphology of the corresponding samples at below 10 at.% Zr range, which was likely due to the formation of a meta-stable Zr-W dodecaboride phase. This was due to the formation of the hard metal dodecaboride phase (ZrB_{12}) for zirconium and hardening of the excess boron, through the formation of β-rhombohedral boron doping phase (HfB_{50}) for hafnium. In addition, the alloys of titanium, zirconium and hafnium with WB_4 showed increased oxidation resistance up to ~460 ^oC, ~510 ^oC and ~490 ^oC respectively, compared to ~400 ^oC for pure WB_4. By exploring the possibility of adding other metals with bigger atomic radii compared to tungsten and different higher boride phases, such as YB_{66}[20] for yttrium and ScB_{19}[21] for scandium, to WB_4, their effects on such alloys can be studies and other possible mechanism and routes of hardening investigated.

Table 8.1. Vickers microindentation hardness data for the hardest alloys of WB_4 with Ti, Zr and Hf, under applied loads ranging from 0.49-4.9 N of force. Hardness data for pure WB_4 and $W_{0.93}Ta_{0.02}Cr_{0.05}B_4$ alloy is given for comparison.[6]

Compound/alloy	Applied Load (N)				
	0.49	**0.98**	**1.96**	**2.94**	**4.9**
WB_4	43.4	38.3	32.8	30.5	28.1
$W_{0.93}Ta_{0.02}Cr_{0.05}B_4$	57.3	44.1	38.2	34.8	31.7
$W_{0.92}Ti_{0.08}B_4$	50.9	39.9	36.2	34.5	32.5
$W_{0.92}Zr_{0.08}B_4$	55.9	42.9	39.8	35.9	34.7
$W_{0.94}Hf_{0.06}B_4$	51.6	40.2	35.1	33.7	32.3

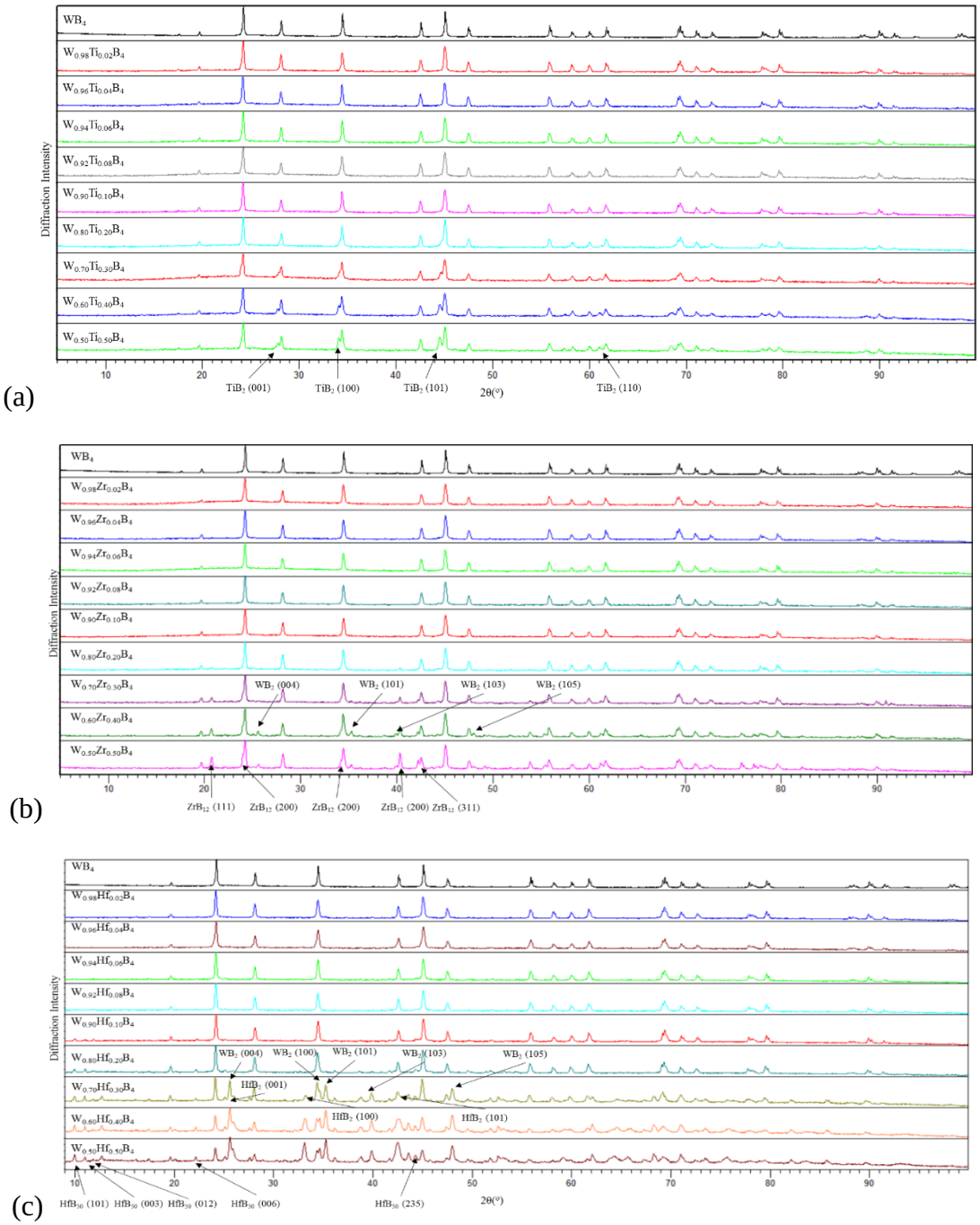

Figure 8.1. Powder XRD patterns of alloys of WB_4 with 2-50 at.% Ti (a), Zr (b) and Hf (c) added on a metals basis. The top spectra in each set is pure WB_4 (JCPDS ref code: 00-019-1373). The solubility limit is less than 20 at.% for Ti, 10 at.% for Zr and below 8 at.% for Hf. Above 20 at.% Ti, TiB_2 (JCPDS ref code: 01-075-0967), above 20 at.% Zr, ZrB_{12} (JCPDS ref code: 03-065-7806) and above 10 and 20 at.% Hf, HfB_{50} (β-rhombohedral boron doping phase) and HfB_2 (JCPDS ref codes: 01-086-2400 and 01-089-3651) appear respectively as secondary phases. In addition, peaks corresponding to WB_2 (JCPDS ref code: 01-073-1244) could be observed at 40 at.% Zr and 30 at.% Hf.

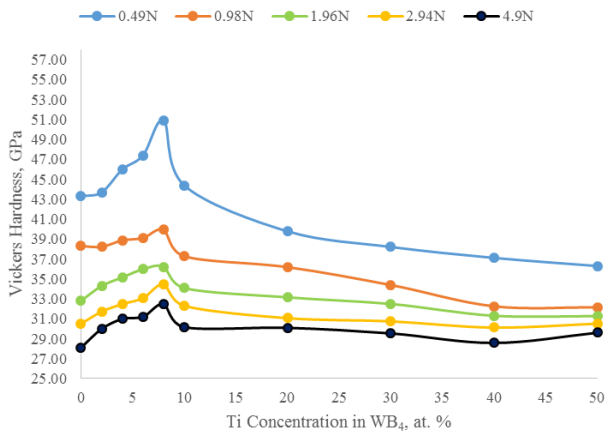

(a)

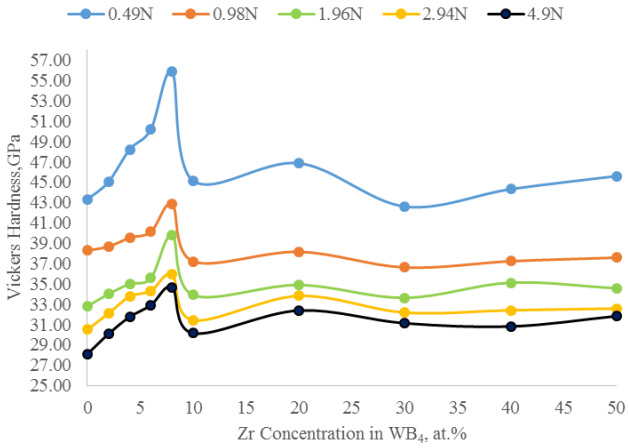

(b)

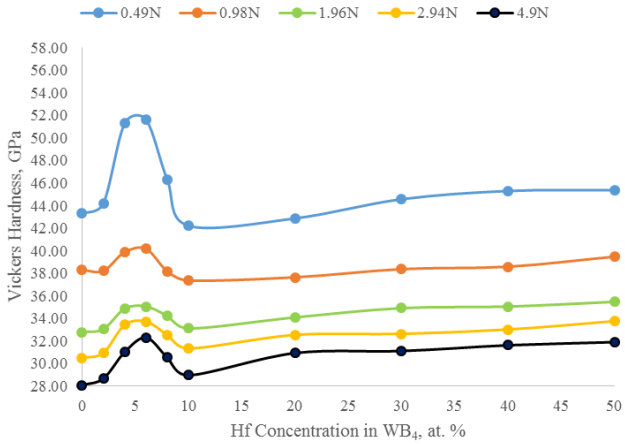

(c)

Figure 8.2. Vickers microindentation hardness of tungsten tetraboride alloys with Ti (a), Zr (b), and Hf (c) under 0.49 N (low) to 4.9 N (high) loads. The concentrations were changed in WB_4 by adding 2-50 at.% Ti, Zr, and Hf on a metals basis.

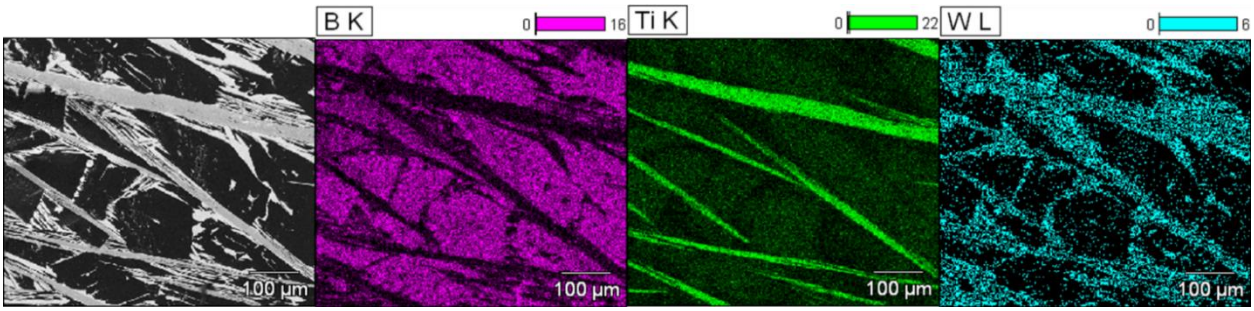

Figure 8.3. Elemental maps for boron (K line), titanium (K line) and tungsten (L line) for the $W_{0.50}Ti_{0.50}B_4$ alloy showing presence of titanium in TiB_{50} (β-rhombohedral boron doping phase) corresponding to boron rich areas and TiB_2 in tungsten rich areas.

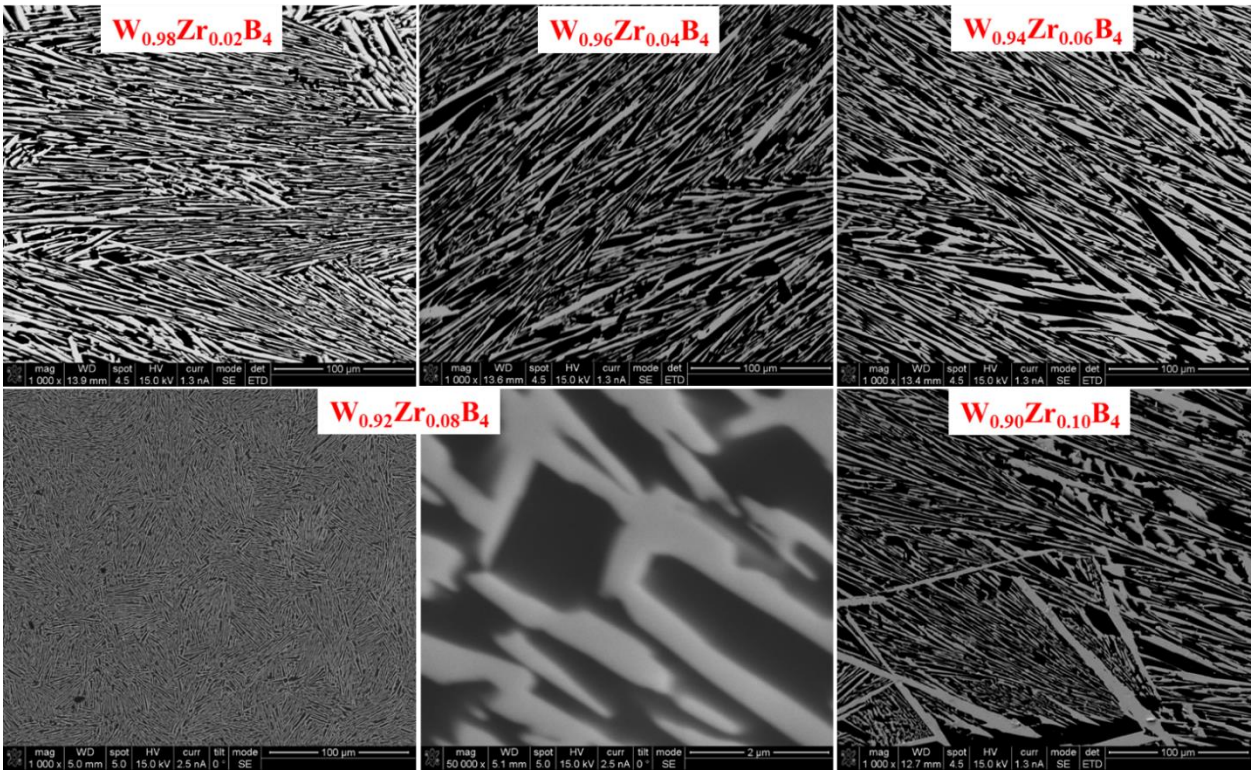

Figure 8.4. SEM images of the alloys of WB_4 with 2-10 at.% Zr taken at 1000x magnification and 50000x for the hardest solution, $W_{0.92}Zr_{0.08}B_4$, showing changes in morphology. The drastic change of surface morphology at 8 at.% Zr can be attributed to a decomposition from a meta-stable W-Zr dodecaboride phase.

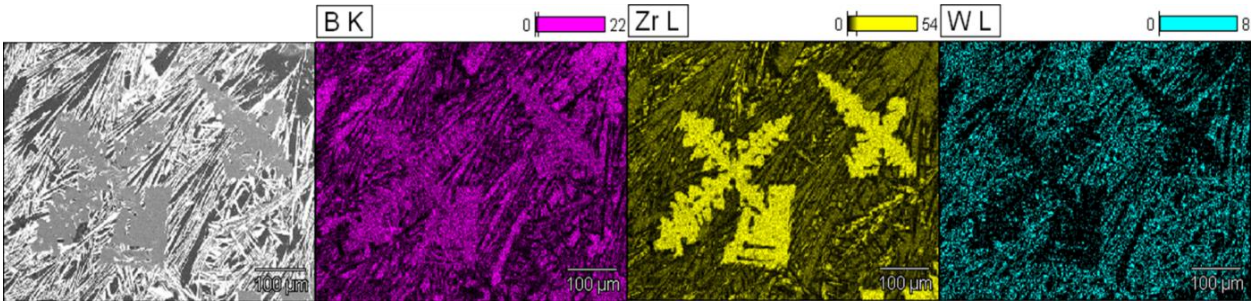

Figure 8.5. Elemental maps for boron (K line), zirconium (L line) and tungsten (L line) for the $W_{0.50}Zr_{0.50}B_4$ alloy showing presence of zirconium in ZrB_{12} and no formation of ZrB_{50} (β-rhombohedral boron doping phase).

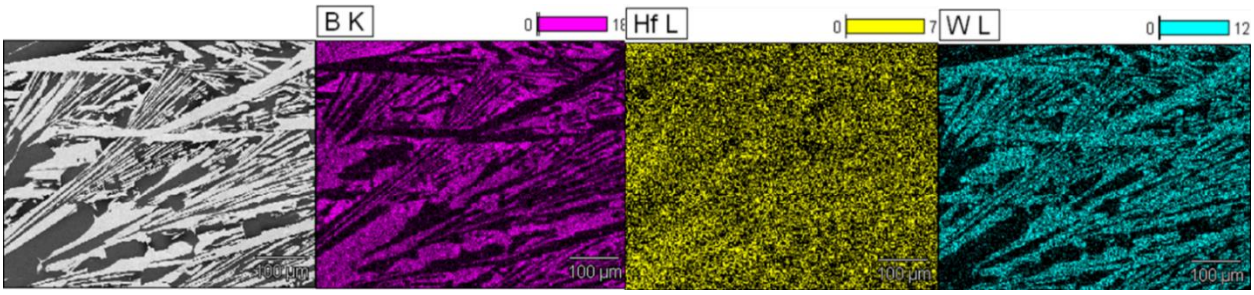

Figure 8.6. Elemental maps for boron (K line), hafnium (L line) and tungsten (L line) for the $W_{0.90}Hf_{0.10}B_4$ alloy showing presence of hafnium in WB_4 as well as in boron-rich phase (as β-rhombohedral boron doping phase – HfB_{50}).

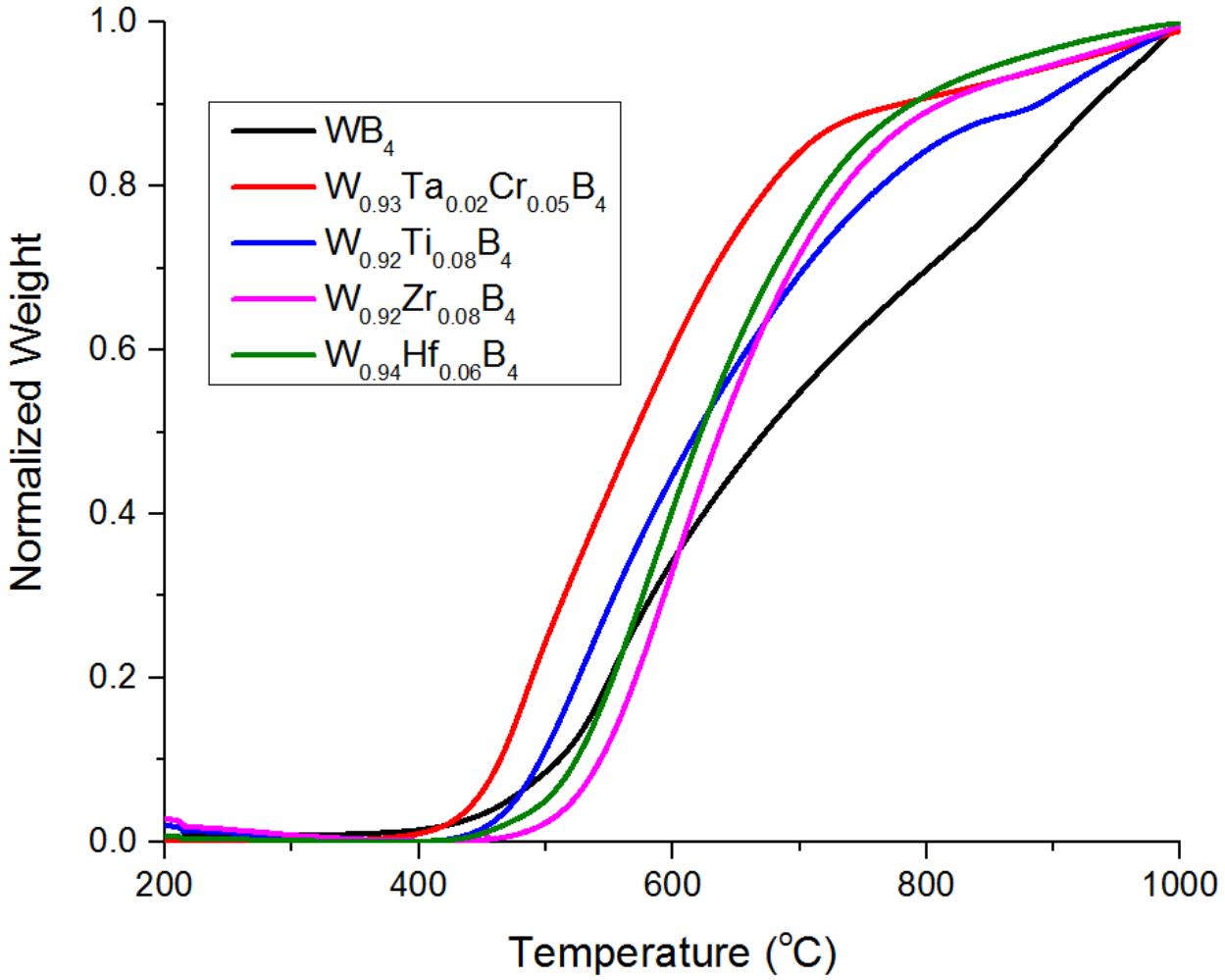

Figure 8.7. Thermal stability of the hardest tungsten tetraboride alloys with Ti, Zr and Hf as measured by thermal gravimetric analysis. The data for pure WB_4 and the hardest alloy $W_{0.93}Ta_{0.02}Cr_{0.05}B_4$ are given for comparison. These data show that $W_{0.92}Ti_{0.08}B_4$, $W_{0.92}Zr_{0.08}B_4$ and $W_{0.94}Hf_{0.06}B_4$ are stable up to ~460 °C, ~510 °C and ~490 °C respectively (using extrapolated oxidation onset), compared to ~400 °C for pure WB_4 and ~420 °C for $W_{0.93}Ta_{0.02}Cr_{0.05}B_4$ alloy.

References

(1) Samsonov, G.V. *Borides*; Atomizdat: Moscow, 1975.

(2) Samsonov, G.V.; Markovskii, L. Y. *Boron, Its Compounds and Alloys*; House of the Academy of the Sciences Ukrainian SSR: Kiev, 1960.

(3) Mohammadi, R.; Kaner, R. B. *Encycl. Inorg. Bioinorg. Chem.* **2012**.

(4) Kaner, R. B.; Gilman, J. J.; Tolbert, S. H. *Science.* **2005**, *308* (5726), 1268–1269.

(5) Lech, A. T.; Turner, C. L.; Mohammadi, R.; Tolbert, S. H.; Kaner, R. B. *Proc. Natl. Acad. Sci.* **2015**, *112* (11), 3223–3228.

(6) Mohammadi, R.; Xie, M.; Lech, A. T.; Turner, C. L.; Kavner, A.; Tolbert, S. H.; Kaner, R. B. *J. Am. Chem. Soc.* **2012**, *134* (51), 20660–20668.

(7) Mohammadi, R.; Lech, A. T.; Xie, M.; Weaver, B. E.; Yeung, M. T.; Tolbert, S. H.; Kaner, R. B. *Proc. Natl. Acad. Sci. U. S. A.* **2011**, *108* (27), 10958–10962.

(8) Slater, J. C. *J. Chem. Phys.* **1964**, *41* (10), 3199–3204.

(9) Cannon, J. F.; Farnsworth, P. B. *J. Less Common Met.* **1983**, *92* (2), 359–368.

(10) La Placa, S.; Binder, I.; Post, B. *J. Inorg. Nucl. Chem.* **1961**, *18* (0), 113–117.

(11) Romans, P. a.; Krug, M. P. *Acta Crystallogr.* **1966**, *20* (2), 313–315.

(12) Kuzenkova, M.A.; Kislyi, P. S. *Powder Metall.* **1965**, *12* (36), 966–969.

(13) Portnoi K.I., Romashov V.M., Romanovich I.V., L. Y. V. *Inorg. Mater.* **1971**, *7*, 1769–1772.

(14) Carlsson, J.-O.; Lundström, T. *J. Less Common Met.* **1970**, *22* (3), 317–320.

(15) Andersson, S.; Lundström, T. *J. Solid State Chem.* **1970**, *2* (4), 603–611.

(16) Murray J.L., Liao P.K., and S. K. E. *Bin. Alloy Phase Diagrams* **1990**, *1*, 544–548.

(17) Basu, B.; Raju, G. B.; Suri, A. K. *Int. Mater. Rev.* **2006**, *51* (6), 352–374.

(18) Duschanek, H.; Rogl, P. *J. Phase Equilib.* **1995**, *16*, 150–161.

(19) Portnoi, K. I. *Sov. Powder Met. Met. Ceram.* **1970**, *9*, 577–580.

(20) Richards, S. M.; Kaspar, J. S. *Acta Crystallogr. Sect. B Struct. Crystallogr. Cryst. Chem.* **1969**, *25* (2), 237–251.

(21) Tanaka, T.; Okada, S.; Gurin, V. . *J. Alloys Compd.* **1998**, *267* (1-2), 211–214.

Chapter 9

The contents of this chapter will be concise, but ultimately lead to a conclusion.

Historically, the superhard material project(s) in the Kaner lab has always been both a continuation of the former students' project(s), and a branching out on one's own. Along the way, and through the pedigree of "superhard" students (many now Ph.D.'s) before me have produced a significant contribution to the hard material world, namely in borides. While tungsten tetraboride had just been successfully created prior to me joining the lab, I have seen it through, with my colleagues, peers, and mentors, many iterations of successful and less-than-successful formulations. Papers are not published on failed experiments; everything you read in a paper was realized through experience. Success is drawn from *why* the previous experiment failed, dumb luck, or an educated understanding of what *should* happen. Dumb luck is always de-convoluted into some explanation with *when* (how long until it is understood) being the predominant variable. My initial and continuous work, as evidenced in publications, was with tungsten tetraboride and its solid solutions. Hand-in-hand with Drs. Mohammadi and Lech, we charted the many variables that are: definitive crystal structure, transition metal solubility, boron deficiency limits, and forcing the structure type with variable compositions. Countless hours and iterations have been devoted solely to flesh out a "matrix of matter" unique to the tetraboride crystal structure. Hundreds, if not thousands of samples have been mixed, synthesized, and characterized to fill out this matrix; the purpose has been two-fold—understand the material, WB_4,

specifically (hardness, toughness, solubility limits, etc.) but more importantly, the rational as to *why* the structure behaves as such, "how it ticks". For instance, intrinsic and extrinsic hardening effects play important roles in WB_4, but at a cost such as oxidation resistance or toughness. The metal boride family has particularly unique structures, the metal atoms become more segregated as the boron content increases, which then "pin" the movement of atoms. The explanation seems trivial, but the papers (a select few in the prior chapters) in the past decade are proof that the understanding of this phenomena is an after-the-fact conclusion requiring many experiments to test the hypothesis. Our more recent works have explored the behavior, expanding our arsenal of borides with "tailored properties".

The functionalization, or application, of tungsten tetraboride (and its solid solutions) has been the primary focus of my Ph.D. program, while the more fundamental and academic endeavors served to enrich the understanding of borides. Ultimately, there has been success in producing both abrasives and composites utilizing the materials developed within our lab. Tungsten carbide has undergone nearly a century of intensive research, and many of the leading compositions used today are at least a decade old. The most recent trend in the industrially used ceramic metallic (read *cermet*, namely composites such as WC-Cobalt) field is "nano"-: composites, grains, agglomerates, and particles. Furthermore, this recent interest in nano- stems from the unique behavior other materials exhibit in the size regime—namely semi-conductors and carbon allotropes. Tungsten carbide is sensitive to grain growth at elevated temperatures, thereby necessitating strict sintering recipes. Nano-carbides are even more susceptible; grain growth inhibitors, namely TiC and TaC, are used to some effect. Fortunately, the borides do not seem to suffer undesirable grain growth (from preliminary experimental results), but in the presence of an excess transition metal other secondary (or

tertiary) boride phases may form at grain boundaries. This behavior is predictable and may prove to be useful particular applications in the future.

It may be of some assuagement to Dr. Lech that WB_4 composites are in fact producible; it was an arduous task to figure out the necessary synthetic parameters, but determination and countless experiments have prevailed. The future of these composites is bright and optimistic, despite the tremendous amount of work needed to "complete" the matrix of binders/compositions. Various synthetic methods are employable to produce a uniformly dense composite of different binder (and binder composition) ratios, making this material a truly comprehensive successor to the tungsten carbide and (potentially) poly-crystalline diamond applications used worldwide.